Potentiel de la robotique pour l'inspection thermographique par chauffage inductif

Mémoire

Mohammed-Yacine Mokhtari

Maîtrise en génie électrique - avec mémoire
Maître ès sciences (M. Sc.)

Québec, Canada

Potentiel de la robotique pour l'inspection thermographique par chauffage inductif.

Mémoire

Mohammed Yacine MOKHTARI

Sous la direction de :

Xavier MALDAGUE, directeur de recherche

Résumé

La thermographie par courants de Foucault (ECT) est une méthode de thermographie active. L'excitation inductive génère des courants de Foucault dans les spécimens conducteurs. En présence de défauts, la circulation des courants est affectée par ces discontinuités produisant un changement dans la distribution de la température autour des défauts. Ces changements sont observés avec une caméra infrarouge. Dans ce travail, on présente une application robotique de la thermographie par courants de Foucault. Une interface robotique a été développée et tous les capteurs utilisés ont été intégrés à la plateforme. Des simulations ont été achevées avec COMSOL Multiphysics en variant différents paramètres. Des expériences ont été menées sur plusieurs spécimens (de différents matériaux) avec des défauts de différents types et tailles. La linescan thermographie est principalement étudiée et d'autres modes d'inspections ont été explorés. Les images résultantes sont reconstruites avec un algorithme dédié. Finalement, les résultats de la méthode sont comparés à ceux de la thermographie optique (par halogène) pour montrer les capacités de la méthode.

Abstract

Eddy current thermography (ECT) is an active thermography method. The inductive excitation generates Eddy currents in electrically-conductive specimen. In a presence of defects, the eddy current flow is affected by these discontinuities leading to changes in the temperature distribution in the specimen around the defects. These changes are observed by an infrared camera. In this work, we present a robotic application of the method. A robotic interface is developed and all the sensors needed are integrated to the platform. Simulations are performed using COMSOL Multiphysics by varying different parameters. Experiments are realised on different specimens (made of different materials) with defects of different sizes. The linescan Eddy current thermography is studied and other modes are explored. The resulting images are reconstructed with a dedicated algorithm. Finally, the method's results are compared to optical thermography to show the capability of the method.

Table des matières

Liste des tableaux

Liste des figures

Remerciements

Tout d'abord, je tiens à remercier chaleureusement mon directeur de maîtrise, le professeur Xavier MALDAGUE, pour son soutient, son aide, et ses précieux conseils tout au long de ce travail. Ça a été un honneur d'être votre étudiant et de faire partie de votre équipe de recherche.

Je remercie également l'Université LAVAL et le laboratoire de recherche MIVIM qui a permis l'aboutissement de ce travail en fournissant les moyens et l'atmosphère propice au développement de la recherche.

Mes remerciements à Clemente Ibarra-Castanedo pour son aide précieuse ainsi que ses conseils avisés pour la réalisation de ce travail. Je tiens aussi à remercier l'équipe de VISIOO Image, Matthieu KLEIN et Adel ZIADI, d'avoir fourni équipements et conseils pour ce travail.
Enfin, Je tiens à remercier mes parents qui ont toujours été présent pour moi et m'ont toujours soutenu de manière inconditionnelles. Je vous aime.

Avant-propos

Dans la démarche de ce travail, plusieurs articles concernant la thermographie robotisée ont été publiés. On présente ici ces publications.

thermographie Robotique par courants de Foucault : simulations et expérimentations

Il s'agit d'un article publié dans la conférence Quantitative Infrared Thermography (QIRT) 2016 sous le titre original (en Anglais) : Robotic Eddy Current Thermography : Simulations and experiments en tant qu'auteur principal. On détaille ici les contributions de chacun des co-auteurs :

Contributions des auteurs :

Yacine MOKHTARI :

auteur principal, a réalisé les simulations COMSOL en variant les paramètres étudiés, a réalisé les différentes expérimentations à l'aide du robot ainsi que la programmation de ce dernier, a effectué le traitement des résultats et leurs analyse, et rédigé l'article.

C Ibarra-Castanedo :

a aidé pour l'établissement de L'expérimentation et sa réalisation, a aidé pour le traitement des résultats et leur analyse, ainsi que la correction du manuscrit.

Pierre Servais :

a aidé avec son expertise et la revue de l'article.

Xavier MALDAGUE :

directeur de la maitrise, supervision, révision, et correction de l'article.

Thermographie linesan robotisée, une nouvelle façon de produire une carte CND de structure aérospatiale complexe

Cet article a été publié dans la conférence Canadian Institute of Nondestructive Evaluation (CINDE), 2017 en tant qu'auteur principal. On présente ici les contributions de chacun des co-auteurs :

Contributions des auteurs :

Yacine MOKHTARI :

auteur principal, a réalisé les différentes expérimentations à l'aide du robot ainsi que la programmation de ce dernier, a effectué le traitement des résultats et leurs analyse, a effectué la comparaison des résultats des deux méthodes étudiées et analysé les résultats obtenus, et a rédigé l'article.

C Ibarra-Castanedo :

a aidé pour l'établissement de L'expérimentation et sa réalisation, a aidé pour le traitement des résultats et leur analyse, ainsi que la correction du manuscrit

Xavier MALDAGUE :

directeur de la maitrise, supervision, révision, et correction de l'article.

Comparative study of linescan and flynig line Active IR thermography operated with a 6 axes robot

Cet article a été publié dans la conférence Quantitative Infrared Thermography (QIRT) 2018 en tant qu'article principal. Les contributions de chacun des co-auteurs sont détaillées dans ce qui suit :

Contributions des auteurs :

Yacine MOKHTARI :

auteur principal, a réalisé les différentes expérimentations à l'aide du robot ainsi que la programmation de ce dernier, a effectué le traitement des résultats et leur analyse, a effectué la comparaison des résultats des deux méthodes étudiées et analysé les résultats obtenus.

C Ibarra-Castanedo :

a aidé pour l'établissement de L'expérimentation et sa réalisation, a aidé pour le traitement des résultats et leur analyse, ainsi que la correction du manuscrit.

L Gavérina :

a aidé pour le traitement des résultats et leur analyse, ainsi que la correction du manuscrit

J Dumoulin :

supervision ainsi que le traitement des résultats, révision, et correction de l'article.

Xavier MALDAGUE :

directeur de la maitrise, supervision, révision, et correction de l'article.

Ces articles seront présentés en détail dans ce mémoire. De plus on présentera également deux articles où l'on est co-auteur dans l'annexe qui sont :

Optimised Dynamic line scan thermographic detection of CFRP inserts using FE updating and POD analysis

Il s'agit d'un article publié dans le journal NDT & E International 2017. On fait partie des co-auteurs. On présente ici notre contribution.

Contributions dans l'article :

Co-auteur, a réalisé les différentes expérimentations à l'aide du robot, a programmé le robot pour les tests ainsi que la calibration des différents capteurs utilisés.

Automatic dynamic inspection using active infrared thermography

Cet article a été soumis et accepté au journal IEEE transaction on industrial informatics 2018. On est co-auteur dans ce dernier et nos contributions sont les suivantes :

Contributions dans l'article :

Co-auteur, a réalisé les différentes expérimentations à l'aide du robot, a programmé le robot pour les tests ainsi que la calibration des différents capteurs utilisés.

Introduction

[1-5] L'aéronautique représente un secteur économique capital dans le monde. Les flux financiers générés par cette industrie se chiffrent en centaines de milliards de dollars. Plus encore, cette industrie a révolutionné plusieurs secteurs comme : le transport, le militaire, la conquête de l'espace,...etc. Très développée au Québec et au Canada avec des entreprises comme PRATT and WHINEY, L3-MAS, ou encore BOMBARDIER, ce secteur suscite un intérêt particulier pour la recherche et développement. La sécurité reste une priorité absolue et fait l'objet de recherches intensives visant à l'améliorer. Les procédés d'inspection des pièces d'appareils connaissent une évolution continue. L'objectif est de détecter les défauts qui peuvent altérer le bon fonctionnement d'une pièce ou d'un appareil avec précision tout en réduisant le coût d'inspection.

Les méthodes de contrôle non destructif (CND)((18)) sont des procédés qui permettent l'inspection de pièces sans altérer leur bon fonctionnement. Ces méthodes s'imposent comme les plus adaptées et sont parmi les méthodes d'inspection les plus utilisées en industrie aéronautique où les pièces coûtent cher et où l'on ne peut se permettre d'avoir même le plus petit des défauts. Différentes méthodes de contrôle non destructif existent comme : le ressuage (FPI), l'inspection par courant de Foucault (ECT), la thermographie, ultrasons...etc. Le choix d'une méthode à utiliser dépend du type de matériaux à inspecter (métal, matériaux composites ...etc.), et du type de défauts recherchés (fissures en surface, porosités, fissures sous la surface, défauts de soudures ...etc.). Dès lors, il est évident qu'une inspection complète d'une pièce donnée nécessite l'utilisation de plusieurs méthodes de CND. En pratique, une pièce passe plusieurs tests où on utilise différentes méthodes de CND avant d'être déclarée valide ou défectueuse. La plupart de ces méthodes de CND sont effectuées par un opérateur et leur précision dépend de sa capacité et de son expérience. De plus, certains problèmes qui surviennent dans certaines méthodes peuvent être évités si l'on utilise un système plus précis.
La thermographie est une méthode de contrôle non destructif très largement utilisée dans l'industrie. Le principe est d'exciter thermiquement une pièce en la chauffant ou en la refroidissant. Le flux de température est affecté par les discontinuités dans la pièce (défauts) ((20)). Une caméra thermique est utilisée pour détecter les changements qui représentent les défauts de la pièce. La thermographie infrarouge peut être passive quand aucune excitation

externe est utilisée ou active dans le cas où l'on utilise une source d'excitation((6)).
Les progrès de la robotique moderne avec des robots de plus en plus précis, fiables, et polyvalent ouvrent de nouvelles perspectives de recherches en aéronautique. En effet, des solutions avec des systèmes entièrement automatisés font l'objet de recherches intensives. Le but recherché est d'avoir une plateforme d'inspection automatisée qui permettrait de détecter des défauts de manière précise, rapide, et la moins couteuse possible. Plus encore, l'utilisation de systèmes robotiques permet de résoudre des problèmes qui surviennent lors d'une inspection manuelle. L'utilisation de robot permet aussi l'inspection de surfaces complexes et difficiles d'accès pour un opérateur.

Contexte

Cette recherche faisait initialement partie d'un projet du Consortium de Recherche et d'Innovation en Aérospatiale au Québec (CRIAQ) intitulé 'Automated non destructive testing for Aerospace industry' et référencé CRIAQ MANU-418 CRDPJ 395920 - 09. Le but de ce dernier était de développer un système automatisé combinant différentes méthodes de contrôle non destructif pour l'industrie aérospatiale. Il était en partenariat avec l'École Polytechnique de Montréal, lÉcole de Technologie Supérieure, l'Université CONCORDIA, et l'Université LAVAL. Comme partenaires industriels, le projet comptait également les entreprises PRATT and Whitney et L-3 MAS. Le projet étant fini et ayant intégré ce dernier à la fin, l'objectif de cette recherche a changé pour le développement dun système robotique pour l'inspection thermographique par chauffage inductif.

Ce projet est sous la supervision du Prof. Xavier MALDAGUE : chaire de recherche du Canada en vision infrarouge multipolaire. Ce dernier porte sur le développement d'une plateforme robotique pour l'inspection par thermographie par courants de Foucault en explorant toutes les possibilités d'inspection (linescan, mode photocopieuse,...etc.) et de comparer les résultats avec la thermographie optique (IRT). Plusieurs recherches portent sur l'utilisation de robots pour les méthodes de CND. Dans les travaux de ((8)), un robot KUKA arc KR5 HW est utilisé pour une inspection par ultrasons. Les résultats ont démontré la faisabilité d'une telle méthode. Plus encore, les résultats obtenus en utilisant un robot à 6 degrée de liberté couplé à une interface de traitement sont meilleurs que la méthode de scan conventionnelle pour les échantillons à géométrie simple utilisés. Les travaux de ((1), (14), (12),...etc.) montrent également des résultats très satisfaisant mais, à notre connaissance, aucune des recherches ne traite de la méthode linescan pour la thermographie par courants de Foucault. De plus, il s'agit d'investiguer les capacités de la méthode et de comparer les résultats avec la thermographie optique. C'est dans cette optique que s'inscrit ce projet de recherche.

Objectifs

Comme nous l'avons mentionné précédemment, l'objectif de ce projet est l'intégration de la méthode thermographie par courants de Foucault pour une plateforme robotique ainsi que l'exploration des capacités de la méthode. De plus, l'objectif est d'investiguer les différents modes d'inspection et le traitement des résultats afin d'améliorer ces derniers. Différents équipements sont à notre disposition tels que : une caméra infrarouge, une lampe halogène pour le chauffage optique, la bobine développée dans ((15)), et une autre bobine développée pour ce travail. Ces capteurs doivent être intégrés sur le robot à six degrée de liberté de type FANUC LrMate 200iD/7L.

Chapitre 1

État de l'art

Dans cette partie, nous allons expliquer la méthode de thermographie par courants de Foucault développée dans le cadre du projet. Nous présenterons également des travaux sur l'inspection automatique et lutilisation de robots pour les méthodes de contrôle non destructif.
L'état de l'art montre qu'il y a des travaux qui proposent une interface automatique d'inspection. Différentes méthodes de contrôle non destructif ont été automatisées ou bien ont été réalisées à l'aide d'un robot. La plupart des travaux dans la littérature, que ce soit en aéronautique ou dans d'autres domaines, proposent une méthode particulière qui a été automatisée et à notre connaissance, peu de travaux proposent l'automatisation de la thermographie par courants de Foucault et de manière aussi approfondie.

1.1 Revue de la littérature

Dans les travaux de ((11)), un système robotique est utilisé pour la détection et la caractérisation de fatigue par contact de roulement (RCF). Le système est composé de chariot mécanique, d'un bras robotique KAWASAKI FS02N, d'un capteur laser (pour mesurer le profil de rail) et d'un dispositif ACFM (alternating current field measurement) de TSC inspection systems. Une interface GUI est utilisée pour commander le rail, le robot, et gérer l'inspection. L'objectif est d'utiliser le robot pour deux tâches principales :

— **Établir le profil de rail** : Il s'agit d'établir le profil du champignon du rail car c'est là où se trouvent le plus souvent les défauts. Aussi, le but est d'assurer un lift-off constant lors du scan pour détecter le défaut. Le contact répété entre les rails et les roues peut déformer le rail de son profil initial. Un laser placé sur l'effecteur du robot est utilisé pour calculer les cordonnées verticales (distances entre l'organe terminal et le rail) tandis que les cordonnées horizontales sont prises du robot. Le tout est enregistré par l'interface GUI. À la fin, le profil du champignon du rail est établi et transféré au contrôleur du robot au moyen de l'interface.

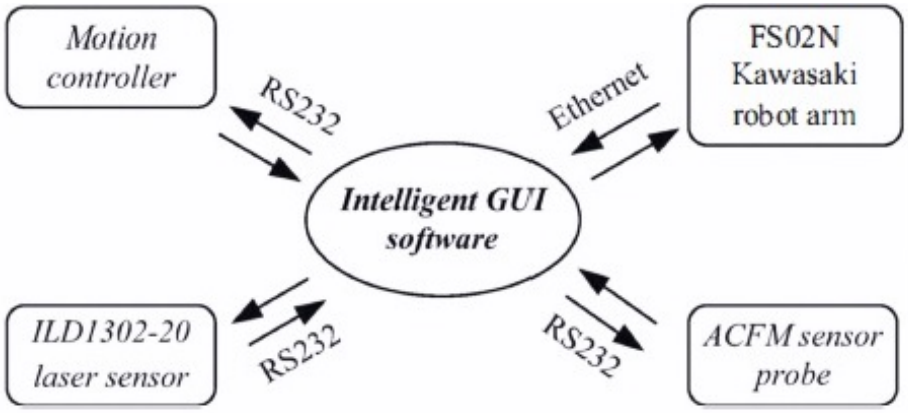

FIGURE 1.1 – Architercture du système ((11)).

— **Réaliser l'inspection du défaut** : Une fois le profil établi et le robot calibré, l'inspection peut être exécutée. La sonde ACFM est placée sur l'effecteur du robot. Les scans sont réalisés à un lift-off de 1mm et une vitesse du robot de 20mm/s. les résultats sont enregistrés et traités par le logiciel. Pour les tests, un UIC54 rail avec un défaut RCF artificiel est utilisé pour simuler le scenario où le système caractérise le défaut. Plusieurs scans ont été achevés avec différents angles de la sonde par rapport au défaut pour simuler un cas réel d'inspection où les fissures apparaissent à différents angles avec les rails. Une différence d'angles entre la sonde ACFM et le défaut conduit à une sous-estimation du défaut (pour plus d'informations voir ((10))). Pour chaque angle, les dimensions du défaut ont été estimées. Les résultats obtenus sont prometteurs. Il a été observé que le signal du ACFM était minimum au centre du défaut où le défaut est plus profond et maximum dans les extrémités où il est le moins profond. L'erreur d'estimation varie de 7% à 21%. Il est proposé de faire des scans 2D avec un angle moyen (52 dans (11)). Ensuite, l'angle réel du défaut est estimé et un autre scan est pratiqué avec cet angle entre la sonde et le rail. Un test sur un échantillon réel est proposé comme travaux futurs.

Outre le fait de proposer des résultats encourageant, il est intéressant de constater quelques similitudes dans le travail qui a été achevé dans cet article et ce que nous voulons faire dans ce projet. L'aspect le plus remarquable est l'intégration de capteurs et logiciels. En effet, ici une interface GUI a été développée pour permettre la gestion de tous les capteurs, le traitement des données, ainsi que le robot. La communication entre les capteurs et le PC est assurée par un câble RS232 et un câble Ethernet pour le robot (voir figure 1.1). Différents programmes ont été développés pour l'exécution des différentes tâches telles que : l'enregistrement des données, la commande du robot, la calibration du robot...etc. Un programme a été fait afin de calibrer le robot. L'utilisation d'un robot a permis de régler le problème du lift-off qui peut affecter le résultat des inspections ACFM de même que dans notre cas, comme nous allons le

voir dans les chapitres suivants, pour les méthodes d'inspections par courant de Foucault.

Pour résumer, le travail réalisé dans cet article présente beaucoup de points communs avec notre projet. Ici, il était question d'achever une méthode d'inspection de manière automatique avec tout ce que ça représente comme défis d'intégration.

Dans l'article ((8)), un robot manipulateur industriel à 6 degrée de liberté de type KUKA KR5 Arc HW est utilisé pour exécuter la méthode de CND d'inspection par ultrasons ((19)). Le but ultime de cette recherche est d'être capable d'achever une inspection (un scan) d'objets à géométries complexes de manière automatique avec peu ou pas de connaissances à priori sur ces derniers. L'inspection de pièces à géométries complexes pose beaucoup de problèmes. L'enregistrement manuel de points de la trajectoire (teaching) peut être ardu et nécessite que tous les points soient accessibles par l'opérateur. Une autre solution très largement utilisée est de calculer la trajectoire à partir du modèle CAD. D'autres solutions sont utilisées telles que l'utilisation d'un capteur laser ou de cameras (reconstruction 3D) pour retrouver la géométrie de l'objet dans le cas où le CAD n'est pas disponible. Dans ce travail, des expériences d'inspections par ultrasons ont été réalisées sur deux pièces à géométries simples. Le robot KUKA KR5 avec le contrôleur KCP2 (pour les spécifications du robot voir((8))) est utilisé pour exécuter les scans par ultrasons. Une sonde à ultrasons d'immersion de type V309 est fixée sur l'effecteur du robot (pour les spécifications de la sonde voir ((8))). Un émetteur-récepteur de type Parametrics 5052PR est utilisé pour actionner la sonde. L'acquisition des ondes ultrasoniques est assurée par un oscilloscope Tektronix DPO4054. Un PC assure le contrôle du robot et l'acquisition et le traitement des différents signaux grâce à un module E/S numérique Agilent U2121A (voir figure (1.2)). La première pièce à inspecter est une plaque en acier de dimension (100 mm x 70mm x 12mm). Quatre trous de 10mm de diamètre ont été percés près des coins et un trou de 7mm de diamètre percé à 50% au milieu de la pièce. La plaque est immergée dans un bassin d'eau avec le trou du milieu vers le bas (pour représenter un défaut sous la surface). La deuxième pièce est une plaque en polymère à renfort fibre de carbone (PRFC ou CFRP en anglais) de dimensions (18 mm x 25 mm x 4 mm) présentant un défaut au centre du à un impact. Les résultats obtenus montrent que les défauts ont été détectés avec succès dans les deux pièces. Dans la première pièce, les quatre trous (ceux proches des côtés) ont été détectés et le trou du milieu apparait clairement comme défaut sous la surface. Les résultats permettent même l'estimation de son diamètre (voir (8) pour plus de détails). Le défaut structurel sur la plaque en composite est clairement détecté. Ce qui démontre l'utilité de l'automatisation de cette méthode et est très prometteur pour l'inspection des pièces à géométries complexes.

Ce travail montre des résultats très intéressants sur l'automatisation de la méthode d'inspection par ultrasons pour les pièces à géométries simples. Ces résultats sont très prometteurs

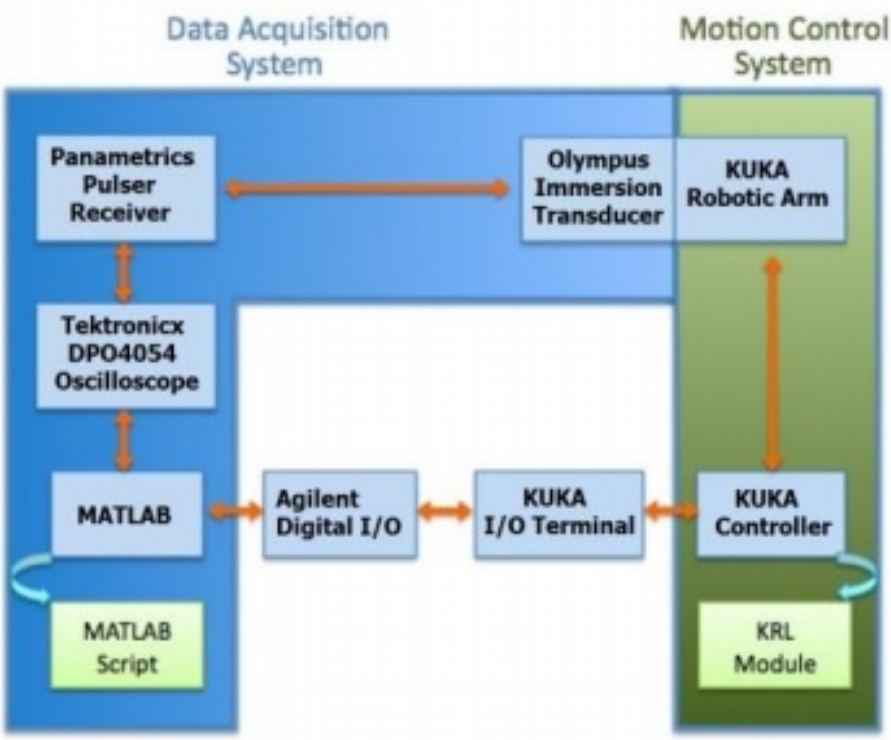

FIGURE 1.2 – Configuration du système ((8)).

quant à l'inspection des pièces à géométries complexes. Dans le cadre de notre projet, il est important de constater le travail fait sur l'intégration. En effet, le control du robot, la communication avec les capteurs et l'acquisition des signaux est assuré par un PC grâce à un module E/S numérique. Les signaux acquis subissent un traitement au moyen d'un script MATLAB. L'architecture du système (figure 1.2) est très similaire à ce que nous voulons faire dans ce projet.

1.2 Thermographie des courants de Foucault

La thermographie infrarouge (IR) ((6)) est une méthode de contrôle non destructif très utilisée dans l'industrie. Le principe de la méthode est d'exciter thermiquement une pièce en la chauffant ou en la refroidissant. Le flux de température est affecté par les discontinuités dans la pièce (défauts) ((20)). Une caméra thermique est utilisée pour détecter les changements qui représentent les défauts de la pièce. La thermographie infrarouge peut être passive quand aucune excitation externe est utilisée ou active dans le cas où l'on utilise une source d'excitation((6)).

La thermographie par courants de Foucault est une méthode de thermographie infrarouge active. L'excitation est une source inductive qui produit, grâce à la force électromagnétique, un courant (courant de Foucault) dans le matériau conducteur qui est inspecté ((16)). Ce courant va chauffer la pièce du fait de la résistance (pertes Joules). La présence de défauts perturbe la distribution de température due à la perturbation du flux de courant dans le matériau ((16)). Cette perturbation génère des régions plus chaudes autour des défauts qui sont observés à l'aide d'une caméra thermique. La figure suivante montre la configuration de la méthode : L'un des éléments important à prendre en compte est la profondeur de pénétration

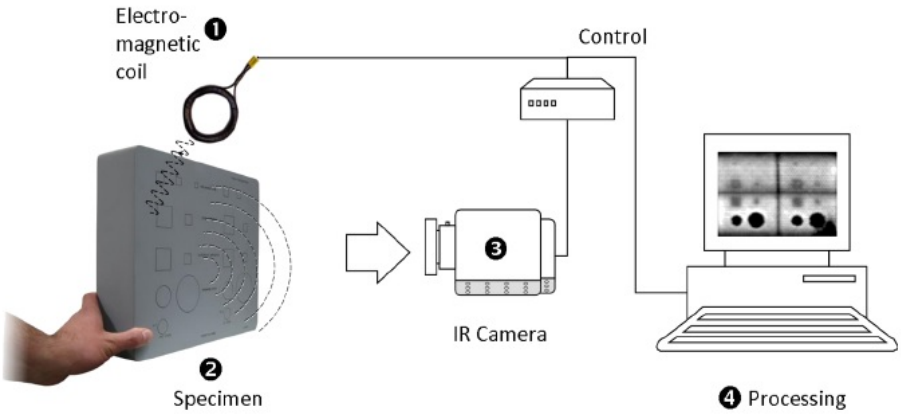

FIGURE 1.3 – Configuration de la thermographie des courants de Foucault((15)).

(skin depth). Il s'agit de la profondeur à laquelle le courant de Foucault "s'infiltre" dans la pièce inspectée. Cette entité dépend de la fréquence du champs magnétique qui génère le courant de Foucault, de la perméabilité du matériau de la pièce, ainsi que sa résistivité comme le montre l'équation suivante ((15),(18)) :

$$\delta = \sqrt{\frac{2\rho}{w\mu}}$$

Avec :
$w = 2\pi f$ la fréquence angulaire
$\mu = \mu_0\mu_r$ la perméabilité
ρ la résistivité
À partir de l'équation, on peut voir que la profondeur δ est inversement proportionnelle à la fréquence d'excitation (figure 1.4). Les avantages de cette méthode sont les suivants ((18)) :

- permet de détecter les défauts de surface et sous la surface
- Sensible aux petits défauts
- nécessite peu de préparation

Ainsi que les inconvénients suivants ((18)) :

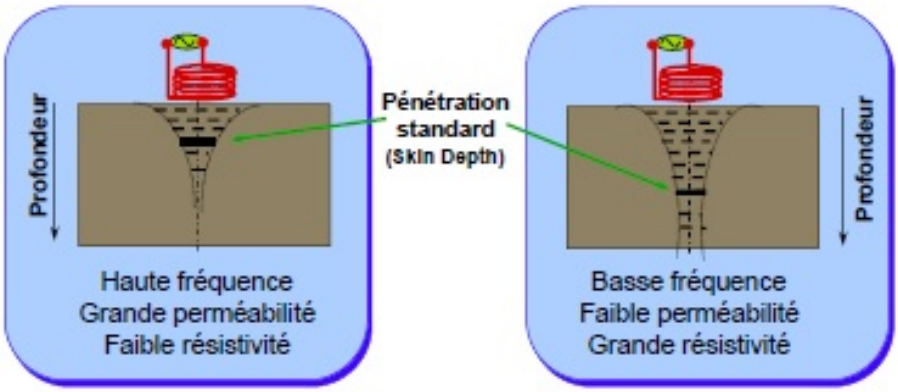

FIGURE 1.4 – Profondeur de pénétration (skin depth)((18)).

— Restreinte aux matériaux électriquement conducteurs

— les surfaces doivent être accessibles à la sonde

— la profondeur de pénétration est limitée

Chapitre 2

Modèlisation à l'aide de COMSOL Multiphysics

COMSOL Multiphysics est un logiciel de simulations de phénomènes physiques qui permet de résoudre des systèmes dépendant du temps ou stationnaire du second ordre dans l'espace des équations différentielles partielles dans une, deux ou trois dimension en se basant sur la méthode numérique des éléments finis pour la discrétisation spatiale (voir (15)). c'est un puissant outil pour résoudre des phénomenes complexes. La figure (2.1) représente l'environnement de travail de ce logiciel. Dans le cadre de cette recherche, COMSOL est utilisé pour

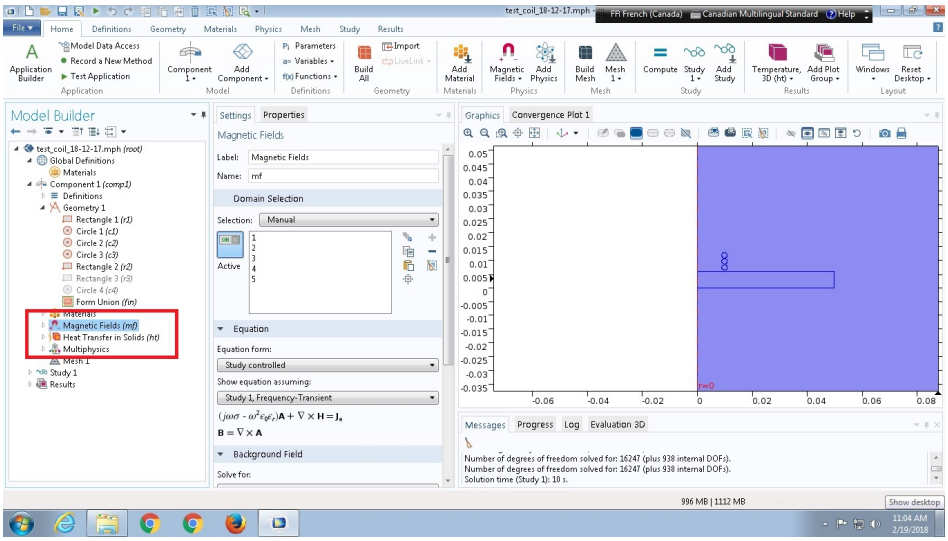

FIGURE 2.1 – Environnement de COMSOL (multiphysics encadré en rouge).

simuler la méthode de thermographie par courants de Foucault. Il s'agit d'un phénomène multi-physique car il faudra résoudre simultanément l'équation de propagation thermique et l'équation du champ magnétique (voir 2.1). La figure (2.2) montre le modèle COMSOL d'une telle méthode. Il s'agit d'une plaque en acier présentant une fissure chauffée par une bobine.

Les caractéristiques de ces derniers seront données dans le chapitre des résultats. Il est éga-

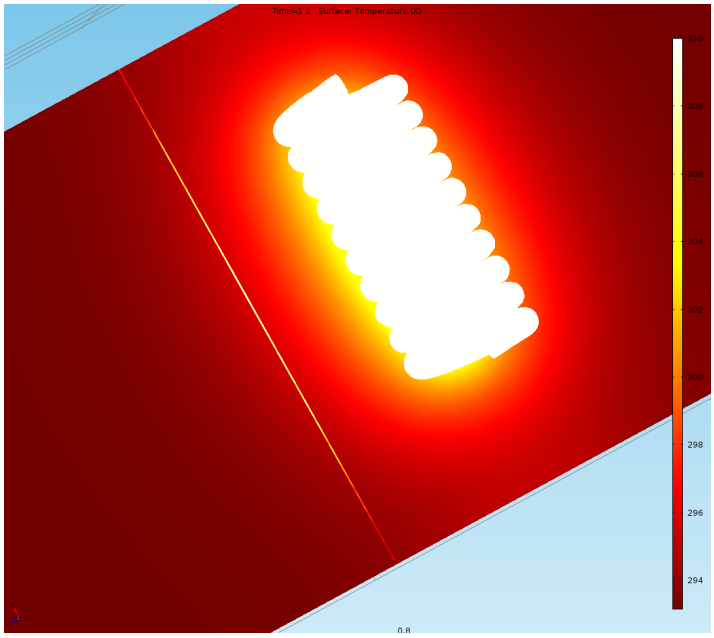

FIGURE 2.2 – Modèle COMSOL d'une plaque en acier chauffée par induction. On voit bien que la rainure à gauche est bien simulée

lement possible d'observer les courants de Foucault générés par la bobine. La figure (2.3) représente les courants de Foucault générés dans une plaque en acier excitée par une bobine à trois spires.

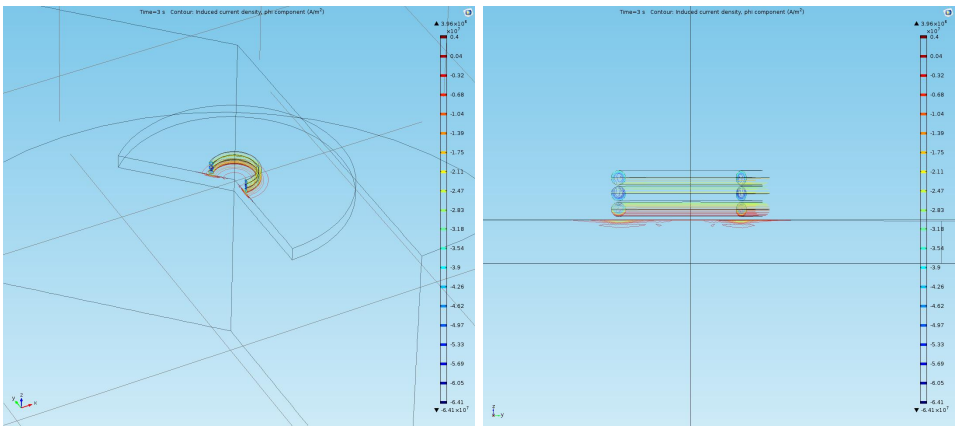

FIGURE 2.3 – Courants de Foucault dans une plaque en acier.

2.1 Principe théorique

La thermographie infrarouge (IR) ((6)) est une méthode de contrôle non destructif très utilisée dans l'industrie. Le principe de la méthode est d'exciter thermiquement une pièce en la chauffant ou en la refroidissant. Le flux de température est affecté par les discontinuités dans la pièce (défauts) ((20)). Une caméra thermique est utilisée pour détecter les changements qui représentent les défauts de la pièce. La thermographie infrarouge peut être passive quand aucune excitation externe est utilisée ou active dans le cas où l'on utilise une source d'excitation((6)).

2.1.1 Diffusion de chaleur

La thermographie s'appuie sur la diffusion de chaleur dans le matériau qui permet de déduire des informations concernant la structure et la composition de ce dernier ((13)). La diffusion de chaleur dépend de la structure et les propriétés thermiques du matériau. Les propriétés thermiques sont résumées à la figure 2.4. En présence de deux corps de températures différentes, ces derniers s'échangent spontanément leurs énergies jusqu'à atteindre l'équilibre thermique. Ce transfert de chaleur se fait par conduction ici (parfois aussi par : convection, ou rayonnement thermique ((17))).

Symbol	Term	Units (cgs)	Units (SI)
Q	Energy	cal	J
ρ	Density	g/cm^3	kg/m^3
κ	Thermal conductivity	cal/s cm K	W/m K
c	Specific heat	cal/g K	J/kg K
α	Thermal diffusivity	cm^2/sec	m^2/sec
e	Thermal effusivity	$cal/cm^2\,sec^{1/2}\,K$	$W.sec^{1/2}/m^2\,K$
Γ	Thermal mismatch factor	(numeric)	(numeric)
t_{trans}	Thermal transit time	sec or $sec^{1/2}$	sec or $sec^{1/2}$

FIGURE 2.4 – Propriétés thermiques ((13)).

Conduction thermique

En régime permanent, le transfert de chaleur par conduction se fait suivant l'équation suivante ((7)) :

$$q = kS(T_1 - T_2) \tag{2.1}$$

Avec : q la chaleur transférée d'une surface de température T_1 à une surface de température T_2, S surface perpendiculaire au flux de chaleur, et k la conductivité thermique.

Convection thermique

La convection thermique est un transfert de chaleur d'une surface à un fluide en mouvement. La convection est régie par l'équation suivante ((7)) :

$$q_c = hA_S(T_s - T_f) \tag{2.2}$$

Avec : q_c la chaleur transférée d'une surface de température T_s au fluide de température T_f, A_S est la surface, et h le coefficient de convection.

Rayonnement

Le rayonnement est un mode de transfert qui se fait par l'entremise d'un rayonnement électromagnétique (infrarouge). Un corps ayant une température supérieure au zéro absolu (0K, -273) émet des radiations à cause de l'agitation de ses électrons. L'augmentation de température augmente la fréquence et l'intensité des radiations. Les facteurs définissant la fraction de la radiation incidente absorbée α (absorbance), la radiation réfléchie ρ (réflectivité), et la radiation transmise τ (transmittance) sont reliés par l'équation suivante ((7)) :

$$\alpha + \rho + \tau = 1 \tag{2.3}$$

Transfert de chaleur unidimensionnel

La loi de Fourier est applicable dans le cas où la distribution de température dans le système atteint l'équilibre. Après bilans de toutes les sources de chaleurs et application du principe de conservation de l'énergie, l'équation dépendante du temps obtenue est dérivée.
Considérons une plaque d'épaisseur Δx, de densité ρ, et de chaleur spécifique c, de conductivité thermique k, et de surface A. La chaleur pénétrant la pièce en $x = 0$ par diffusion de chaleur dans un intervalle de temps ΔT est donnée par l'équation (2.4) :

$$Q_1 = J_1 A\Delta T = (-k\frac{\partial T}{\partial x})_{x=0} A\Delta T \tag{2.4}$$

et En $x = \Delta x$:

$$Q_2 = (k\frac{\partial T}{\partial x})_{x=\Delta x} A\Delta T \tag{2.5}$$

La chaleur provenant de la source d'excitation, H en (W/m^3) est :

$$Q_H = HA\Delta T\Delta x \tag{2.6}$$

Pour une augmentation de température, le changement de chaleur dans la plaque est donné par l'équation suivante :

$$\Delta Q = c\rho A\Delta x\Delta T \tag{2.7}$$

En considérant $Q_1 + Q_2 + Q_H = \Delta Q$ (chaleur totale de la plaque est égale à la somme des chaleurs provenant de la source et de la diffusion) et en mettant toutes les équations dans la dernière, on obtient (2.8) :

$$((k\frac{\partial T}{\partial x})_{x=\Delta x} - (k\frac{\partial T}{\partial x})_{x=0})A\Delta T + HA\Delta T\Delta x = c\rho A\Delta x\Delta T \tag{2.8}$$

En divisant (2.8) par $A\Delta T\Delta x$ et en prenant les dérivées pour des petits $\Delta t\Delta x$, on obtient :

$$k\frac{\partial^2 T}{\partial x^2} - c\rho\frac{\partial T}{\partial t} = -H \tag{2.9}$$

Sachant que la diffusivité thermique est égale à :

$$\alpha = \frac{k}{c\rho} = \frac{conductivitthermique}{chaleurspecifiquedensit}$$

L'équation différentielle de conduction de chaleur unidimensionnelle est donnée par l'équation (2.10) :

$$\frac{\partial^2 T(x,t)}{\partial x^2} - \frac{1}{\alpha}\frac{\partial T(x,t)}{\partial t} = -\frac{H(x,t)}{k} \tag{2.10}$$

2.1.2 Émissivité

Corps noir

Un corps noir est un radiateur thermique idéal (théorique). Ce dernier a la capacité d'absorber toutes les radiations incidentes indépendamment de leurs longueur d'ondes (ou fréquence) et de l'angle d'incidence. De la même manière, il est capable de réémettre toutes ces radiations de manière uniforme. La radiance thermique $N_{\lambda,b}$ d'un corps noir en équilibre thermique à une température T est définie par la loi de Planck ((2)) :

$$N_{\lambda,b} = \frac{2hc^2}{\lambda^5 exp(\frac{hc}{\lambda kT} - 1)} \tag{2.11}$$

Avec : h la constante de Planck ($6.626x10^{-34}J.s$), c la vitesse de la lumière, k la constante de Boltzmann, λ la longueur d'onde de la radiation émise, et T la température du corps noir.

Émissivité

L'émissivité est une propriété de la surface d'un matériau qui représente le pourcentage d'un flux thermique généré par rapport au flux thermique généré par un corps noir à la même température. L'émissivité d'une surface entre dans le calcul de sa température ((17)).

$$\varepsilon = \frac{q(T)}{q_0(T)} \tag{2.12}$$

2.1.3 Courants de Foucault

De ce qui a été dit dans la section précédente, une bobine alimentée d'un courant alternatif produit un champ magnétique. Si un conducteur électrique se trouve à proximité de ce champ, des courants seront générés dans le conducteur. On parle alors de courants de Foucault. Ces courants dépendent : des propriétés électromagnétiques du matériau qui sont σ la conductivité électrique et μ la perméabilité magnétique, de la fréquence d'excitation de la bobine f, et des paramètres géométriques de la bobine comme le nombre de spire N, diamètre du fil, surface de la boucle, distance de retrait et de l'échantillon testé comme l'épaisseur, formes, proximités de la sonde aux coins...etc. ((13)). Quand les courants de Foucault sont générés, ces derniers produisent à leur tour un champ magnétique qui va s'opposer au champ magnétique primaire ce qui a pour effet d'affaiblir le champ magnétique net (global) et causer une baisse des courants avec la profondeur de pénétration. Aussi, les courants de Foucault en surface bloquent partiellement la pénétration sous la surface du champ magnétique de la bobine. De manière générale, la densité des courants de Foucault décroit avec la profondeur. La profondeur de pénétration ou "skin depth" décrit cette décroissance. La profondeur de pénétration dépend de la perméabilité magnétique μ, la conductivité électrique σ, et de la fréquence d'excitation f de la bobine. La densité de courants de Foucault J induits par une bobine excitée par une source sinusoïdale en n'importe quel profondeur x est donnée par l'équation (2.13) :

$$j = J_0 e^{-x\sqrt{\pi\mu\sigma f}} sin(\omega t - -x\sqrt{\pi\mu\sigma f}) = J_0 e^{-(i+j)(x\sqrt{\pi\mu\sigma f})} e^{j\omega t} \tag{2.13}$$

Avec :
J_0 à la surface, $e^{-x\sqrt{\pi\mu\sigma f}}$ représente la décroissance de l'intensité avec l'augmentation de la profondeur x, $e^{-j(x\sqrt{\pi\mu\sigma f})}$ représente le déphasage avec l'augmentation de x. Le standard skin depth δ est la profondeur x à laquelle la densité de courant est atténuée de e^{-1} c.-à-d. $36,8\%$ de la valeur J_0, et la phase est changée de $1rad$ $(57,29)$. Ce qui donne (2.14) :

$$\delta = \frac{1}{\sqrt{\pi\mu\sigma f}} \tag{2.14}$$

$$J = J_0 e^{-x/\delta} e^{-j(x/\delta)} e^{-\omega t} \tag{2.15}$$

2.1.4 Chauffage par induction

La thermographie par courants de Foucault est une méthode de thermographie infrarouge active. L'excitation est une source inductive qui produit, grâce à la force électromagnétique, un courant (courant de Foucault) dans le matériau conducteur qui est inspecté ((16)). Ce courant va chauffer la pièce du fait de la résistance (pertes Joules). La présence de défauts perturbe la distribution de température à cause de la perturbation du flux de courant dans le matériau ((16)). Cette perturbation génère des régions plus chaudes autour des défauts qui sont observées à l'aide d'une caméra thermique.

Modèle mathématique

Le modèle mathématique d'une induction électromagnétique est donné par les équations de Maxwell, la loi dOhm, ainsi que d'autres équations essentielles ((5)) :

$$B = \nabla xAE = -\nabla V - \frac{\partial A}{\partial t} \tag{2.16}$$

La loi d'Ampère peut s'écrire sous la forme de :

$$\sigma \frac{dA}{dt} + \nabla \times \mu^{-1} \nabla \times A + \sigma \nabla V = J^e + \varepsilon \frac{d^2 A}{dt^2} \tag{2.17}$$

Avec :
E l'intensité du champs électrique (V/m),B la densité du flux magnétique (T), A le vecteur de potentiel magnétique, V la potentiel électrique, J la densité du courant externe, ε la permittivité du milieu $(F/m) = \varepsilon_0 \varepsilon$ ou ε_r la permittivité relative et ε_0 de l'espace libre, et σ la conductivité électrique (S/m).
Le gradient de potentiel, pour une structure à symétrie axiale avec les courants circulant seulement dans une direction angulaire et dans ce cas en considérons juste la composante A_φ du potentiel magnétique, s'exprime comme suit :

$$\nabla V = \frac{-V_{loop}}{2\pi r} \tag{2.18}$$

Le champ électrique étant présent seulement dans la direction azimute, V_{loop} représente la différence de potentiel pour un tour sur l'axe Z. Pour l'analyse harmonique $A = A_\phi e^{j\omega t}$, 2.17 s'écrira comme :

$$(j\omega\sigma - \omega^2 \varepsilon_0 \varepsilon_r) A + \nabla \times (\mu^{-1} \nabla \times A_\varphi) = \sigma \frac{V_{loop}}{2\pi r} + J^e_\varphi \tag{2.19}$$

Les conditions aux limites sont l'isolation magnétique limites du domaine

$$A_\varphi = 0 \tag{2.20}$$

Et la continuité du champ magnétique à l'intérieur des limites

$$n \times (H_1 - H_2) = 0 \tag{2.21}$$

La chaleur générée dans la plaque (l'échantillon testé) est donnée par :

$$Q = 1/2\sigma \left|E\right|^2 \tag{2.22}$$

L'équation de transfert de chaleur dans le cas de symétrie axiale est donnée par :

$$\frac{1}{r}\frac{\partial}{\partial r}(kr\frac{\partial T}{\partial r}) + \frac{\partial}{\partial z}(k\frac{\partial T}{\partial z}) + \dot{q} = \rho C_p \frac{\partial T}{\partial t} \tag{2.23}$$

Avec :
ρ la densité (kg/m^3), C_p la chaleur spécifique $(kg/j.K)$, T la température (K), et k la conductivité thermique $(W/m.K)$.
Les conditions aux limites du domaine

$$T = T_{ambiante} \tag{2.24}$$

Et le flux de températures aux autres limites :

$$k\frac{\partial T}{\partial n} = h(T_\infty - T) + \varepsilon\sigma(T_a^4 - T^4) \tag{2.25}$$

Avec h coefficient de convection $(W/m^2.K)$, T_∞ la température ambiante, et ε est l'émissivité, et σ est la constante de Stefan-Boltzmann $= 5.6710^{-8} W/m^2K^4$.

2.1.5 Effet de la conductivité électrique et de la fréquence du courant inducteur sur l'intensité et la distribution des courants de Foucault

Effet de la conductivité Électrique

Considérons une variation de la conductivité σ de 0 à ∞. Lorsque $\sigma = 0$, Il n'y aura pas de courants de Foucault générés. À $\sigma = \infty$, il n'y aura pas de pertes résistives et les courants de Foucault générés induiront un champ magnétique égal et opposé au champ magnétique primaire. Entre les deux extrêmes, avec l'augmentation de la conductivité, les pertes résistives vont croitre de manière proportionnelle aux courants de Foucault générés. À un certain moment, l'augmentation de la densité des courants de Foucault avec l'augmentation de la conductivité va prendre le dessus sur les pertes résistives et si on était dans un cas d'inspection par courant de Foucault, la résistance R (normalisée) dans la pièce inspectée va décroitre jusqu'à atteindre une valeur nulle. Une résistance nulle implique pas de pertes Joules et donc pas de chauffage. La figure 2.5 représente l'effet de la conductivité sur l'impédance (normalisée) d'une sonde d'inspection par courant de Foucault (Dans le cas de la thermographie par induction, il s'agit d'une bobine mais les résultats restent le même).

Pour ce qui est de la distribution des courants de Foucault dans la pièce, il est évident d'après l'équation de la profondeur de pénétration δ que cette dernière est inversement proportionnelle à la conductivité. En d'autres termes, plus la conductivité est élevée, plus les courants de Foucault auront tendance à être concentrés en surface. On va voir dans la section suivante que l'effet de la conductivité est le même que celui de la fréquence du courant inducteur sur l'intensité et la distribution des courants de Foucault.

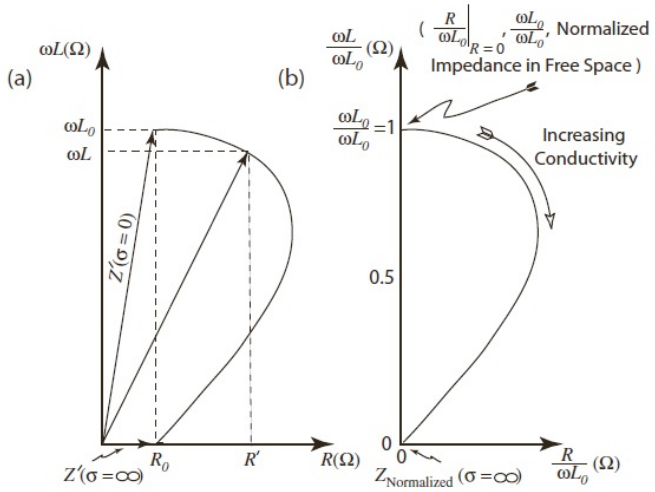

FIGURE 2.5 – Effet de la conductivité électrique sur l'impédance de la sonde : (a) non-normalisée (b) normalisée ((13)).

Effet de la Fréquence du courant inducteur

Comme il a été cité dans la section précédente, la fréquence d'excitation (du courant inducteur) a le même effet que la conductivité électrique sur les courants de Foucault. Considérons une variation de la fréquence de 0 à ∞. À 0, il y aura un champs magnétique DC (continu) et donc pas de courants de Foucault. Quand $f = \infty$, Les courants de Foucault sont concentrés en surface et il y aura un echauffement en surface. Les courants de Foucault induiront un champ magnétique d'amplitude égale au champ primaire mais il y sera opposé et les deux vont s'annuler. Comme on peut le voir sur la figure 2.6, la trajectoire de l'impédance d'une sonde d'inspection quand la fréquence augmente est la même que pour l'augmentation de la conductivité électrique. Pour ce qui est de la distribution des courants, On peut voir d'après les équations de J de δ que les basses fréquences auront une plus grande profondeur de pénétration et inversement.

2.1.6 Effet de la perméabilité magnétique

Les matériaux paramagnétique et diamagnétique possèdent une perméabilité relative $\mu_r \geq 1$ et $\mu_r \leq 1$ respectivement. Ce sont des matériaux à faible perméabilité magnétique ce qui

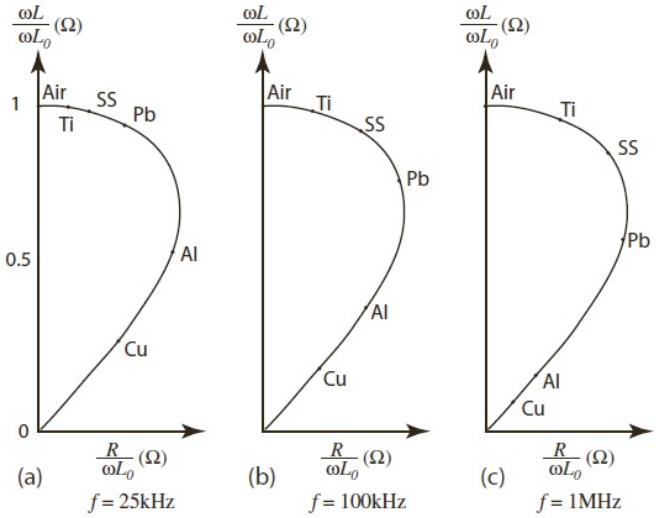

FIGURE 2.6 – Effet de la fréquence sur l'impédance de la sonde : (a) 25kHz (b) 100kHz (c) 1MHz ((13)).

implique une grande profondeur de pénétration pour les courants de Foucault. Dans ce cas, la profondeur de pénétration des courants de Foucault dépend plus de la conductivité électrique σ et la fréquence d'excitation f. Lorsque une bobine se trouve à proximité d'un matériau ferromagnétique (perméabilité $\mu >> 1$), Ce dernier va concentrer le flux magnétique primaire (de la bobine). Une augmentation du flux magnétique primaire va "éclipser" le flux magnétique secondaire (généré par les courants de Foucault).La tension générée dans le matériau est proportionnelle au flux primaire. Ce qui aura pour conséquence un courant d'intensité plus importante. Pour ce qui est de la distribution des courants, l'augmentation de la perméabilité magnétique est inversement proportionnelle à la pénétration des courants de Foucault (équation 2.14).

2.1.7 Phénomènes physiques participant à la production de chaleur dans la pièce inspectée

Du fait de la résistance du matériau de la pièce inspectée, la circulation des courants de Foucault de la pièce induit des pertes dissipées sous forme de chaleur (pertes par effet Joules) ce qui permet de chauffer la pièce inspectée. Lorsqu'un courant circule dans un conducteur, la résistance de ce dernier à la circulation du courant cause des pertes sous formes de chaleur. La puissance perdue est exprimée par l'équation suivante :

$$P = RI^2 \tag{2.26}$$

La loi de Joule (effet Joule) exprime la relation entre la chaleur générée par la résistance R à la circulation d'un courant I :

$$Q = RI^2t \tag{2.27}$$

Avec : Q la chaleur générée par la résistance un conducteur de résistance R au courant I circulant durant un temps t.
Dans les matériaux ferromagnétique (et ferrimagnétique) la chaleur provient également des pertes par hystérésis. Quand un matériau magnétique est chauffé, le flux magnétique alternatif provoque une oscillation du dipôle magnétique du matériau avec le changement des orientations des pôles. Cette oscillation est appelée Hystérésis et les frictions causées par cette dernière génèrent une quantité mineure de chaleur. Dans la thermographie par courants de Foucault, les pertes par Hystérésis sont généralement négligées car moins importantes que les pertes Ohmiques.
La chaleur générée par induction se propage dans la pièce inspectée principalement par le phénomène de conduction (section 2.1.1).

Chapitre 3

Plateforme robotique

3.1 Robot FANUC lrMate 200iD/7L

Il s'agit du bras manipulateur à 6 DDL de la firme FANUC. Ce robot soulève une charge de 7Kg et a un rayon d'action de 911 mm (voir figure). Le robot est montré par la figure (3.2).

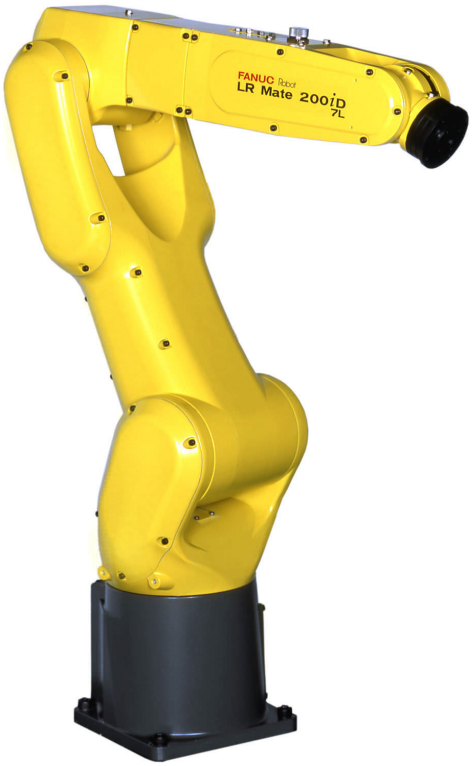

FIGURE 3.1 – Robot FANUC LrMate 200iD/7L (4).

Les caractéritiques sont représentées par la figure 3.2

Modèle		LR Mate 200iD/7L
Axes contrôlés		6
Contrôleur		R-30iB
Charge embarquée maximum au poignet [kg]		7
Répétabilité [mm]		0.03
Poids [kg]		27
Enveloppe de travail [mm]		911
Amplitude de mouvement [°]	Axe 1	340/360
	Axe 2	245
	Axe 3	420
	Axe 4	380
	Axe 5	250
	Axe 6	720
Vitesse maximum [°/s]	Axe 1	370
	Axe 2	310
	Axe 3	410
	Axe 4	550
	Axe 5	545
	Axe 6	1000
Moment [Nm/kgm²]	Axe 4	16.6/0.47
	Axe 5	16.6/0.47
	Axe 6	9.4/0.15

FIGURE 3.2 – Caractéristiques du Robot FANUC LrMate 200iD/7L (4).

Le robot vient habituellement avec le contrôleur R-30iB. Dans notre cas, on a préféré avoir le contrôleur R-30iB OpenAir cabinet moins encombrant et destiné à être monté sur des racks ce qui le rend facile à déplacer. Le contrôleur est montré à la figure 3.3 :

FIGURE 3.3 – contrôleur R-30iB OpenAir Cabinet (4).

C'est la nouvelle génération de contrôleur de FANUC. Il vient avec le logiciel HandlingPro qui offre différentes fonctions pour controler le robot. Le contrôleur dispose également d'option IrVision "plug and play" pour gérer des caméras. La communication avec le PC se fait via

câble Ethernet. Grâce au HandlingPro, il est aussi est possible de faire des simulations Offlines Dans un environnement 3D.

3.1.1 Roboguide et HandlingPro

HandlingPro est un logiciel de simulation de la firme FANUC pour les différents programmes et tâches à effectuer avec le robot. Il s'agit d'un environnement virtuel de travail avec le robot avec toutes les caractéristiques et les fonctionnalités du robot. Ceci permet de tester les différentes tâches assignées au robot dans le simulateur afin d'éviter tout problème qui peut survenir à l'exécution avec le robot. La figure suivante montre l'environnement de travail du HandlingPro :

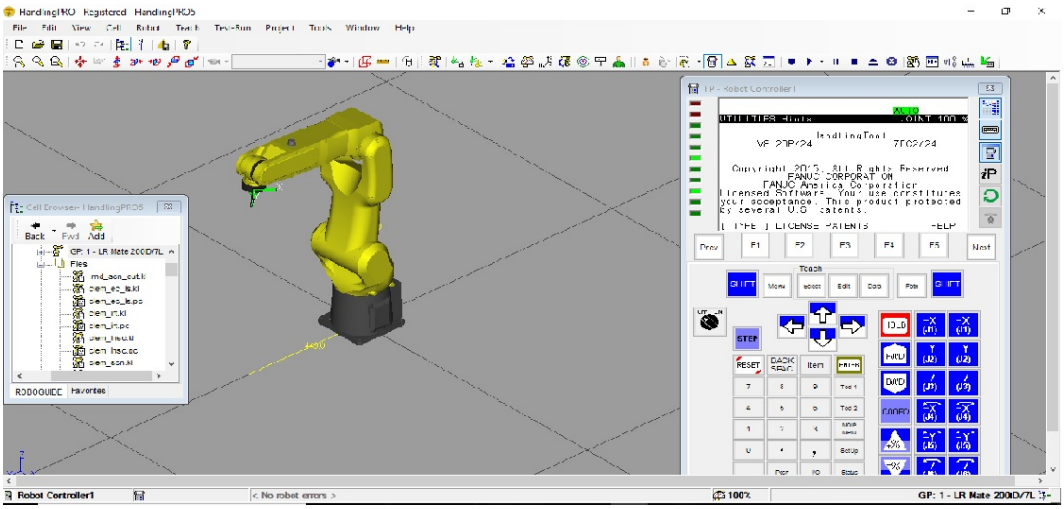

FIGURE 3.4 – Environnement du HandlingPro (4).

Comme le montre la figure (3.4), l'environnement dispose d'un teach Pendant virtuel, d'un onglet contrôleur pour ajouter des programmes, changer de référentiels, etc. Il est également possible d'ajouter des tables, rails, ou obstacles afin de bien représenter l'environnement de travail réel du robot.

3.1.2 Calibration du robot

Habituellement, les robots viennent calibrés ou mastered. Cette calibration est communément appelée intégration en robotique. Outre le fait de charger les programmes nécessaires au bon fonctionnement du contrôleur, cette procédure comprend la calibration des articulations du robot. En d'autres termes, déterminer la position zéro de chaque encodeur de l'articulation. On parle alors de zero mastering. Cette procédure est détaillée dans le manuel d'utilisation du robot ((4)). Elle est indispensable au fonctionnement du robot.
Une fois la calibration réalisée, une autre étape est primordiale. Il s'agit de déterminer les

limites de chaque articulation afin d'éviter des positions anormales des articulations. Ce qui pourrait causer des dommages à ce dernier. Nous avons réalisé l'intégration et la calibration du robot nous-même.

3.1.3 Programmation du robot

Une fois la calibration achevée, le robot est prêt à l'utilisation. La programmation du robot se fait avec le langage de programmation Karel. C'est un langage propre à la firme FANUC. La figure suivante montre la structure type d'un programme Karel :

```
PROGRAM ECT_traj
%COMMENT = 'ECT_pth_insp'

-- declaration des variables
CONST
pas =80
nbr_axe = 6
nbr_pts = 7


VAR
idx : INTEGER
pos_rl :  XYZWPR
tmp_p :ARRAY[nbr_axe] OF REAL
statu : INTEGER
tmp_r : REAL
tmp_jp : JOINTPOS6
traj_1 : ARRAY[nbr_pts] OF XYZWPR
ref_pos : XYZWPR
path_1 : PATH
length : INTEGER


-- declaration des routines
ROUTINE MOV_TO_PR FROM MOV_TO_PR
ROUTINE MOVEL_TO_PR FROM MOVEL_TO_PR

BEGIN
    -- INIT


   FOR idx = 1 TO nbr_axe DO
        tmp_p[idx] = 0
   ENDFOR
END
```

FIGURE 3.5 – Structure d'un programme Karel.

Comme le montre la figure (3.5), le programme se décompose en trois parties comme suit :

— Déclaration des variables

— Déclaration des routines (comparable à des fonctions)

— Le contenu du programme

Dans la programmation, il est possible de générer une trajectoire de plusieurs façons différentes. La solution choisie pour ce travail est l'utilisation de la variable PATH qui offre la façon la plus complète de programmer. La variable PATH comprend des nuds qui assemblés représentent la trajectoire complète. Elle offre également la possibilité de gérer les orientations

de l'effecteur ainsi que la manière de gérer le coude du robot (par exemple si lon veut que le coude soit à gauche ou à droite, en haut ou en bas).

3.2 Appareillages utilisés

3.2.1 Bobine pour la thermographie des courants de Foucault

Il s'agit de la bobine utilisée dans les travaux de ((15)). La bobine est montrée à la figure suivante :

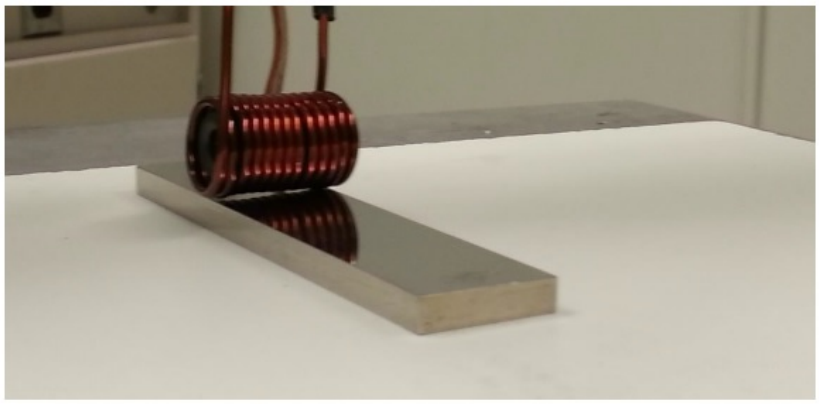

FIGURE 3.6 – Bobine utilisée dans ((15)).

Les caractéristiques de la bobine sont définit dans le tableau suivant : Il est à noter que

Parametres	valeurs
Courant	10A
Nombre de tours de la bobine	10
Rayon du fil de la bobine	1mm
Rayon de la bobine	3mm
Distance entre la bobine et la pièce	5mm
matériel de la bobine	cuivre

TABLE 3.1 – Caractéristiques de la bobine ((15))

la thermographie par courants de Foucault exige, en plus d'une caméra IR et de la bobine, différents instruments : amplificateurs, transformateur,...etc. Ceux ci sont décrits en détails dans ((15)).

3.2.2 Caméra thermique FLIR A65

C'est une caméra infrarouge de type Micro-bolomètre. Elle est equipée d'une lentille de 13mm (45x 37). Le tableau suivant détaille les caractèristiques de la caméra :

IR resolution	640 x 512 pixel
object temp range	-25 to +135
Thermal sensitivity/ NETD	< 0.05 @ +30
Focal plane array spectral range heightImage rate	uncooled VOX microbolometer/7 -13 30 Hz
operating temp range	-15to 60
weight	0.21 kg
external power operation	12/24VDC , < 3.5W (nominal) < 6.0W absolute max,

TABLE 3.2 – Caracteristiques de la A65

FIGURE 3.7 – FLIR A65.

3.2.3 Caméra Thérmique FLIR A655sc

Le tableau suivant montre les caracteristiques de la Caméra :

FIGURE 3.8 – FLIR A655sc.

IR resolution	640 x 480 pixel
standar temp range	-40 to +150
NETD/	<30mK
Focal plane array spectral range heightImage rate	uncooled microbolometer/7.5 -14 50 Hz
operating temp range	-15to 50
weight	0.9 kg
external power operation	12/24VDC, 24W absolute max

TABLE 3.3 – Caracteristiques de la A655sc

3.2.4 Système de chauffage par induction

Il s'agit d'un système de chauffage par induction similaire à celui de ((15)). La figure (3.9) représente le système. pour résumer, il s'agit d'un circuit RLC. Le système est équipé d'un génerateur haute fréquence de type Labjack U6, un amplificateur de de fréquence, et un circuit d'adaptation d'impédence (couplé au condensateurs). Le tout est dans un seul boitier (voir figure 3.9 (à la différence du système de (15)). Il est possible de changer la fréquence de résonnance en changeant les capacités (circuit RLC). Le système dispose également d'une interface pour contrôler les fréquences et démarrer la chauffage à partir du PC. Le dispositif est équipé d'une bobine (figure 3.10) avec 10 spires et un fils multi-brain en cuivre. La bobine a une inductance de $25.7\mu H$ à vide.

FIGURE 3.9 – Système de Chauffage par induction.

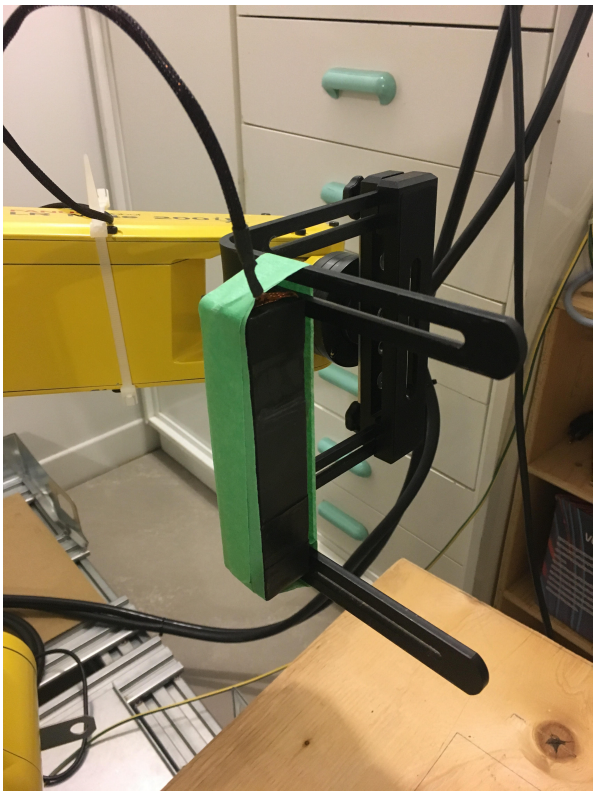

FIGURE 3.10 – bobine de Chauffage par induction.

Chapitre 4

thermographie Robotique par courants de Foucault : simulations et expérimentations

(publié dans quantitative infrared thermography conférence (QIRT), 2016)

4.1 Résumé

Cet article présente une application robotique de l'inspection par thermographie par courants de Foucault. Des simulations sont achevées grâce à COMSOLMultiphysics en variant plusieurs paramètres (fréquence d'excitation et Lift-off). Les expérimentations sont faites sur une plaque en aluminium (voir l'article pour plus d'informations) avec différents défauts à l'aide du robot. La pièce est finalement reconstruite ((3)).

4.2 Abstract

Eddy current thermography (ECT) is an active thermography method. The inductive excitation generates Eddy currents in an electrically-conductive specimen. In presence of defects, the eddy current flow is affected by these discontinuities leading to changes in the temperature distribution in the specimen around the defects. These changes are observed by an infrared camera. In this paper, we present a robotic application of the method. Simulations are performed using COMSOLő Multiphysics by varying different parameters. Experiment is realised on an aluminum plate with cracks of different sizes created artificially in our laboratory. The resulting images are reconstructed with a dedicated algorithm.

4.3 Simulations COMSOLMultiphysics

Il s'agit de simuler le chauffage par induction (courants de Foucault) de la plaque en aluminium en faisant varier la fréquence d'excitation du courant ainsi que le lift-off (la distance entre la bobine et la surface de la pièce). Les figures suivantes montrent les résultats de simulations avec les différents paramètres :

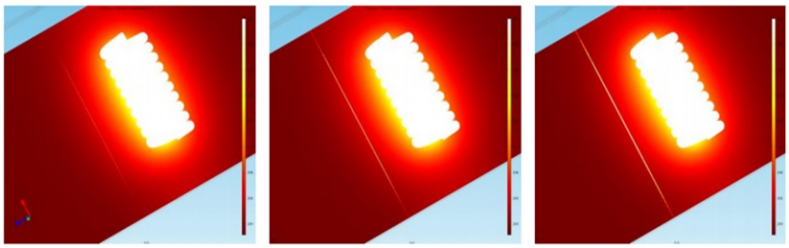

FIGURE 4.1 – Résultats de simulations avec f=100 KHz et T=1s (temps de chauffage) : gauche (défaut w (largeur) =0.2mm, d (profondeur)=0.2mm), Milieu (défaut w=0.5mm, d=0.5mm), droite (défaut w=1mm, d=1mm).

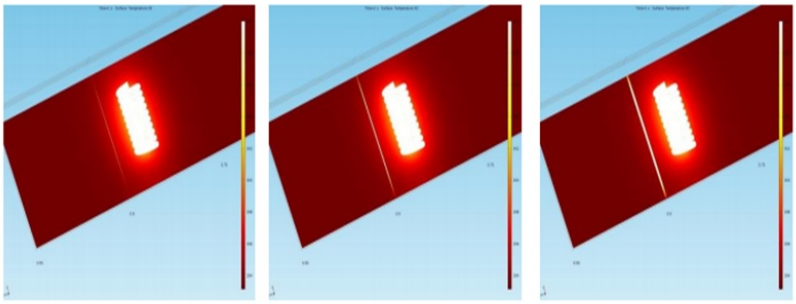

FIGURE 4.2 – Résultats de simulations avec f=200 KHz et T=1s (temps de chauffage) : gauche (défaut w (largeur) =0.2mm, d (profondeur)=0.2mm), Milieu (défaut w=0.5mm, d=0.5mm), droite (défaut w=1mm, d=1mm).

À partir des résultats de simulations, on peut observer que les défauts sont clairement visibles. On obtient de meilleurs résultats en utilisant une fréquence d'excitation **f=200 KHz** qui est la fréquence à utiliser pour inspecter ce type de matériau avec notre bobine. Il est également intéressant de noter que plus la distance entre le spécimen et la bobine (lift-off) est importante, moins le défaut est clair. Ceci est dû au fait que le champs magnétique autour du défaut décroit avec la bobine de ce dernier. Ce qui a pour effet de décroitre les courants de Foucault générés autour du défaut. Les courants étant plus faibles, la chaleur générée par ces derniers par effet résistif (joule) ou par la présence de discontinuités (défaut) est moins importante.

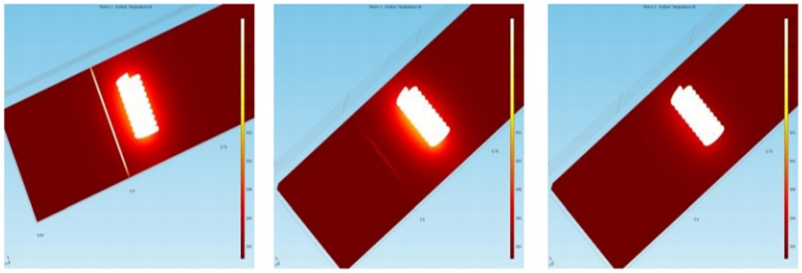

FIGURE 4.3 – Résultats de simulations avec f=200 KHz, défaut w=1mm, d=1mm, and T=1s (temps de chauffage) : gauche (position de la bobine P=0.5cm loin du défaut, lift-off = 3mm), Milieu (P = 2.5cm,lift-off=3mm), droite (P=2.5cm,lift-off =7mm).

4.4 Résultats expérimentaux

La figure (4.4) représente le montage expérimental pour la thermographie par courants de Foucault : La pièce inspectée est une plaque en aluminium avec des rainures de (0.2mm,

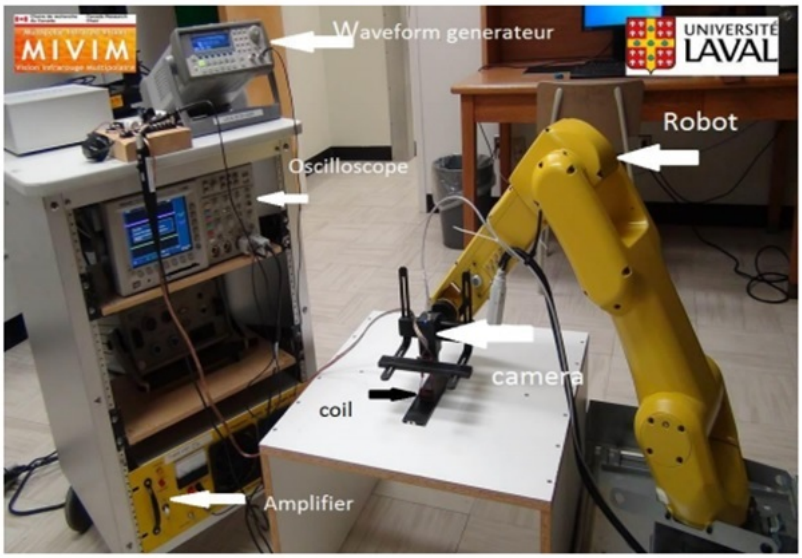

FIGURE 4.4 – Montage expérimental de la thermographie par courants de Foucault

0.5mm, et 1mm). Ces derniers ont été crées artificiellement au laboratoire. La pièce a été peinte en noir (pour augmenter l'emissivité). L'inspection est réalisée à l'aide d'un robot à 6 axes FANUC LrMate iD200/7L. La fréquence d'excitation des courants est f=200KHz.C'est la fréquence qui donne les meilleurs résultats pratique. Ce qui coincide avec les résultats obtenus en simulations. La vitesse d'inspection du robot est V= 10mm/s et le lift-off est de 3mm (voir 4). Les résultats de l'expérimentation sont donnés par la figure suivante : La plaque est ensuite reconstruite grâce à une reconstruction Pseudo-Static ((3)). La figure (4.6) montre le résultat de cette reconstruction :

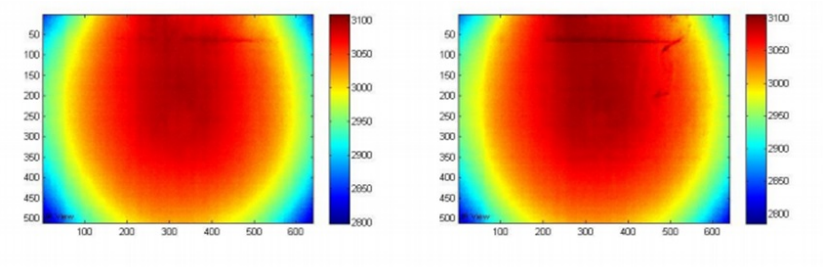

FIGURE 4.5 – Résultats d'inspection : défaut de 0.5mm (gauche), défaut de 1mm (droite)

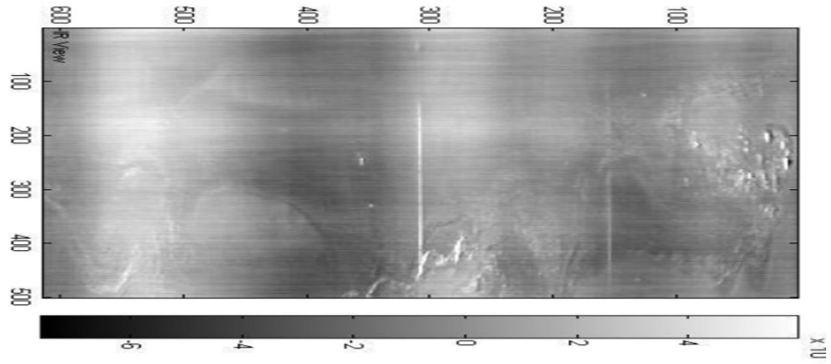

FIGURE 4.6 – Reconstruction Pseudo-static

On constate que les défauts de profondeur et largeur égale à 0.5mm et 1mm ont été parfaitement détectés. Le temps d'inspection est de 25 secondes pour un spécimen de 25cms. Le temps d'inspection a été réduit dans les travaux qui vont suivre. La pièce a été reconstruite d'après les images du linescan en utilisant un algorithme de reconstruction pseudo-Static((3)). Le résultat est amélioré en utilisant la PCT (Principal Component Thermography) qui est basé sur l'analyse des composantes principales ((9)) (figure 4.6).

Robotic Eddy Current Thermography: Simulations and experiments

By Y. Mokhtari*, C Ibarra-Castanedo*, P. Servais** and X Maldague*

*Department of electrical and computer engineering, LAVAL University, Quebec city, Canada,
E-mail:*mohammed-yacine.mokhtari.1@ulaval.ca, xavier.maldague@gel.ulaval.ca*
** Level 3 Eddy Current and Infrared Testing, NDT Pro, Libramont, Belgium, Email: pierreservais@skynet.be

Acknowledgment

This research was supported by both governments of Wallonia/Brussels and Quebec, and by the Natural Sciences and Engineering Research Council of Canada (NSERC). We are also thankful to the Wallonie Aerotraining Network (WAN) for the provided expertise. We also thank Visioo-Image Ltd. for the technical help.

Abstract

Eddy current thermography (ECT) is an active thermography method. The inductive excitation generates Eddy currents in an electrically-conductive specimen. In presence of defects, the eddy current flow is affected by these discontinuities leading to changes in the temperature distribution in the specimen around the defects. These changes are observed by an infrared camera. In this paper, we present a robotic application of the method. Simulations are performed using COMSOL® Multiphysics by varying different parameters. Experiment is realised on an aluminum plate with cracks of different sizes created artificially in our laboratory. The resulting images are reconstructed with a dedicated algorithm.

Keywords: Eddy current thermography, nondestructive testing (NDT), Robotic NDT, 3D FEM.

1. Introduction

Over the last decades, thermographic Nondestructive testing (NDT) has been largely used in the aerospace industry. One of the main advantages of the technique is to inspect a relatively large area in a short time. Thermographic NDT can be divided in two categories: passive and active. Passive thermography doesn't need an external heat source and is used to test specimen that are naturally at different temperature than the ambient. Active thermography uses an external heat source to excite thermally the inspected material and observe changes in the temperature distribution.

Eddy current thermography (ECT) is an active thermography method. The inductive excitation generates, thanks to the electromagnetic force (Lenz-Faraday's Law), a circular current (Eddy current) [2], [4] in an electrically-conductive specimen that is inspected [1]. This current heats the specimen due to the resistance of the specimen (Joules losses). The presence of a discontinuity (a defect) then affects the temperature distribution in the specimen because of the perturbation of the current flow in the material. These changes are finally captured by an infrared camera. One of the most important parameter to take in account in Eddy current testing is the Skin Depth. It represents the maximum depth at which the current will "penetrate" the specimen. The Skin Depth depends on the frequency of excitation, the magnetic permeability, and the resistivity of the material [1], [2], [4].

Improvements in IR cameras have led to several researches in Eddy current thermography topic. In [1], inspection is deployed with an X-Y table. Simulations have been done on different specimens. It was shown that 3D simulations give better visualizations of the defects. Results have shown the capability of the method and a crack detection limit has been established. However, the resulting images were not processed. Also, the inspection could not proceed on complex shaped specimens (Curvatures).

In this work, Eddy current thermography is performed using a 6 degree of freedom (Dof) robotic arm. Simulations are achieved with COMSOL® Multiphysics. An aluminum plate with defects (line slots modelling cracks) with different size is modeled in software. In the experiments, an aluminum plate with defects (line slots) created artificially in our laboratory is inspected. The inspection is achieved with a 6 axis robotic arm. Resulting image is reconstructed using an algorithm developed in [6].

2. Simulation with COMSOL® Multiphysics

COMSOL® Multiphysics is finite element modeling software for numerical simulations enabling to model physical principles. To obtain a solution for Eddy current thermography, it is necessary to solve the magnetic propagation simultaneously with the heat transfer equations. Equations for the simulation model are given as follows [3]:

$$\rho C_p \frac{\partial T}{\partial t} - \nabla . k \nabla T = Q$$

Where $\rho(kg/m^3)$ is the density, $C_p(J/K)$ is the specific heat, $k(W/(m.K))$ is the thermal conductivity, and Q is the inductive heating.

$$Q = \frac{1}{\sigma}|J_s|^2 = \frac{1}{\sigma}|\sigma E|^2$$

with E, the electric field intensity vector, J_s the current density, and $\sigma(S.m^{-1})$ the electrical conductivity which is temperature dependent as it is shown in the following equation:

$$\sigma = \frac{\sigma}{1 + \alpha(T - T_0)}$$

With σ_0 is the conductivity at the reference temperature T_0, and $\alpha(\Omega.m)$ is the coefficient of resistivity.

Simulations are done in 3D since this gives better visualizations of defects [1]. Simulations are achieved on an aluminium plate with artificial defects created in our laboratory (line slots modeling cracks). The following parameters were varied: defects size (3 defects of size respectively: width = depth = 0.2mm; width = depth = 0.5; all defects have a length of 50mm (specimen's width)), frequency of excitation, and position of the coil (parameters are discussed below). Other parameters will be studied in future work to optimize results such as the number of turns for the coil and current circulating in it, lateral velocity and lift-off over the specimen. The following table shows the main simulations parameters:

Table 1: Simulations parameters

Parameters	Values	Parameters	Values
Current	15A	Distance between the coil and the plate (lift-off)	3mm
Number of turns for the coil	10	Time of heating	1s
Radius of the wire of the coil	1mm	Material of the coil	Copper
Radius of the coil	3mm	Material of the specimen	Aluminum

2.1. Simulations results

2.1.1 f = 100 KHz (excitation frequency), T = 1s (time of heating), D =3mm(lift-off)

The following figure shows simulations results with the previous parameters:

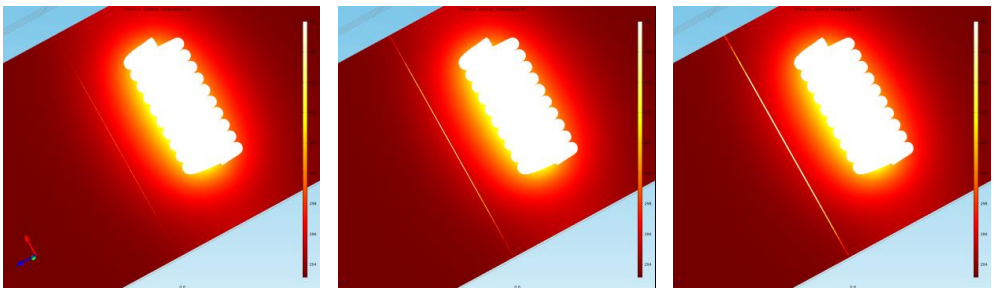

Fig. 1. *Simulations Results with f=100 KHz and T=1s (heating time): left (defect w (width) =0.2mm, d (depth) =0.2mm), Middle (defect w=0.5mm, d=0.5mm), right (defect w=1mm, d=1mm).*

2.1.2 f = 200 KHz (excitation frequency), T = 1s (time of heating), D =3mm(lift-off)

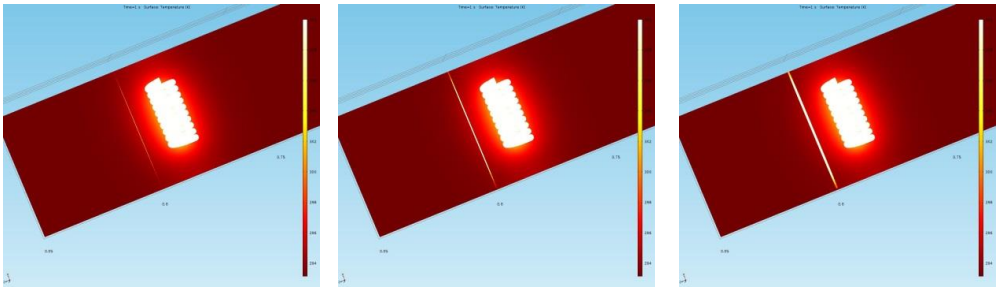

Fig. 2. *Simulations Results with f=200 KHz and T=1s (heating time): left (defect w (width) =0.2mm, d (depth) =0.2mm), Middle (defect w=0.5mm, d=0.5mm), right (defect w=1mm, d=1mm).*

From the figure, defects are very well detected, even the smallest one (0.2mm).

2.1.3 f = 200 KHz (excitation frequency), T = 1s (time of heating), D =7mm(lift-off)

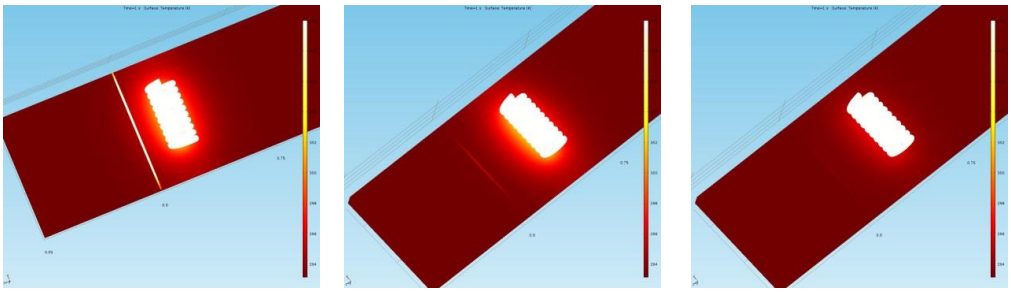

Fig. 3. *Simulations Results with f=200 KHz, defect w=1mm, d=1mm, and T=1s (heating time): left (coil position P= 0.5cm far from the defect, lift-off = 3mm), Middle (P = 2.5cm,lift-off=3mm), right (P =2.5cm,lift-off =7mm).*

Based on results obtained, we can see in figure 1, the three defects are clearly detected. Better results are obtained when using the frequency of excitation $f = 200KHz$ (figure 2) which is the frequency used when performing experimental Eddy current inspection of an aluminum alloy specimen in the laboratory. In the last simulation, the position of the coil is varied (lift-off and horizontal distance from the defect). From the results, it is observed that when the lift-off or the horizontal distance of the coil from the defect is relatively large, the magnetic field around the defect is less important. This leads to a decrease in Eddy current's amplitude around the defect and the heating is not as important (figure 3 middle and right) as if the coil is close to the defect (figure 3 left). Consequently, in experiments a frequency of $f = 200KHz$ and a lift-off of $3mm$ will be used.

3. Experimental results

3.1 Experimental setup

The experiment is performed on an aluminum plate (aluminum alloy 7075) with two defects created artificially in our laboratory (line slots modelling cracks), experiment parameters as in Table 1. The current in the coil is $I = 10A$. Other coil parameters (material, number of turns…etc.) are detailed in table 1. Defects sizes are, respectively, width = 0.5, 1mm, depth = 0.5, 1mm, and length = 70 mm (width of the specimen). Eddy current thermography is deployed with 6 axis robot FANUC LrMate 200iD/7L (figure 4). The whole specimen is then scanned with the robot while being heated with the coil. The results are observed with an infrared camera FLIR A65. Pseudo-static matrix reconstruction [6] is performed on the resulting images to have an image of the plate with all defects visible on it. Principal component thermography (PCT) algorithm [7] is applied to the results of the reconstruction (figure 8).

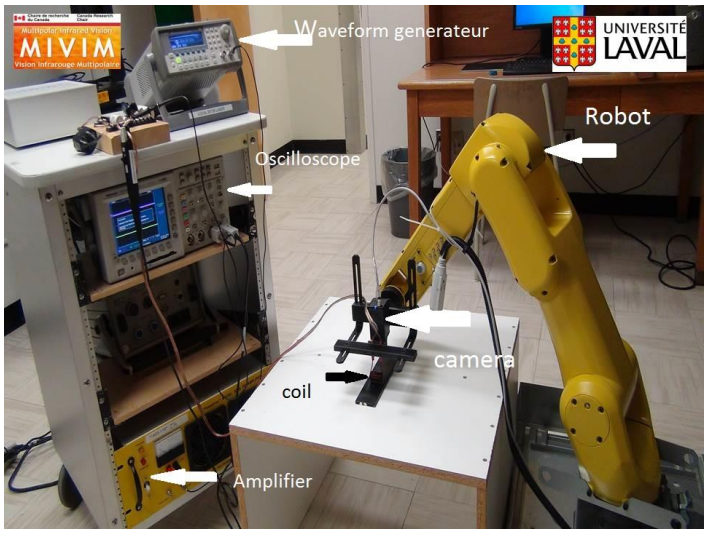

Fig. 4 *Experimental setup*

The eddy current equipment is:

- Coil (characteristics in table-1)
- Amplifier: Industrial Test Equipment “PowerTron” Model 500A RF
- Waveform generator: Agilent 33220A 200MHz
- An oscilloscope to monitor the excitation current (fig. 3): Tektronix TDS 3034B.

3.2 Results

The experiment is performed with a frequency of excitation $f = 200KHz$, the lift-off $D = 3mm$, and the speed of inspection is $V = 10mm/s$. Results are shown in the following figures:

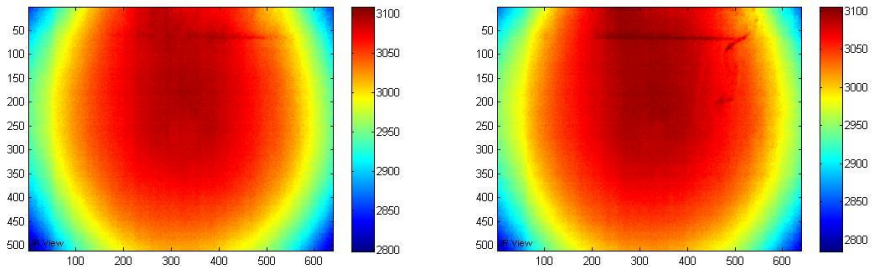

Fig. 5 *Experimental results on the aluminum plate: defect’s width and depth is 0.5mm (left), defect’s width and depth is 1mm (right). In both cases, defect length is 50mm (specimen width).*

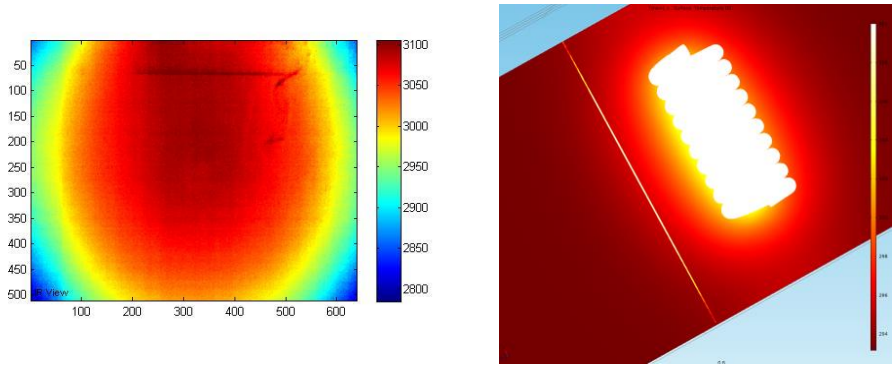

Fig. 6 *Experimental results on the aluminum plate for the defect of 1mm (left), orientation is 90^{o} with respect to simulations (right): line slot corresponding to defect is visible on the top.*

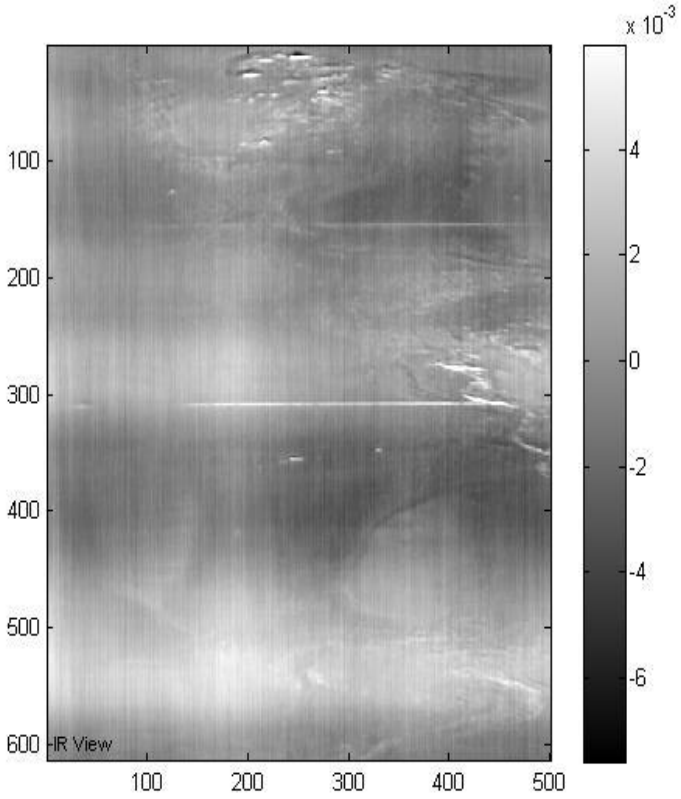

Fig. 7 *specimen reconstructed with Pseudo – static reconstruction: Both 0.5mm (top) and 1mm (bottom) defects are visible.*

From the experiment results, Defects of sizes $width = 0.5mm, depth = 0.5mm$ and $width = 1mm$ and $depth = 1mm$ are well detected (fig.5). Simulations results and the experiments match (fig.6). The time of inspection is about $20\ seconds$ for a $20cms$ length specimen, which is correct and will be improved in future works. From the result images of the specimen line scan, the latter was reconstructed with Pseudo-static matrix reconstruction [6] and a PCT algorithm [7] is applied to enhance the result contrast. Reconstruction results are shown in figure 6. The aluminium plate is well reconstructed and the resulting image represents the aluminium plate very well with the two defects clearly seen at the right positions. The bright spots (top and middle right of the figure) seen in the resulting image represent the painting non uniformity. The specimen has been painted in black to solve the low emissivity problem. Other bright spots (under the middle defect) are due to scratches in the paint. The defect's length is the width of the part ($50mm$). In the figure, the bright lines representing the defects do not go till the plate borders. The reason is that the coil is smaller than the specimen width. The heating is less important in specimen's edges which are "far" from the coil. The solution is to do another line scan of the specimen's part that has not been heated.

4. Conclusion

In this work, we presented a Robotic application of Eddy current thermography. Simulations were performed in order to determine best parameters for the experiment. Experiments were done on an aluminum plate with defects created artificially in our laboratory (line slots modelling cracks). The scanning of the part was achieved with a 6 axis robotic arm Fanuc LrMate 200iD/7L. Defects were very well detected. A reconstructed image of the specimen with the detected defects was obtained with Pseudo-static matrix reconstruction.

In future works, more complex shape specimens will be inspected and algorithms will be developed for this type of inspections. Also, we want to test of the scanning speed. Experiments will be done on specimens from the industry with real cracks.

REFERENCES

[1] P Tran-Gia, X Maldague, and L Birglen. "Crack detection limits in Eddy current thermography". The American Society for Non-destructive testing Research Symposium, (22), 2013.

[2] X Maldague. John Wiley." Theory and practice of infrared technology for non-destructive testing", 2001.

[3] I.Z Abidin, M Z Umar, M Y Yusof, and M. N Salleh. "Advantages and Applications of Eddy Current Thermography Testing for Comprehensive and Reliable Defect Assessment", 18th World Conference on Non-destructive Testing, 16-20 April, Durban, South Africa,

[4] P J Shull. "Non-destructive evaluation: theory, techniques, and applications", CRC press, 2002.

[5] H Fernandes, C Ibarra-Castanedo, H Zhang, and X Maldague. "Thermographic NDE of CFRP after tensile testing", Journal of NDE, 2015.

[6] C Ibarra-Castanedo, P Servais, A Ziadi, M Klein and X Maldague. "RITA – Robotized inspection by thermography and Advanced processing for the inspection of aeronautical components ", QIRT, 2014.

[7] N Rajic." Principal component thermography for flaw contrast enhancement and flaw depth characterization in composite structures", Compos. Struct., 58:521-528, 2002.

Chapitre 5

Thermographie linesan robotisée, une nouvelle façon de produire une carte CND de structure aérospatiale complexe

(Publié à la conférence Canadian Institute of Nondestructive Evaluation (CINDE) , 2017)

5.1 Résumé

L'objectif de ce travail est d'effectuer l'inspection linescan de la thermographie par courants de Foucault (LST) et explorer les capacités de la méthode ainsi que l'optimisation des paramètres d'inspection (fréquence et vitesse d'inspection). Ces paramètres ont été variés et un signal-to-noise ratio (SNR) est calculé à chaque variation pour chaque défaut. Les paramètres avec le plus grand SNR sont choisis comme optimaux. Les images de la thermographie par courants de Foucault sont post-traité et une image du spécimen est reconstruite ((3)). Finalement, une comparaison avec la méthode chauffage par lampe Halogène (IRT) pour montrer l'efficacité de la méthode. Les deux méthodes sont comparées en termes de SNR. Ce travail a fait l'objet d'une publication dans la conférence the Canadian institute of Non-Destructive Evaluation 2017 (CINDE).

5.2 Abstract

The objective of this research is to perform a robotic eddy current line scan thermography (LST) and investigate its capabilities and to optimize scanning parameters (frequency and scanning speed). These parameters were varied and the signal-to-noise ratio (SNR) was cal-

culated for each defect. Parameters are chosen for the highest SNR. Images of eddy current thermography were post processed and an image of the specimen was reconstructed based on [3]. Finally, a comparison is made with IRT to show the capability of the method. The two methods will be compared by the SNR.

5.3 Montage experimental

Le montage est montré par la figure 5.1. Il consiste en un robot à 6 axes de type FANUC LrMate 200iD/7L, un système de thermographie par courants de Foucault avec une bobine en cuivre (voir 3.2.4), et une caméra infrarouge FLIR A35 montées sur l'effecteur du robot. La pièce inspectée est une plaque en acier (stainless steel) académique avec des trous à fond

FIGURE 5.1 – montage experimental

plat (flat bottom holes) de deux diamètres $D_1 = 20mm$ et $D_2 = 10mm$ et de profondeur variables $z = 1mm$ à $4mm$ pour simuler des défauts de différentes tailles et profondeurs. La plaque comprend également une rainure (slot) de dimensions ($100mmx10mm, z = 1mm$) comme illustré dans la figure 5.2. L'expérience consiste à faire varier la vitesse d'inspection et la fréquence d'excitation (fréquence des courants de Foucault). La vitesse de scan est variée de $V = 25mm/s, 50mm/s$ et $75mm/s$. Trois fréquences d'excitations sont utilisées $f = 72KHz, 90KHz$ et $100KHz$.

Les résultats sont post-traités en utilisant l'algorithme PCT ((9)). Limage de la pièce est ensuite reconstruite avec et sans le post traitement. Le signal-to-noise ratio est ensuite calculé pour chaque paramètre et pour les résultats avec et sans traitement en utilisant la formule suivante ((3)) :

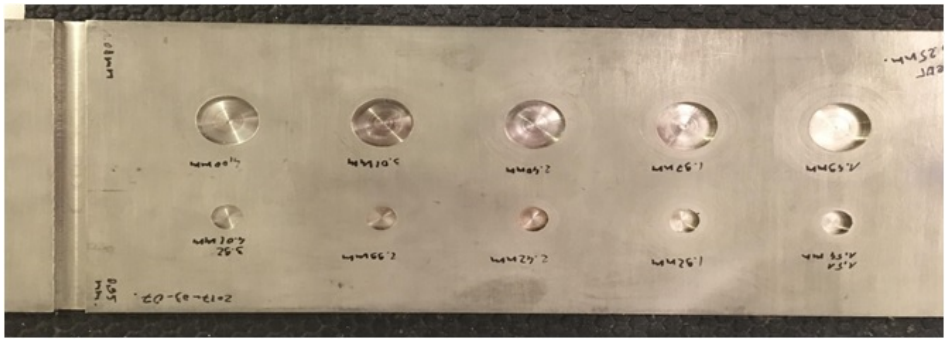

FIGURE 5.2 – plaque en acier

$$SNR = 20log_{10}\left|\frac{S_d - S_{sa}}{\sigma_{sa}}\right|$$

Ou :
S_d : signal du défaut S_{sa} signal sans défaut(sound area) σ_{sa} lécart type de la sound area

5.4 Résultats

Les résultats de la linescan thermographie par courants de Foucault (LST) sont comparés aux résultats de la thermographie optique (par lampe halogène IRT) en linescan également. Cette dernière a été exécutée en utilisant la même d'inspection. Le SNR de chaque défaut de D1 à D13 est calculé pour les deux méthodes et est présenté à la figure suivante :

Les valeurs soulignées en rouge représentent le SNR maximum avec traitement PCT tandis que les valeurs soulignées en jaunes sont les maximum SNR de chaque défaut sans post-traitement (PCT).
Il est intéressant de noter que pour la majorité des défauts, la valeur maximum du SNR pour les courants de Foucault est obtenu pour la fréquence **f=92KHz** et la vitesse d'inspection **V= 25mm/s**. Ceci implique que ces les paramètres sont optimaux pour l'inspection du spécimen en acier.
Il est également intéressant de constater que pour tous les défauts, le SNR de la linescan thermographie pour courant de Foucault est supérieur au SNR du linescan optique (IRT). Ce résultat démontre les capacités de la LST pour les pièces métalliques. La figure 5.4 démontre la différence de profils entre la LST et l'IRT. Le profil de la LST présente beaucoup moins de bruits.

V(mm	δ(mm)	d1	d1_PCT	d2	d2_PCT	d3	d3_PCT	d4	d4_PCT	d5	d5_PCT	d6	d6_PCT
25		28.124	30.5976	7.0917	15.3792	7.5564	23.4591	10.0304	18.8804	20.7054	28.1638	23.3619	32.7058
50	4.022	25.6621	31.5226	3.7512	24.8277	5.5173	19.355	2.4438	11.8985	16.0532	16.8331	22.2867	26.5503
75		17.006	26.5443	2.1687	18.3703	4.3487	17.7072	1.1713	12.4303	8.6614	14.9033	23.4987	31.2628
25		28.3156	36.4293	N.D	17.5841	1.605	27.2204	18.3881	28.4721	17.901	34.9816	21.3853	38.8303
50	3.598	22.0754	34.3753	N.D	21.7602	1.5133	21.89	7.2509	26.3489	15.5073	29.538	18.3414	30.5159
75		20.1582	33.916	N.D	19.4541	4.8306	21.1429	N.D	16.689	8.3015	26.3837	18.5532	32.5976
25		27.824	24.1396	7.3443	16.9773	11.0377	18.1829	13.9971	17.8729	22.4469	21.5312	27.4617	31.3956
50	3.112	22.2885	23.3765	N.D	21.0808	1.1811	7.304	9.6114	17.2183	18.958	21.1131	23.9152	25.2563
75		14.3975	26.6589	N.D	15.4707	N.D	16.6951	N.D	11.8519	11.4043	24.0093	19.8863	31.5758
25		18.2881	21.5769	6.646	5.9781	11.3374	N.D	16.3252	12.2354	17.22	13.2772	22.6974	18.6129
50		24.7603	24.7076	6.9717	10.4489	7.9213	3.0842	12.6809	19.3456	19.0959	19.8549	23.5308	21.2836
75		21.1426	11.5048	4.9338	6.6455	1.6764	6.9986	14.0829	14.2081	20.908	16.5704	20.4007	15.1845

N.D : not detected

F (Khz)	V(mm/s)	d7	d7_PCT	d8	d8_PCT	d9	d9_PCT	d10	d10_PCT	d11	d11_PCT	d12	d12_PCT	d13	d13_PCT
72	25	26.9121	34.4129	2.6602	4.7245	3.22	6.6974	12.3523	8.7235	14.113	17.5058	19.9397	23.0308	21.7672	23.1085
	50	23.1322	33.7109	4.8337	8.9765	4.3494	9.7712	4.1574	4.8066	17.686	23.5082	20.4321	26.5897	22.4711	27.6573
	75	18.9728	34.553	4.8836	11.4928	4.2823	20.846	2.0689	16.8595	7.7234	23.3596	17.0624	25.3295	13.8048	29.2096
92	25	24.0203	30.6188	3.1494	N.D	N.D	21.364	8.5243	11.7751	10.048	20.0756	14.8864	27.9301	18.7951	29.0904
	50	21.3215	33.3853	N.D	14.5992	1.7007	21.142	3.0042	15.6223	2.7287	17.9956	14.4084	33.0383	17.5444	27.0743
	75	18.0742	35.4257	0.4974	4.5883	1.0214	13.927	N.D	7.7717	9.5187	17.3191	18.514	28.7291	17.5149	28.2109
100	25	26.4551	33.6002	N.D	8.181	N.D	21.277	1.3865	N.D	9.3557	15.2175	17.5161	18.85	18.0679	25.4142
	50	23.6736	34.9646	2.1296	6.297	N.D	16.265	N.D	9.0963	12.07	16.7093	18.3475	20.9287	19.5536	26.5398
	75	21.4901	34.6985	N.D	3.4573	N.D	17.718	N.D	14.3964	N.D	9.6367	17.356	28.0037	15.392	25.933
IRT Linescan	25	24.5262	14.1898	N.D	N.D	N.D	6.1163	0.2434	N.D	N.D	N.D	12.2544	0.093	N.D	N.D
	50	24.0099	16.9596	N.D	N.D	N.D	7.9107	N.D	N.D	6.0181	14.4618	16.3371	14.8562	0.6345	2.3475
	75	23.1197	21.8776	N.D	2.2522	N.D	N.D	N.D	0.7566	6.1882	4.0989	14.894	1.3505	8.8751	11.6404

N.D : not detected

FIGURE 5.3 – SNR des défauts pour LST et IRT

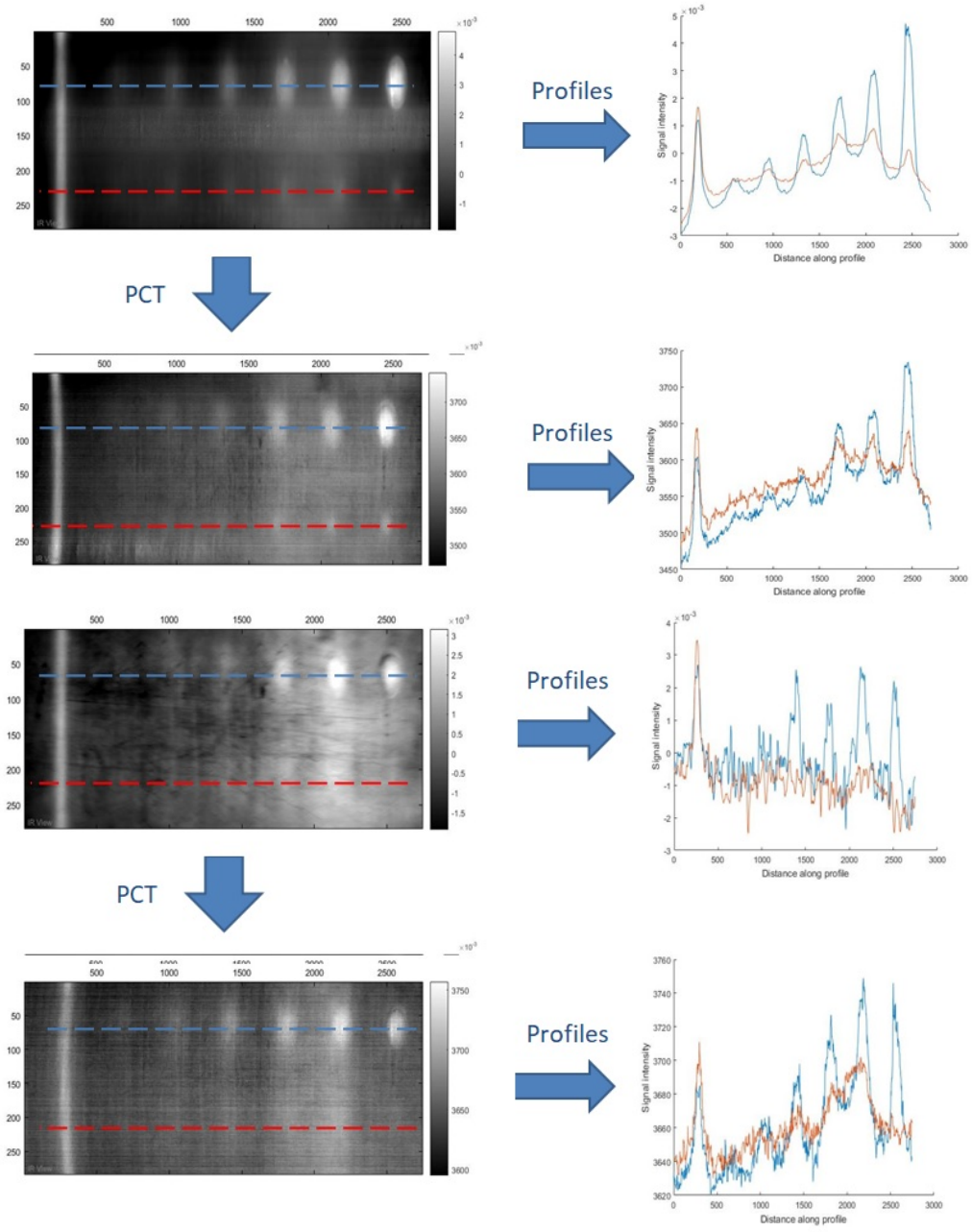

FIGURE 5.4 – Comparaison Courants de Foucault (haut) et chauffage optique (bas)

Chapitre 6

Comparative study of linescan and flynig line Active IR thermography operated with a 6 axes robot

(publié à la conférence Quantitative Infrared thermography (QIRT), 2018)

6.1 Résumé

Dans ce travail, deux méthodes de contrôle non destructifs avec la thermogrpahie active sont montées sur un robot à 6 axes. Ces dernières sont présentées et étudiées. L'excitation thermique et l'acquisition des données sont achevées de manière dynamique pour des plaques de fibre de carbonnes (CFRP) planaires, concaves, et convexes afin d'augmenter la compléxité de l'inspection. Une procédure automatique est proposée pour recontruire la séquence des images thermiques obtenue du linescan et du Flying line. La détection des défauts se fait par traitement d'images. Les résultats obtenus sont analysés et d'autres perspectives sont proposées. Cette recherche a été soumise pour la conférence QIRT 2018.

6.2 Abstract

In this paper, two Non Destructive Testing approaches by active infrared thermography mounted on a 6-axis robot are presented and studied. Data acquisition and thermal excitation is carried out dynamically over various CFRP specimens with increasing geometry complexity, form planar, convex and concave shapes. An automated procedure is proposed to reconstruct thermal image sequences issued from the two scanning procedure studied, respectively the Line Scan and Flying Line procedures. Defective area detection is performed by image processing

and an inverse technique based on thermal quadrupole method is used to map the depth of flaws. Results obtained are discussed and perspectives are addressed.

Comparative study of Line Scan and Flying Line Active IR Thermography operated with a 6-axis robot

by Y. Mokhtari*, L. Gavérina**,***, C. Ibarra-Castanedo*,****, M. Klein****, P. Servais*****, J. Dumoulin**,***, X. Maldague*

** Electrical and Computer Engineering Dpt, LVSN-MIVIM, Laval University, Av. De la Médecine, Québec, Canada.*
*** IFSTTAR, COSYS-SII, Allée des Ponts et Chaussées, F-44344, Bouguenais, France.*
**** Inria, I4S Team, Campus de Beaulieu, F-35042 Rennes, France*
***** Visiooimage IRT Research Inc., 2560 rue Lapointe, Québec (QC) G1W 1A8, Canada*
****** NDT Pro-WAN, Libramont-Gosselies, Belgium*

Contact authors: mohammed-yacine.mokhtari.1@ulaval.ca and ludovic.gaverina@ifsttar.fr

Abstract

In this paper, two Non Destructive Testing approaches by active infrared thermography mounted on a 6-axis robot are presented and studied. Data acquisition and thermal excitation is carried out dynamically over various CFRP specimens with increasing geometry complexity, form planar, convex and concave shapes. An automated procedure is proposed to reconstruct thermal image sequences issued from the two scanning procedure studied, respectively the Line Scan and Flying Line procedures. Defective area detection is performed by image processing and an inverse technique based on thermal quadrupole method is used to map the depth of flaws. Results obtained are discussed and perspectives are addressed.

1. Introduction

The inspection of complex-shaped specimen is complicated using the conventional thermal methods, such as flash or lock-in techniques. Such investigation represents a serious challenge in particular for the aeronautic industry.

Twenty years ago, Krapez et al. [1] proposed the “flying spot technique” based on a constant displacement of the laser spot to detect cracks in steel. Then, the Pulsed Flying Spot (P.F.S) [2] was developed to obtain in-plane thermal diffusivity fields on heterogeneous and anisotropic materials. Though the laser spot is a very interesting approach due to its known analytical solution, it has a lower scanning rate than the line scan method. For this reason, the flying line method has been proposed instead to detect cracks [3], [4] in metals as well as disbonding in composite materials [5], [6].

Recently, the MIVIM laboratory at Laval University has developed and improved the Robotized Inspection by Thermography and Advanced processing for the inspection of aeronautical components (RITA): it is a robotic arm that allows inspection of complex-shaped specimens. The goal of the present study is the thermogram reconstruction whatever the configuration of the RITA set-up, and in a second stage to calculate the depth map of defects in composite material with various shapes.

In this paper, we first introduce the test bench with the 6-Axis robot and describe the planar specimen used. Dedicated post-processing methods studied and develop to reconstruct thermal sequence acquired in line scan and flying line modes are presented and results shown. Then damage localization characterization approaches are introduced and results analysis is discussed. Finally, conclusion and perspectives are addressed.

2. Experimental set-up and procedures

2.1. Active IR test bench

The inspection of the object surface is carried out by active infrared thermography technique. The heating of specimen is done in linear configuration and performed for two data acquisition modes: Line Scan and Flying Line. In line scan, both the heating source and the IR camera move synchronously over the surface of the specimen by using the robotic arm (figure 1.a.). In flying line, only the heating source mounted on the robotic arm moves while data acquisition is realized with the IR camera fixed on a tripod in front of the scene (figure 2.a.). figure 1.b and figure 2.b show IR images of the scene at a fixed time for the two configurations.

Two IR cameras were used during experiments. A FLIR SC655 (640*480 pixels, NETD 30mK, 50 FPS, pitch 17 µm, spectral band 7.5 – 13 µm) and a FLIR A65 (640*512 pixels, NETD 50mK, 30 FPS, pitch 17 µm, spectral band 7.5 - 13 µm). The linear heating source is an optical one mounted horizontally on the robotic arm. The robotic arm is the RITA system developed by the MIVIM Laboratory at Laval University in collaboration with Visiooimage Inc..

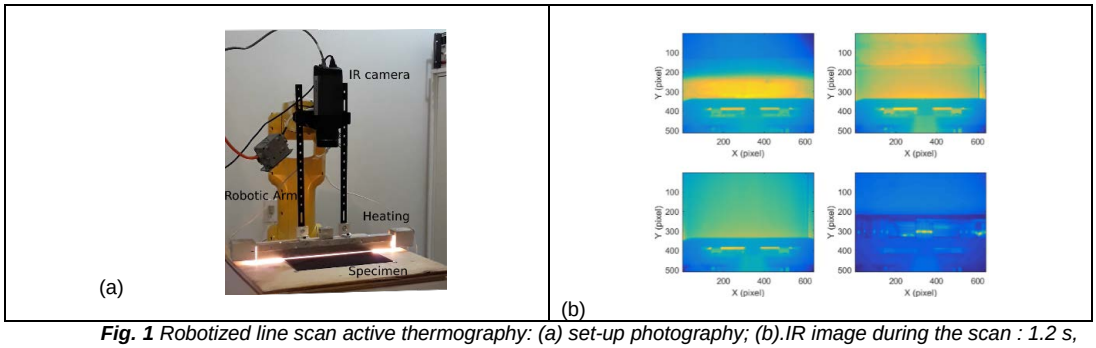

Fig. 1 *Robotized line scan active thermography: (a) set-up photography; (b).IR image during the scan : 1.2 s, 4s, 8s, 12 s.*

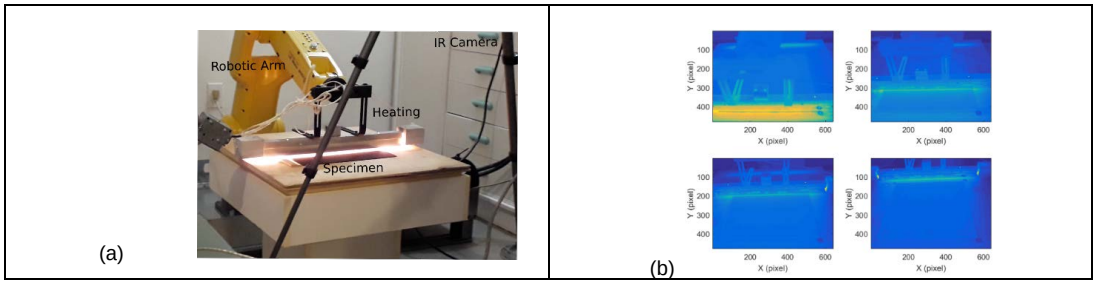

Fig. 2 *Robotized flying line active thermography: (a) set-up photography; (b).IR image during the scan : 1.2 s, 4s, 8s, 12 s.*

2.2. Experimental specimen

Experiments were carried out on academic CFRP specimens [7], which incorporate twenty-five square Teflon inserts of different sizes at different locations, as illustrated in Figure 3.

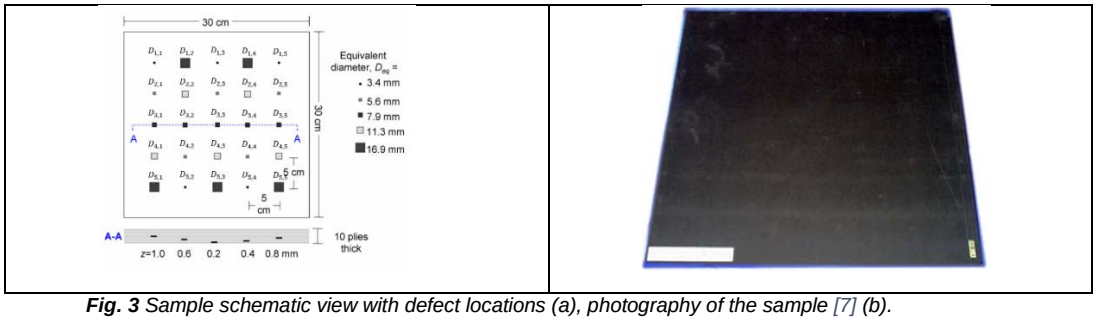

Fig. 3 *Sample schematic view with defect locations (a), photography of the sample [7] (b).*

The total dimensions of the square CFRP sample, presented hereafter, are 300 mm *300*mm*2 mm. The thermal properties of the material are the following:
Thermal conductivity $\lambda = 0.8$ W.m^{-1}.K^{-1}, volumetric heat capacity $\rho C_p = 1.92*10^{-6}$ J.m^{-3}.K^{-1} and thermal diffusivity $\alpha = 4.2*10^{-7}$ m^2.s^{-1}.

3. Reconstruction

3.1. Line Scan

In the literature [8], many parameters must be known to reconstruct the thermographic matrix I_r from line scan method such as, (i), spatiotemporal resolution (size of FPA matrix), (ii), field of view and (iii), acquisition rate, … .

In this case, it is possible to reconstruct the matrix I_r without those parameters. This algorithm is based on the tracking of each line pixel independently for each frame of the matrix $I(x,y,t)$. The pixel line $p(x_n,y_n,t_n)$ of the matrix $I(x,y,t)$ is shifted on the initial $p(x_0,y_0,t_0)$ by $y_0+N\cdot d_y$ as shown in the figure 4.a. After determining this shift from the slope of a straight line of the maximum of each pixel line of the matrix $I(y,t)$ (figure 5.a), each pixel line reconstructed temporally is rearranged in the new matrix $I_r(x,t,y')$ where y' is equal to $N\cdot d_y$ as shown in the figure 4.b.

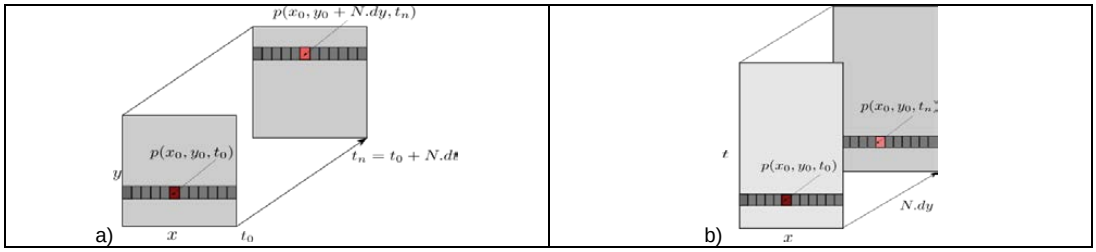

Fig. 4. *Schematic reconstructed thermogram (a), raw thermogram (b). reconstructed thermogram*

An example of thermographic image reconstructed is shown in figure 5.b from the dynamic matrix.

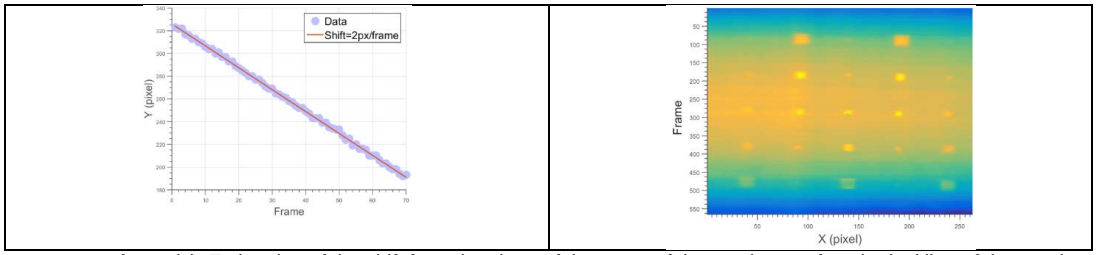

Fig. 5. *(a), Estimation of the shift from the slope of the curve of the maximum of each pixel line of the matrix $I(y,t)$, (b). reconstructed thermogram.*

The presence of the defects is clearly seen, thus algorithm can be used to reconstruct the raw thermogram. It can be also observed background effect due to non-uniform heating, which reduces defective area thermal contrast.

3.2. Flying line

In the flying line configuration, the algorithm proposed to reconstruct the matrix I_r is faster and simpler than the previous method. In this case, the camera frame rate is not synchronized with the displacement of the robotic arm. As the previous algorithm each line pixel is heating independently for each frame of the matrix $I(x,y,t)$ but the pixel line corresponding to the $p(x_0,y_0,t_0)$ is the pixel line $p(x_0,y_0,t_n)$ as show in figure 6.a and b. Therefore, the method to reconstruct the new infrared sequence $I_r(x,y,t)$ is based on the tracking of the gradient for each frame. In this new infrared sequence $I_r(x,y,t)$, there is a time-offset between each pixel line from each frame as show in figure 6.c. This time-offset is estimated for each pixel line by the detecting the barycentre at each frame as it is shown in the figure 6.d. The new thermal sequence obtained is similar to a the ones observed in a flash (*i.e.* short pulse) method [9].

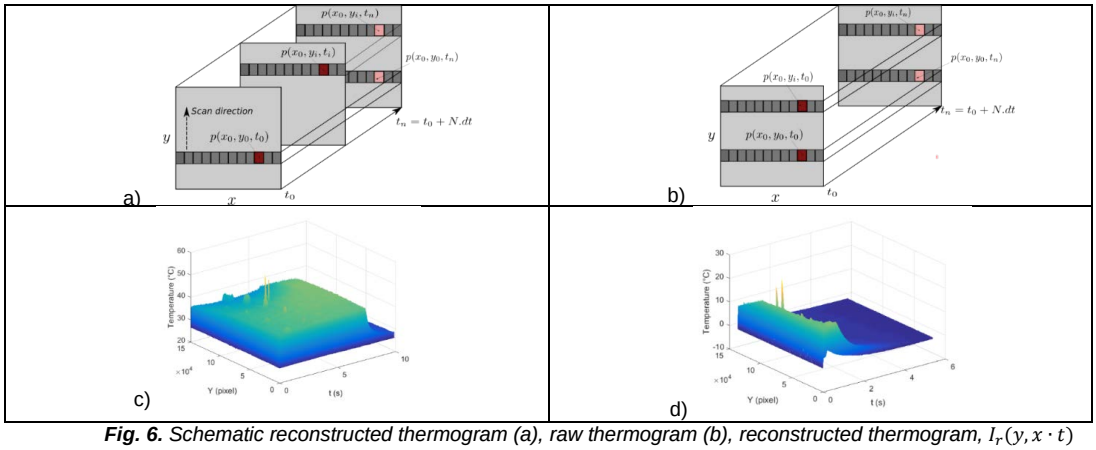

Fig. 6. *Schematic reconstructed thermogram (a), raw thermogram (b), reconstructed thermogram, $I_r(y, x \cdot t)$ represents themal profile : (c), shifted between each frame, (d); not shifted between each frame.*

An example of thermographic image reconstructed is shown in figure 7 from the dynamic matrix $I(x, y, t)$.

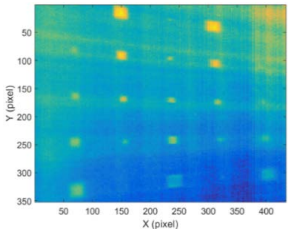

Fig. 7. *Averaged thermogram over several hundreds of reconstructed thermograms corresponding to flying line scan active thermography*

The presence of the defects is clearly seen, thus algorithm can be used to reconstruct the raw thermogram. One can also observed deformation in the reconstructed thermal image probably due to the non-regular initial field of view of the camera. This can be a problem for the future estimation due to the non-constant spatial sampling. Anyway, several methods may be used to attenuate effects of such problem [10].

4. Defect localization and characterization

4.1. Thermal signal filtering

For line scan mode, figure 8.b shows the thermal profiles for defective areas at the same depth ($D_{1,2}$, $D_{1,4}$,) and sound area ($S_{1,2}$, $S_{1,4}$) obtained from line scan thermograms. It can be observed for these profiles a same thermal contrast between defect and sound areas, and the decay of these curves is similar to a static pulsed thermography [9].

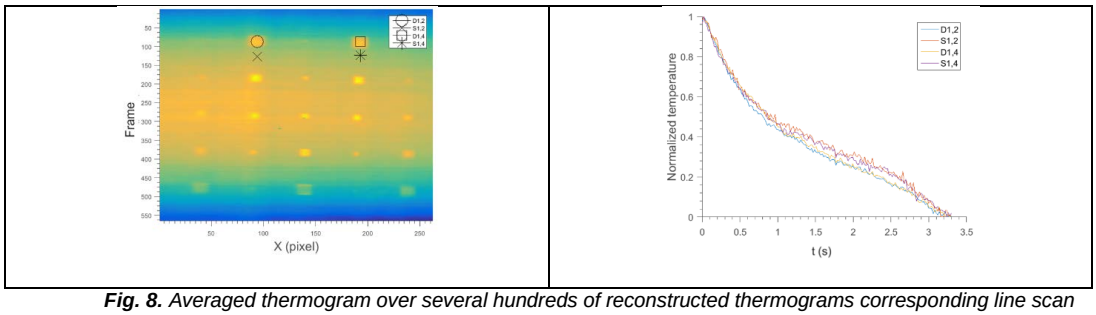

Fig. 8. *Averaged thermogram over several hundreds of reconstructed thermograms corresponding line scan active thermography: (a) raw reconstructed thermography; (b) thermal profiles.*

In flying line mode, figure 9.a shows the thermal profiles for defect areas at the same depth ($D_{1,4}$, $D_{2,4}$, $D_{3,4}$, $D_{4,4}$) and figure 9.b shows thermal profiles for different depth ($D_{3,1}$, $D_{3,2}$, $D_{3,3}$, $D_{3,4}$). As can be seen from these profiles produce a positive thermal contrast with respect to the sound area and the decay is depending to the depth. These last thermal profiles shows that flying line experiment after reconstruction is similar to thermal profile from static flash method [9].

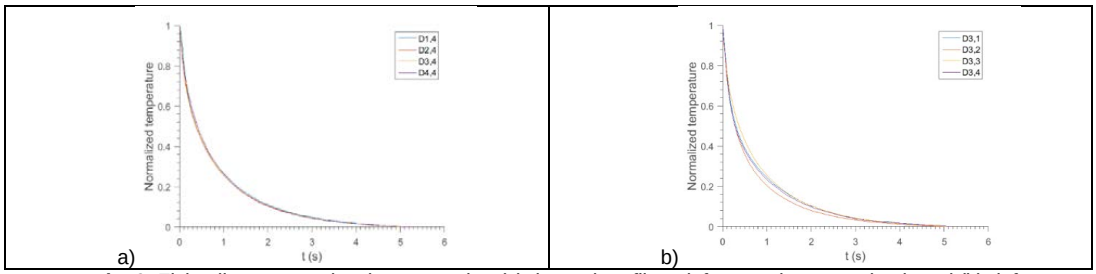

Fig. 9. *Flying line scan active thermography: (a) thermal profiles: defects at the same depth and (b) defects not the same depth.*

Some observations can be made on these results. The raw reconstructed thermograms in Figure 10.a and c presents some signs of non-uniform heating, which reduce the defect contrast. A correction stage may be added to the raw reconstructed thermogram to increase the defect contrast. For instance, here we use polynomial fitting to approximate thermal background and correct thermograms. However, some artefacts are still present in the raw reconstructed thermogram due to some discrete inhomogeneities inherent to the heating source, as it is show in Figures 10.b and 10 d.

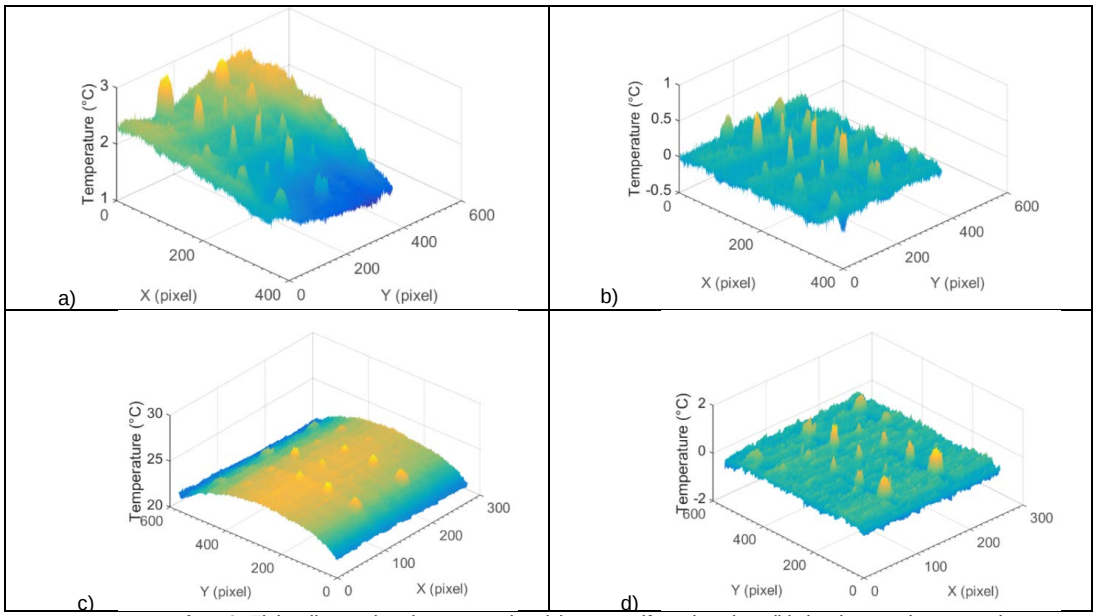

Fig. 10. *Flying line active thermography: (a), non-uniform heating, (b), background corrected. Line scan active thermography: (c), non-uniform heating, (d), background corrected.*

4.2. Defect localization by Singular Value Decomposition (S.V.D)

Since several years, Singular Value Decomposition (S.V.D) is applied in image processing and signal processing problems for data compression and noise reduction. In Non Destructive Testing and thermal analysis, SVD-based methods have been employed to defect detection [11]. In this part, the Singular Value Decomposition (S.V.D) is applied to the previous results from line scan and flying line.

For that, the thermogram matrix (3D) representing space and time has to be reorganized as a 2D matrix as follow:

$$T(X,t) = T(x,y,t) \qquad (1)$$

Applying S.V.D on a thermal field of 2D thermogram matrix is reported in equation 2:

$$T(X,t) = \sum_{k=1}^{\min(N_x,N_y,N_t)} \gamma_k U_k(X) V_k(t)^t \quad (2)$$

Where
$U_k(X)$ and $V_k(t)$ are orthogonal functions and γ_k are the singulars values in decreasing mode.

The columns of the matrix U represent the empirical orthogonal functions (EOF) that describe the spatial variations of data [12]. The first columns of the matrix U represent the most characteristic variability of the data. The figure 11 which represent the logarithm of singulars values from S.V.D apply to the matrix $T(X,t)$ as a function of singular values index show the first three singulars values is much greater than the others.

These columns of the matrix U has to be reorganized as a 2D matrix as follow:

$$EOF_k(x,y) = \sum_{k=1}^{k=3} U_k(X) \quad (3)$$

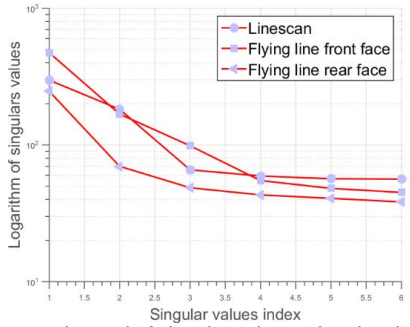

Fig. 11. *Diagonal of singular values related to the expression*

So the original data can be represented only with three EOF.

In figure 12, sound and faulty areas were localized by using EOF maps for line scan, flying line for front and rear face scan. This method can be used to localize the spatial position of defect.

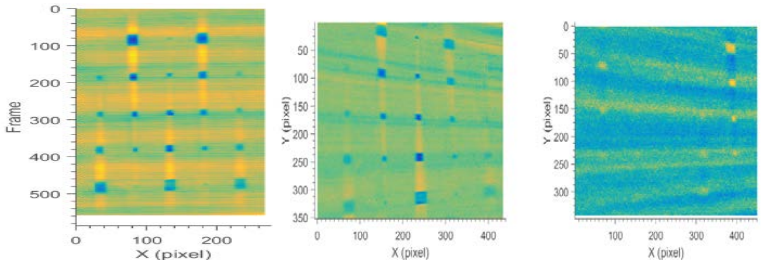

Fig. 12. *PCT results: EOF_2 line scan active thermography (left), EOF_1 front face of flying line scan active thermography (middle), EOF_1 front rear of flying line scan active thermography (right)*

4.3. Thermal contrast

The thermal contrast is a processing technique to enhance subsurface defect visibility and also a quantitative method to estimate defect depth and size [13-14]. This method require a priori information, such as, sound area and defective area localization. However, these informations are not always available but it is possible to apply the previous method (see section 3.1) to identify them. In this case, the sound area is not a uniform all over the specimen.
The absolute thermal contrast definition is reported below:

$$C_T(i,j,t) = T_d(i,j,t) - T_s(i,j,t) \quad (4)$$

where $T_d(i,j,t)$ defect area and $T_s(i,j,t)$ sound area at location *i,j*.

Results obtained by calculating absolute thermal contrast for both experiments (line scan and flying line) are presented in figures 13a and 14a. Amplitude differences in thermal contrast maps (i.e. profiles) are observed. Anyway, thermal contrast from line scan is more significant than the flying line because there is no initial field of view induced effect on reconstructed thermal images.

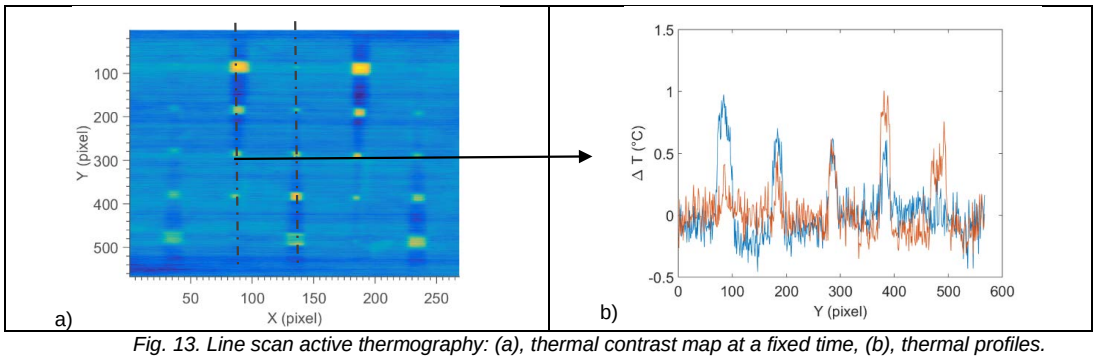

Fig. 13. Line scan active thermography: (a), thermal contrast map at a fixed time, (b), thermal profiles.

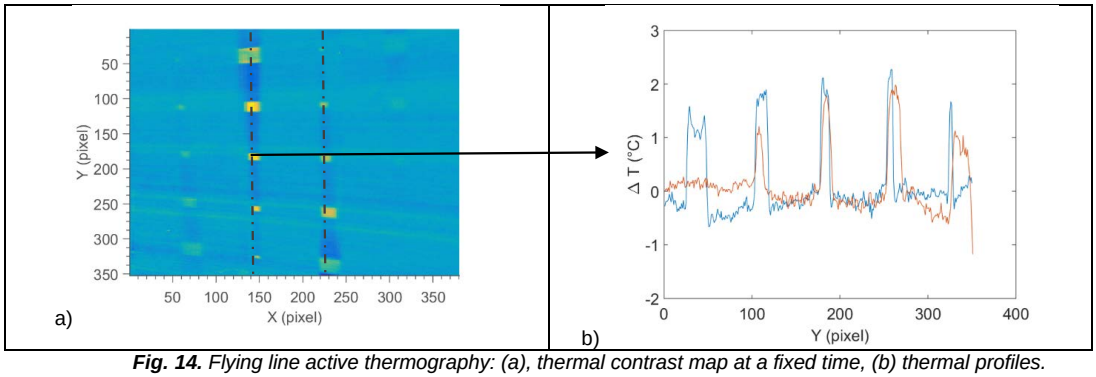

Fig. 14. *Flying line active thermography: (a), thermal contrast map at a fixed time, (b) thermal profiles.*

Figure 15 shows thermal signal as a function of time obtained from both scans: line scan figure 15 a. and flying line figure 15 b. These figures illustrate thermal contrast decay with defect depth. Furthermore, for the chosen scan speed maximum contrats may appear or not appear in the time interval of observation, depending also on defect depth.

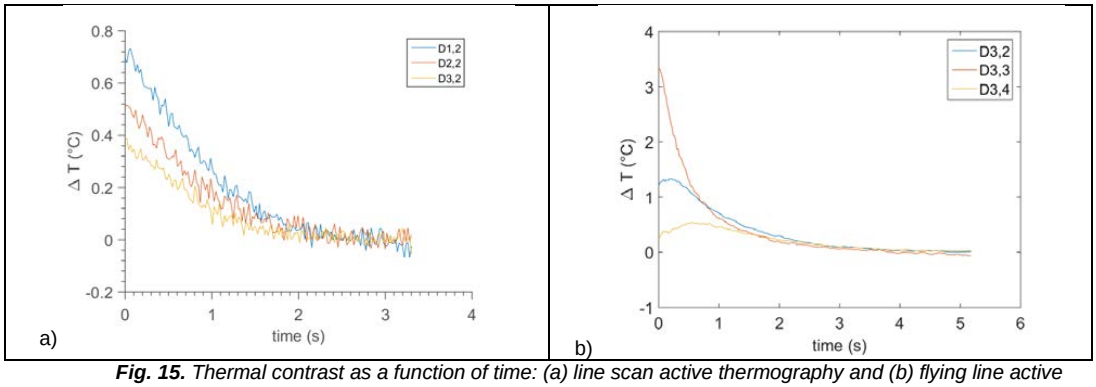

Fig. 15. *Thermal contrast as a function of time: (a) line scan active thermography and (b) flying line active thermography*

In such context using time of the appearance of the maximum thermal contrast for defect depth retrieval will require to act on the robot scan speed. A possible alternative is to use thermal inverse method to retrieve such information.

4.4. Thermal Inverse approach

4.4.1. Direct thermal model

In this section, we first apply the quadrupole method to calculate the surface temperature of multilayered CFRP, supposed to have homogeneous thermal properties, that is illuminated by uniform radiative source. Accordingly, in this simple configuration the one-dimensional approach can be used. The quadrupole formalism expresses, for each layer *i*, the upstream temperature flux vector in terms of downstream temperature flux vector in Laplace space.

Let us consider that the specimen is a parallelepiped with a thickness e (2 mm), a thermal conductivity k (0.8 W/mK), a volumetric mass density ρ (1600 kg/m^3), a heat capacity c_p (1200 J/Kg/K) and a thermal diffusivty (4.2*10^{-7} m/s). The specimen is submitted to heat exchange both on front h_1 and rear face h_2.

The specimen is not homogeneous due to delamination (defective areas), so we have considered two models such as: (i), sound area with one layer and (ii), defect area with two layers separated by the defect whose is modelled as follow:

(i) Quadrupole formalism for sound area

$$\begin{bmatrix}\theta_1\\ \varphi_1\end{bmatrix} = \begin{bmatrix}1 & 0\\ h_1 & 1\end{bmatrix}\begin{bmatrix}A_s & B_s\\ C_s & D_s\end{bmatrix}\begin{bmatrix}1 & 0\\ h_2 & 1\end{bmatrix}\begin{bmatrix}\theta_2\\ \varphi_2\end{bmatrix} \quad (4)$$

After algebraic manipulation, the Laplace temperature over front face for a sound area can be written as:

$$\theta_2 = \frac{\varphi_1(A+Bh_2)+\varphi_2(DA-BC)}{C+Dh_2+Ah_1+Bh_1h_2} \quad (5)$$

(ii) Quadrupole formalism for defective area

$$\begin{bmatrix}\theta_1\\ \varphi_1\end{bmatrix} = \begin{bmatrix}1 & 0\\ h_1 & 1\end{bmatrix}\begin{bmatrix}A_1 & B_1\\ C_1 & D_1\end{bmatrix}\begin{bmatrix}1 & R\\ 0 & 1\end{bmatrix}\begin{bmatrix}A_2 & B_2\\ C_2 & D_2\end{bmatrix}\begin{bmatrix}1 & 0\\ h_2 & 1\end{bmatrix}\begin{bmatrix}\theta_2\\ \varphi_2\end{bmatrix} \quad (6)$$

with:

$$A_i = D_i = \cosh\left(\sqrt{\frac{p}{a_i}}e_i\right);\ B_i = \frac{\sinh\left(\sqrt{\frac{p}{a_i}}e_i\right)}{\lambda_i\sqrt{\frac{p}{a_i}}};\ C_i = \lambda_i\sqrt{\frac{p}{a_i}}\sinh\left(\sqrt{\frac{p}{a_i}}e_i\right) \quad (7)$$

Where *p* is the Laplace variable and $R = \frac{e}{\lambda}$ the thermal resistance considered between two layers.

The main purpose is to be able to characterize the depth and the thermal resistance of defect. Based on the one-dimensional thermal model (Eq. (6)), an inverse problem is solved using the Levenberg-Marquardt algorithm, that is applied independently to each pixel of the 3D thermogram matrix.

As the first and second layer is an orthotropic material and as there is a priori knowledge on the thermophysical and thickness properties of the CFRP, the number of unknown parameter is reduced in the inverse model. The parameters estimated are then the thermal resistance *R* and the depth of defect, which is obtained from the thickness of two layers e_1 and e_2.

Furthermore, the energy deposed on the surface is estimated from the first model (Eq. (4)) using pixel without defect and considering a square wave form excitation as described in equation 8. The heat duration τ is related to the displacement velocity of the heating line during the experiments (figure 16. a). After having reconstructed the thermogram from the flying line scan, it is still not to possible to have the shape evolution related to the heat duration (figure 16. b). So, in that case, we have to consider τ that is equal to the displacement duration of the heating (*3s* in the shown results).

The Laplace expression of the heating source is:

$$\varphi_1 = \frac{Q}{p}(1 - e^{-\tau p}) \quad (8)$$

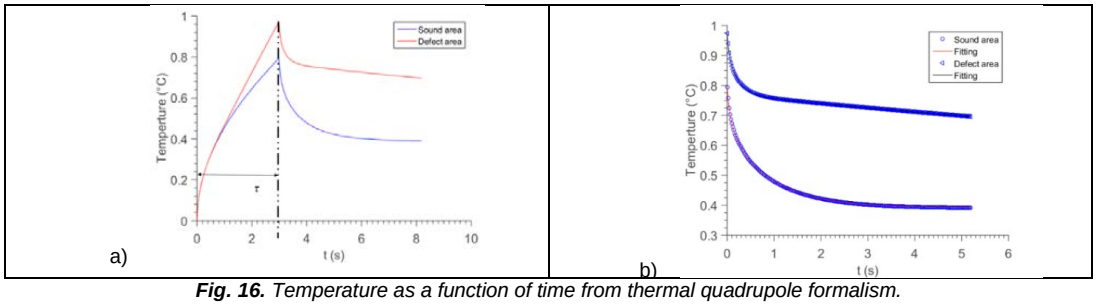

Fig. 16. *Temperature as a function of time from thermal quadrupole formalism.*

4.4.2. Depth estimation

In this part, the estimated parameter associated to front surface observation of CFRP plate are presented for flying line mode. The figure 17 show that the estimation procedure applied to reconstructed thermal infrared image sequence is able to characterize defect depth in CFRP material. However, the spatial distortion due to the field of view of the IR camera fixed on a tripod in front of the scene affect the depth estimation. In order to correct this problem, it could be possible to apply an algorithm to recover a non-projective view [10].

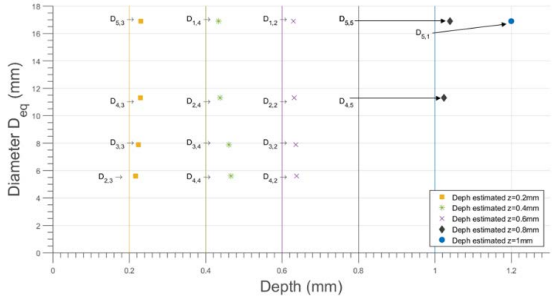

Fig. 17. *Diameter as function of the depth estimation (symbol) for each defect of CFRP specimen. The real depth is representing by a coloured straight line.*

Moreover, one will observed that for a given scan speed , depth estimation depends on the real depth and size of defect , but also on the validity of the 1D inverse model as suggested in [15] in their sensitivity analysis.

5. Conclusion and perspectives

In this paper, two kind of active infrared non destructive testing processes, mounted on a 6-axis robot, have been studied: line scan and flying line. Thermographic matrix have been reconstructed from raw data using dedicated processing approaches. SVD processing have been implemented for defect localization and combined with an inverse method to characterize defective areas.

It has been proven that the profile follow a temperature decay similar to the ones observed in a pulsed thermography. Therefore, a one dimensional thermal quadrupole model with an estimation procedure has been implemented to estimate the depth of the defect. This model represents rough simplification of the actual physical problem, such as, lateral diffusion,… . The Levenberg-Marquadt algorithm has been used for the minimization procedure for each pixel. This minimization procedure apply to infrared image reconstructed (434*352 pixels) may take more 90 h on a standard Labtop computer to obtain a *Thickness Map*. However, it should be possible to improve drastically the computation time (< some hours) by an efficient GPU (Graphical Processing Unit) during the implementation of parameter estimation. The estimation procedure for each pixel of infrared image reconstructed could be assigned to one thread block in the GPU.

Future work will address a series of complete scans of different academic shape panels using also transmission scanning and associated signal processing. Improvement in inverse model will be also studied to address three dimensional thermal phenomenon observed during some experiments.

Acknowledgment

Authors wish to thanks the Collaborative Research and Training Experience (CREATE) of the National Sciences and Engineering Research Council of Canada (NSERC) for supporting this work carried out in the framework of *oN DuTy!* Program. NSERC Discovery and Canada research chair programs are also acknowledged.

REFERENCES

[1] J.-C. Krapez, “Résolution spatiale de la caméra thermique à source volante,” Int. J. Therm. Sci., vol. 38, no. 9, pp. 769–779, 1999.

[2] L. Gaverina, J. C. Batsale, A. Sommier, and C. Pradere, “Pulsed flying spot with the logarithmic parabolas method for the estimation of in-plane thermal diffusivity fields on heterogeneous and anisotropic materials,” J. Appl. Phys., vol. 121, no. 11, p. 115105, 2017.

[3] T. Li, D. P. Almond, and D. A. S. Rees, “Crack imaging by scanning laser-line thermography and laser-spot thermography,” Meas. Sci. Technol., vol. 22, no. 3, p. 035701, 2011.

[4] N. Rajic, “Modelling of thermal line scanning for the inspection of delamination in composites and cracking in metals,” DEFENCE SCIENCE AND TECHNOLOGY ORGANISATION VICTORIA (AUSTRALIA) PLATFORM SCIENCES LAB, 2004.

[5] L.-D. Théroux, J. Dumoulin, and J.-L. Manceau, “Dynamic heating control by infrared thermography of prepreg thermoplastic CFRP designed for reinforced concrete strengthening,” in 12th International Conference on Quantitative InfraRed Thermography, 2014.

[6] L.-D. Théroux, J. Dumoulin, and E. Merliot, “Automatic installation of thermoplastic CFRP monitored by infrared thermography for pipelines,” Adv. Infrared Technol. Appl., p. 24, 2015.

[7] C. Ibarra-Castanedo and X. P. Maldague, “Pulsed phase thermography inversion procedure using normalized parameters to account for defect size variations,” in Proc. SPIE, 2005, vol. 5782, pp. 334–341.

[8] C. Ibarra-Castanedo, P. Servais, A. Ziadi, M. Klein, and X. Maldague, “RITA-Robotized Inspection by Thermography and Advanced processing for the inspection of aeronautical components,” in 12th International Conference on Quantitative InfraRed Thermography, 2014.

[9] W. J. Parker, R. J. Jenkins, C. P. Butler, and G. L. Abbott, “Flash method of determining thermal diffusivity, heat capacity, and thermal conductivity,” J. Appl. Phys., vol. 32, no. 9, pp. 1679–1684, 1961.

[10] N. Le Touz, T. Toullier, and J. Dumoulin, “Infrared thermography applied to the study of heated and solar pavement: from numerical modeling to small scale laboratory experiments,” in Thermosense: Thermal Infrared Applications XXXIX, 2017, vol. 10214, p. 1021413.

[11] N. Rajic, “Principal component thermography,” DEFENCE SCIENCE AND TECHNOLOGY ORGANISATION VICTORIA (AUSTRALIA) AERONAUTICAL AND MARITIME RESEARCH LAB, 2002.

[12] C. Ibarra-Castanedo, A. Bendada, and X. Maldague, “Thermographic image processing for NDT,” in IV Conferencia Panamericana de END, 2007, vol. 79.

[13] J. C. Krapez, F. Lepoutre, and D. Balageas, “Early detection of thermal contrast in pulsed stimulated thermography,” NDT E Int., vol. 6, no. 29, p. 393, 1996.

[14] X. Maldague, "Theory and practice of infrared technology for non-destructive testing", John Wiley & sons Inc., 2001.vier

[15] A. Crinière, J. Dumoulin, C. Ibarra-Castanedo, X. Maldague, "Inverse model for defect characterization of externally glued CFRP on reinforced concrete structures: Comparative study of square pulsed and pulsed thermography", Quantitative InfraRed Thermography Journal, Taylor & Francis Editor, vol 11, pp 84-114, 2014.

Conclusion

[1-5] L'objectif de ce travail est de proposer une inspection par thermographie par courants de Foucault robotisé. Pour ce faire, une étude théorique de la méthode et une revue de la littérature ont été achevées afin d'assimiler la physique ainsi que les capacités de la technique. Nous avons exécutés plusieurs simulations en variant différents paramètres. Les résultats de ces simulations ont été capitaux pour démontrer les capacités de la méthode. Ces derniers ont également donnés des éclaircissements et des données préalables aux expérimentations et à la façon de les réaliser.

Différentes expérimentations ont été achevées. La méthode d'inspection linescan de la thermographie par courants de Foucault a été testée avec différents paramètres et configurations. Cette dernière a été comparée à la thermographie optique. Ces expériences ont montré l'efficacité de notre plate forme robotique d'inspection. Aussi, les capacités ainsi que les limites de la méthode ont été explorées dans cette recherche.

Finalement, la thermographie robotique par courants de Foucault est nettement plus performante que l'inspection classique. L'utilisation de robot et de logiciels de traitement permet, en plus d'améliorer considérablement la détection de défaut, une inspection plus facile et plus précise pour l'opérateur. De plus, il est démontré que la méthode présente un avantage indéniable pour les spécimens métalliques (conducteurs) et offre des résultats intéressants sur la fibre de carbone.

La direction à explorer dans des travaux futurs serait d'améliorer le système pour des inspections de pièces plus complexes. On propose également plus de développement de l'automatique du système comme : lamélioration l'interface de contrôle du robot, plus de pré et /ou post-traitement, etc.

Annexe A

Optimised Dynamic line scan thermographic detection of CFRP inserts using FE updating and POD analysis

A.1 Résumé

La détection de délaminations sur les lamellés en composites par thermographie automatique est une tâche complexe. Les paramètres de la détection ne dépendent pas uniquement des équipements mais également du spécimen inspecté. Dans ce travail, une méthodologie est présentée s'appuyant sur un modèle en éléments finis (FEM) qui modifie les paramètres automatiquement établissant ainsi les paramètres optimaux pour un spécimen et les profondeurs de délaminations donnés. Les résultats obtenus sont comparés en termes de probabilités de détection (POD) par rapport à ceux d'un expert d'inspection. Les résultats montrent une amélioration dans la précision et les la vitesse d'inspection avec la complexité du spécimen inspecté et la baisse du POD.

A.2 Abstract

The detection of delaminations in composite laminates using automated thermographic scanning is a quite challenging task. The set-up parameters are not only dependent on the equipment, but on the inspected component as well. In this work, a methodology is discussed to use Finite Element (FE) model updating to automatically establish the most suitable inspection parameters for a given combination of the structure and the investigated delamination depths. The optimised results are compared using binary Probability of Detection analysis and are benchmarked with parameter sets retrieved by an expert using the regular trial er-

ror approach. The results show an improvement of the accuracy and scanning speed which significantly increases as the POD decreases and the complexity of the samples increases.

NDT and E International 93 (2018) 141–149

Contents lists available at ScienceDirect

NDT and E International

journal homepage: www.elsevier.com/locate/ndteint

Optimised dynamic line scan thermographic detection of CFRP inserts using FE updating and POD analysis

J. Peeters [a,*], C. Ibarra-Castanedo [b], F. Khodayar [b], Y. Mokhtari [b], S. Sfarra [c,d], H. Zhang [b], X. Maldague [b], J.J.J. Dirckx [f], G. Steenackers [a,e]

[a] University of Antwerp, Op3Mech, Groenenborgerlaan 171, B-2020, Antwerp, Belgium
[b] Laval University, Computer Vision and Systems Laboratory, Electrical and Computer Engineering Department, 1065 av de la Medecine, Quebec, G1V 0A6, Canada
[c] Las.E.R. Laboratory, Department of Industrial and Information Engineering and Economics (DIIIE), University of L'Aquila, Piazzale E. Pontieri 1, Loc. Monteluco di Roio, Roio Poggio, 67100, L'Aquila, AQ, Italy
[d] Tomsk Polytechnic University, Lenin Av., 30, Tomsk, 634050, Russia
[e] Vrije Universiteit Brussel, Acoustics & Vibration Research Group, Pleinlaan 2, B-1050, Brussels, Belgium
[f] University of Antwerp, Laboratory of Biomedical Physics, Groenenborgerlaan 171, B-2020, Antwerp, Belgium

ARTICLE INFO

Keywords:
Dynamic line scan
FE updating
Inverse problem
Automated NDT
Quantitative non-destructive evaluation
CFRP
Probability of Detection

ABSTRACT

The detection of delaminations in composite laminates using automated thermographic scanning is a quite challenging task. The set-up parameters are not only dependent on the equipment, but on the inspected component as well. In this work, a methodology is discussed to use Finite Element (FE) model updating to automatically establish the most suitable inspection parameters for a given combination of the structure and the investigated delamination depths. The optimised results are compared using binary Probability of Detection analysis and are benchmarked with parameter sets retrieved by an expert using the regular trial & error approach. The results show an improvement of the accuracy and scanning speed which significantly increases as the POD decreases and the complexity of the samples increases.

1. Introduction

Active thermography is a broadly used technology to inspect large, carbon fibre reinforced plastic (CFRP) components for flaws in a fast way [1–3]. To receive accurate results on large samples, the thermal camera has to be repositioned over the structure in a way each surface is inspected with sufficient accuracy with an equal heat excitation and time resolution considering directional emissivity [4–6]. To perform these sequential experiments in a robust, repetitive way, NASA developed a type of line Scan thermography (LST) whereby a robotised movement is used to reposition both the heating device as the infrared thermal camera in tandem [6–8]. Those ideas are based on the ideas of Maldague in 1993 [9] and on the work of Lindberg in 1968. Lindberg proposed the idea of a prism line-scanner for high speed thermography, at that time mono-detectors were used so even though the camera was not moving the laser heated the surface point-by-point and a reconstruction was performed to recover a complete image of the inspected surface [10]. In recent research, for the heating device, a thin line radiative heater is used and the acquired image sequence is processed to result in a pseudo-static representation of the full surface over time, to evaluate the subsurface integrity [1,6]. The NASA developed and patented technology of the 1990s, as described by Cramer et al. has since been used by more and more industrial branches for inspection of metallic and composite components [8,11]. There exists a similar technique with analogue problems, called the thermal-photocopier for which this work delivers similar insights [12]. The main difference with LST is that the camera remains fixed and only the heat source is moving.

Automatic scanning using a robotic arm is seen as an interesting way for Non-destructive Testing (NDT) of large and complex shaped components [6]. The programming of the inspection path, speed, excitation power and acquisition rate is a difficult task which is highly dependent on the inspected sample geometry and material properties [6,13]. This parameter optimisation is mostly done manually by a highly qualified inspector using experience and trial and error which is a time-consuming task for complex structures as the heat deposition and scanning speed should match the heat diffusion in the material [13]. Within this work, it

* Corresponding author.
E-mail address: jeroen.peeters2@uantwerpen.be (J. Peeters).
URL: http://www.op3mech.be

https://doi.org/10.1016/j.ndteint.2017.10.006
Received 3 November 2016; Received in revised form 2 May 2017; Accepted 17 October 2017
Available online 20 October 2017

is shown that using numerical model updating within the field of active thermography inspection can facilitate the set-up of the measurements by predicting the most ideal setup parameters. The optimised results are compared using a Probability Of Detection analysis to compare with the work flow by trial and error followed by a skilled inspector.

The use of Finite Element (FE) models is well integrated into the design of large structures, but in uttermost cases, the use of the FE models remains in the design stage. FE model updating can be used to optimise the complex parameter set of the LST set-up by correlating the numerical results with NDT data. These methods are widely used in modal vibration inspection [14–16], but their usage is limited in thermal optimisation problems [17,18] due to the difficulties in estimating the diffusivity.

The optimisation of LST set-up parameters using FE model optimisation is similar to the FE model updating techniques as described by Marwala [19] for modal analysis. There are a few differences with the well-known FE model optimisation routines for shape or model performance optimisations due to the complex interdependency between the experimental limitations (e.g. the experimental setup), for example, the camera sensitivity and the heat distribution of the excitation source. This results in a different manner of defining the objective function and solver choice described in Section 2.3.1. Besides, an extreme non-linear behaviour of the response to limited parameter differences and the different mathematical definition of thermal modes with respect to modal modes [20] results in the need for an accurate investigation of those influences.

The accuracy and the efficiency of an NDT technique, are mostly evaluated by using a Probability Of Detection (POD) analysis to determine the acceptance of a certain technique or to compare two distinguished technologies [21]. Probability of Detection (POD) is a statistical method used to estimate the proportion of defects of a given size that can be detected by a particular technique. It requires a large amount of samples having defects ranging from non-detectable to minimum detectable sizes and larger. PoD is often used to evaluate the reliability of a particular NDE method (x-rays, ultrasounds, Eddy currents, thermography, etc.), or a processing technique (principal components, Fourier transform, etc.), to detect a certain type of flaw (cracks, delaminations, impact damage, corrosion loss, etc.), at a given depth (or depth range) either manually or automatically. It has been utilised for years to validate the performance and reliability of NDE techniques such as ultrasounds and Eddy current techniques. In the case of infrared thermography, only a few POD studies can be found in the literature [22–25]. In this study, the number of targets (defects of different sizes and depths) is rather limited (25 per side, which gives a total amount of 50 defects to detect). Nevertheless, POD analysis in this work is performed in order to receive an objective comparison between the optimised detection results and the results received by an experienced LST inspector and a randomly chosen parameter set. The amount of literature related to POD analyses of active thermography and especially for LST techniques is limited [21]. Due to the importance of the parameter optimisation, the implementation of statistical methods for the evaluation of the accuracy of the experimental set-up is provided in this manuscript. To perform an accurate POD analysis, a great amount of defective samples are required, with known defects ranging from non-detectable to good detectable size/depth ratios (D/d), also called aspect ratios [21,26]. In this work, the discrete hit/miss evaluation technique is used on the same test sample that was employed by Duan et al. to deliver comparable results [21].

2. Materials & methods

2.1. Experimental set-up

The experimental inspections were performed on a CFRP sample, widely described in literature [27,28], with a thickness of 2 mm with 25 Teflon square inserts with lateral sizes $D = 3, 5, 7, 10$ and 15 mm placed between each consecutive ply at different depths, varying of $0.2 < d < 1$ mm from the front side and $1 < d < 1.8$ mm from the rear side, and locations as shown in Fig. 1. The specimen is tested from both sides which result in a total of 50 inspected flaws with different aspect ratios varying from 3/1.8 to 15/0.2). The sample is built from 10 unidirectional prepreg carbon fibre plies consisting of Hexcel AS4/3501-6, 300 AW with 31% remaining resin after cure. The stacking within the sample follows a symmetric $[0\ 90]_{5\text{-}s}$ order. The test sample is fabricated using standard autoclave curing cycle. The sample is inspected using an inspection tool consisting of a FLIR A65sc microbolometric LWIR $7.5 - 14\mu m$ camera with a spatial resolution of 640×512 pixels for the data acquisition and an IR Heater of 30 cm with a total power of maximum 1500W as a heat source. The inspection tool is attached to a 6 degree of freedom FANUC LR Mate 200iD 7L robotic arm and makes use of consecutive linear scan paths starting from the same side of the sample. A photograph of the experimental set-up is shown in Fig. 2.

2.2. Numerical model description

The numerical model was developed using COMSOL Multiphysics 5.0 software based on the Finite Element technique. The model simulates the moving heat source of the LST set-up over the inspected test sample using multibody dynamics combined with heat transfer. The heat conductivity through the different material layers is simulated to implement the anisotropic behaviour of the lateral heat diffusion. A constant Newtonian non-linear method is used with a modernised implementation of the DAE solver within the heat transfer routine. This solver is based on the backwards differentiation formulas [29]. Linear tetrahedral Lagrange elements are used to simulate the behaviour of the material on the moving thermal heat source. The model consists of 41 406 elements with an average growth rate of 2.2 and an average element quality of 0.565. The model consists of a stacking of different layers for each CFRP ply with thermal anisotropic properties dependent on the fibre orientation of the ply. The different layer properties are estimated using a model where each ply consist of uniform carbon fibres with only one longitudinal conductivity and one different transversal in-plane conductivity. Between each ply, a thin epoxy layer is modelled to simulate the practical, not ideal contact layer between each carbon ply with the third variable conductivity coefficient, perpendicular to the plies. With this stacking recipient a quasi-isotropic laminate is represented. A detailed picture of the 3D mesh with the different layers is shown in Fig. 3.

- 5 CFRP layer of 0.25 mm thick with a global fibre orientation of 0°C, in figure in blue represented.
- 5 CFRP layer of 0.25 mm thick with a global fibre orientation of 90°C, in figure in green represented.

Some simulation results are shown in Fig. 4 and Fig. 5 for the full inspected plate. The essence of mesh convergence is acknowledged within this research and might result in significant errors within the updating routine. The computed model within this manuscript is checked

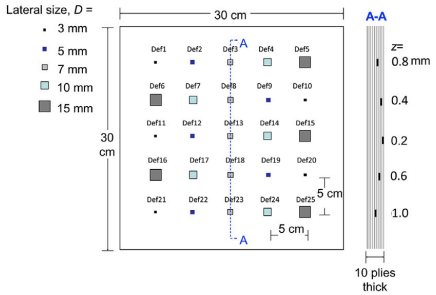

Fig. 1. Technical drawing of the CFRP inserts.

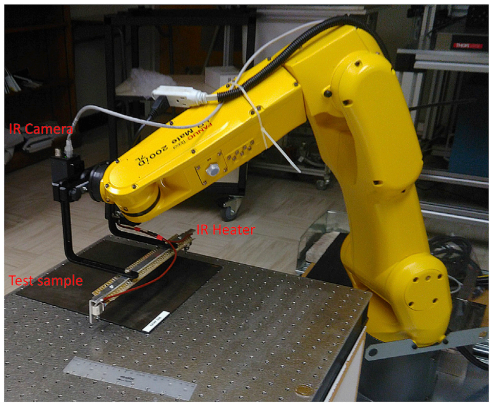

Fig. 2. Experimental set-up of the dynamic line scan.

on mesh convergence with a minimum acceptance rate of 95% accuracy on temperature level when the mesh is changed. It is found that the elements can be made rather large within this constraint for thermal simulations. The geometrical complexity by simulating the thin teflon inserts force the use of a smaller mesh which is more robust with respect to mesh convergence due to the minimal element quality needed in the area close to the simulated defects. A representation of the performed mesh convergence is shown with respect to temperature on a probe point on a certain time stamp in Fig. 6. A red asterisk shows the used mesh within the optimisation routine.

2.2.1. *Modelling of the excitation source*

The tubular carbon excitation source results in a non homogeneous spatial distributed heat excitation which is shown in Fig. 7. This spatial distribution is implemented in the excitation source modelling to correlate the spatial heat distribution on the inspected test sample according to the distribution in the X-axis. The narrow distribution in the Y-axis is transposed to the temporal distribution due to the lateral movement of the heat source.

The movement of the heat source is simulated using a moving mesh for the radiating heat source with a horizontal speed perpendicular to the inspected surface which is equal to the robot speed around the global world coordinate system. The world coordinate system itself is placed similarly in the numerical model as for the robot used in the experimental measurements.

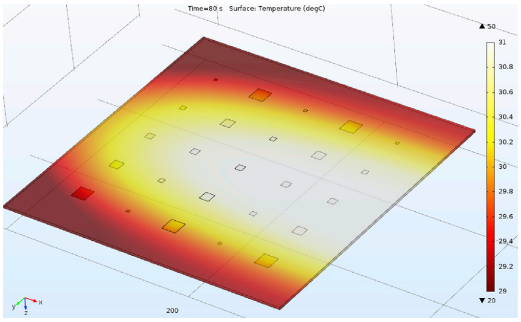

Fig. 4. Simulation result of the optimised numerical model (scale in degC).

2.2.2. *Physical boundary conditions*

For the heat transfer module in the simulation model, it is important to implement surface to surface radiance between the moving heat source and the upper surface of the test sample. Besides the radiative energy exchange between the heat source and the sample, the cooling mechanisms: convection and ambient radiation were also taken into account. A representation of the overall numerical model is shown in Fig. 4 that corresponds to the time when the heat source has moved for 80 s and already passed the inspected plane.

The governing differential equation is a combined heat transfer equation with conduction, convective cooling and radiation of an

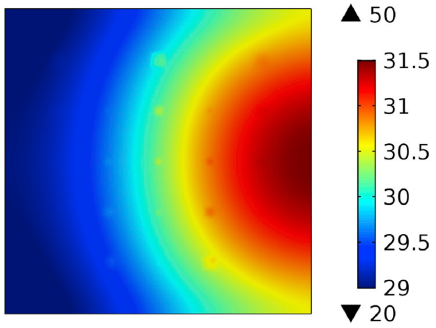

Fig. 5. Spatial simulation result during LST simulation where the detection of the defects on different depths is visualised.

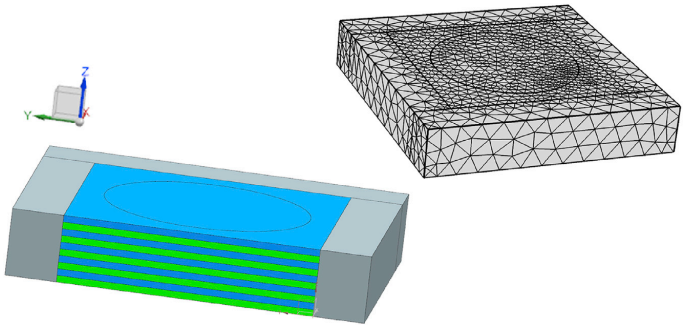

Fig. 3. Overview of a subsection of the 3D mesh on the test sample with the different plies schematically represented by different colors.

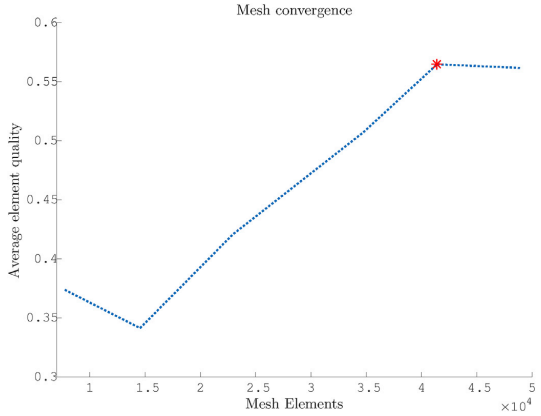

Fig. 6. Mesh convergence analysis on 3D mesh.

external heat source, formulated in Eq. (1)– (3) where ρ is the density, C_p is the heat capacity at constant pressure, T is the absolute surface temperature, κ is the thermal conductivity, t is the time, $Q(t)$ is the time dependent heat source, h is the coefficient of convection and σ is the constant of Stefan-Boltzmann [30,31].

$$\rho C_p \frac{\partial T}{\partial t} + \nabla\cdot(-\kappa\nabla T) = Q \; with \; T(x,y,z,0) = T_\infty = 292.88[K] \tag{1}$$

$$\overrightarrow{n}(k\nabla T) = h(T_\infty - T) \tag{2}$$

$$\overrightarrow{n}(k\nabla T) = \varepsilon\cdot\sigma\cdot\left(T_\infty^4 - T^4\right) \tag{3}$$

A few assumptions are made:

- The air velocity is assumed to be zero allowed by the laboratory conditions.
- The lay-up of the CFRP laminate is considered quasi-isotropic with structured fibre angles in a woven pattern.
- The test sample is opaque and behaves like an ideal grey body as a result of the mate epoxy surface.

The physical properties used in the numerical model are shown in Table 1.

The accuracy of the material properties within the used test sample is validated within previous work on the test sample as provided in Ref. [35]. Using a similar optimisation routine, the material properties of the test sample are estimated with respect to the known simulated defect depths, represented by the teflon inserts. Therefore the inspection is validated with a standard pulsed thermography inspection. The accuracy of prediction of the defect depths is related to the accuracy of modelling the thermal diffusivity α in the test sample which gives a clear indication on the uncertainty of the used material properties. This is shown in Fig. 8 where the importance of precise material properties within the numerical model is provided. The numerical model using standard material properties delivers the worst estimation of defect depths, especially when the defect depth increases. Due to the optimisation of the material properties, the accuracy is significantly increased.

2.3. Optimisation routine

The adaptive response surface optimisation routine is used to optimise numerical models with lots of data points and the time reducing by the algorithm increases as the number of parameters increases [14]. The routine is designed to handle multiple-output time series data [18]. The optimisation procedure can be divided into the following steps:

1. Starting reference simulation points is running and a correct object function is built of the difference between the FE model and the optimal target values defined in the objective function.
2. The FE model is replaced by a spline-based meta-model of response surfaces to decrease the optimisation time but remains an accurate approximation.
3. The optimisation routine is run on the specific object function to find the minimum for the meta-model. There is made use of an optimisation routine according to a genetic algorithm computation to find the optimum fast for the complex numerical model. Thereby the amount of FE solutions is further reduced.
4. The estimated parameter values are used as input parameters for an improved FE model that corrects the meta-model.
5. Only the points closer to the minimum are used to form the response surface (pan & zoom function).

The response model which is optimised is not built from a pre-defined number of design experiments, but is adapted and refined during the optimisation routine by the pan and zoom command [18]. The method automatically calculates the parameter influence sensitivity and sequentially resolves multiple sets with first the major influencing parameters with fixed parameter values for the minor influencing

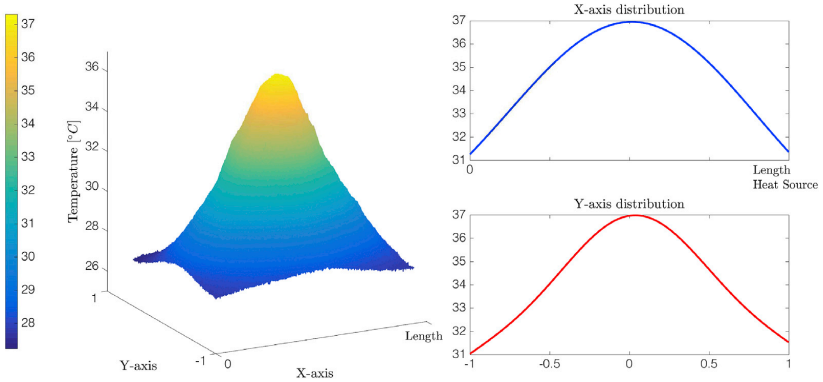

Fig. 7. Spatial temperature distribution of the heat source.

Table 1
Material properties within the numerical model [32–34].

Parameter	Conductivity $k_{long}(W/m{\cdot}K)$	Conductivity $k_{trans}(W/m{\cdot}K)$	Specific heat capacity CFRP $C_p[J/(Kg.K)]$	Density CFRP $\rho[kg/m^3]$	Heat transfer coefficient $W/(m^2.K)$	Emissivity
Carbon	60	4.2	1000	1580	10	0.85
Teflon	0.265	0.265	950	2175	10	0.92

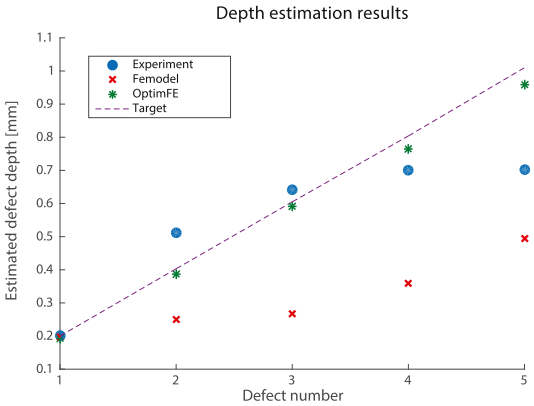

Fig. 8. Depth estimation using standard pulsed thermography data on the CFRP test sample, the numerical model with standard material properties and the numerical model with optimised material properties.

parameters. Succeeding, the second parameter set is optimised and finally an influence check is performed for all parameter sets until the results converge.

2.3.1. Objective function declaration

For the optimisation of the line scan thermography system, the declaration of the objective function is essential and closely related to the optimised experimental parameters. The most important parameters that influence the efficiency and accuracy of the thermal line scanning are:

- Robot speed u along the scanning direction;
- Excitation power P;
- Distance between heat source and the test sample d.

These parameters have implicit dependencies on the following parameters, which results in the complex objective function declaration:

- Image acquisition rate;
- Field of View (FOV);
- Scanning path;
- Minimum defect resolution.

It should be noted that these parameter values are highly dependent on the material properties of the structure under inspection.

The FOV is used to determine for each time instance which part of the inspected structure is visible using basic optical formulation represented in Eq. (4), with D the perpendicular distance between the camera and the structure. The scanning time is computed and minimised using basic path planning in combination with the robot speed u. This is combined with the computation of the minimal and maximal time instances, each point should be visibly related to the depth estimation of a possible defect according to Eq. (5), where α is the thermal diffusivity (m^2/s), C_1 a constant equal to 1.8 [27], f_b the blind frequency (Hz) and μ the diffusivity length (m). Therefore, the structure is divided into layers, related to the effective material layers defects are located. Reported experimental values of the constant C_1 are: $C_1 = 1$ when using amplitude data [36], and in the range $1.5 < C_1 < 2$ [36–41] when working with the phase. The value $C_1 = 1.8$ is typically adopted [37,38] following the research work by Thomas et al., 1980 [42]. The phase is therefore of more interest in NDT than the amplitude, since it provides deeper probing capabilities than the amplitude. Thereby, the inspection routine is optimised for the material and structure thickness of the specific structure.

$$x = 2{\cdot}D{\cdot}tan\left(\frac{HFOV}{2}\right) \tag{4}$$

$$z = C_1\sqrt{\frac{\alpha}{\pi{\cdot}f_b}} = C_1{\cdot}\mu \tag{5}$$

These preparing criteria are combined with the objective function in which the total scanning time is minimised and the relative temperature difference between sound area and possible defective area is maximised. An important limit in the objective function is the maximum surface temperature of the structure which is dependent on the inspected material and which can overrule the objective function value to ignore certain unsafe inspection configurations. For the CFRP test sample, the maximum allowed surface temperature on which the surface in the numerical model is exposed to, is set to 323 K. By implementing this boundary condition in the optimisation routine, a precaution is implemented to keep the non-destructive intention of the inspection routine.

2.4. Probability of Detection

A Probability of Detection (POD) analysis is performed to receive an objective comparison between the optimised detection results and the results received by an experienced LST inspector and a randomly chosen parameter set. A discrete hit/miss response is used in accordance with the work of Duan et al. [21]. The data is organised in a way that a defect is either detected (hit = 1) or not (miss = 0). The defect characterization is performed in relation to the aspect ratio using the log-odd model and a linear least square weighted special maximum likelihood method to estimate the model parameters [21]. The experimental and numerical results are first post-processed using Principal Component Thermography (PCT) to improve the defect detection capabilities [21,43]. In relation to the work of Duan et al., there is used a region surrounding, but not containing, each defect as sound area. The size of the sound area is chosen in relation to the inspected defect with an equal surface. This comparison is used to perform an objective evaluation of the hit/-miss criteria.

3. Results & discussion

In the following section, the results of the optimisation routine are compared with the set-up parameters defined by an expert in dynamic line scan thermography and several iterative defined set-up parameter sets. The optimisation routine is validated on three different datasets performed on the CFRP006 sample. A representation of the Detected inserts after PCT post-processing is shown in Fig. 9 for the shallow test sample. All parameter sets are described by:

1. D = perpendicular distance between the test sample and the heat source (mm);

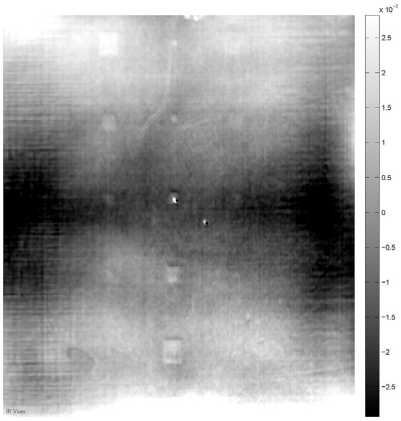

Fig. 9. Detected teflon inserts in the shallow side of the testsample after Principal Component analysis.

2. u = speed of the robot arm (m/s);
3. P = power of the heat source (%) of 1500W;
4. d = horizontal distance between the camera and the heat source (mm).

The parameter set which is defined by the expert and the final parameter set after the optimisation routine are noted in the following figures.

3.1. Shallow side

The shallow side was analysed two times, one time for the data without adding extra noise and one time with extra noise added. Due to the very shallow defects of 0.2–1 mm, the defect ratio is higher than 84%. As a result of the high detection ratio, the fitting of the POD curves is not consistent and the interpretation of these data sets is not applicable. One of the risks is a misinterpretation of the results as shown in Fig. 10. It is shown in Fig. 10b that the raw data should deliver a more accurate POD than the post-processed PCT data, which is in contrast to the findings of Duan et al. [21]. This is the reason that explains why it is important to use datasets with enough miss and hit data [44].

3.2. Shallow side with noise

To use the shallow data set and to optimise the set-up for shallow structures it is essential to increase the amount of miss data to provide impossible to detect defects. It was chosen to do this by adding Gaussian noise to the camera data set. In this way, a camera is simulated with a higher NETD value. After the addition of the Gaussian noise, there are multiple defects that are impossible to detect and while some others are visible in all cases. A Gaussian distribution was chosen in order to avoid influence between the comparison of the RAW and PCT processed data. The results of the POD analysis are shown in Fig. 11.

After adding the noise it is shown in Fig. 11a that both the expert and the optimised results deliver similar POD curves and the differences for shallow defects are rather small. A major remark with these results is that due to the high distance D of the optimised results, it is possible to scan the object in one pass in contrast to the very low D of the expert set-up. This results in a lower scanning time and an easier scanning path of the optimised results in contrast to the path of the expert set-up which needs three passes. The implementation of PCT post-processing gives a major improvement, especially for the parameter sets with a higher D distance, which results on a lower spatial resolution. By post-processing the RAW measurements with PCT, the contrast is improved and the effect of smaller spatial resolution is reduced [43].

3.3. Comparison shallow side with traditional active thermography

To verify the relevance of the performed measurements, a comparison is made with measurements performed by Duan et al. [21] on the same test sample. Within their setup, data acquisition was carried out using a Focal Plane Array (FPA) infrared camera (Santa Barbara Focalplane SBF125, 3 to 5 μm) with a 320×256 pixels array [21]. Besides, two high-power flashes (Balcar FX 60), each giving 3.2 kJ for 5 ms pulse duration, were used as heating sources in reflection mode [21]. The benchmark should be made on POD level and not on spatial quality of the measurement as there is made use of different equipment with different NETD levels and spatial resolution. An overview of the comparison is showed in Fig. 12. The differences are limited and in advantage of the optimised LST measurements. It can be concluded that the measurements are performed adequate with respect to the state-of-the-art.

3.4. Deep side

The deep side has simulated defects between 1 and 1.8 mm as described in section 2.1. The POD analysis is plotted versus the Aspect ratio which gives the relation to the size/depth ratio. Due to the depth and difficulty to detect the Teflon inserts on larger depths ($> 1mm$), the detection rate is less than 28%. The different set-up variations are compared after PCT post-processing in Fig. 13. It is shown that both the expert set and the optimised set of parameters deliver the best results, compared with the other parameter sets which are the result of a manual iterative process using trial and error. The optimised set is slightly better than the expert set and it should be remarked that by coincidence there is found a different parameter set during the iterative process which gives almost the same accuracy (D50). An important benefit of the optimised result is the consideration of scanning time. The higher the D distance, the fewer passes there are necessary and the faster the inspection could be performed. For this reason, the D160 set of parameters is preferred by the optimisation routine over the D50 set.

It should be pointed out that the optimised distance between the sample and the source D is smaller than the one required for the shallow side of the test sample. This is a logical and expected result considering that a smaller D implies that more energy is delivered to the surface, and as a consequence, deeper probing is possible.

At the same time, the optimisation algorithm proposed a scanning speed u much higher for the deep side as the decrease in D compensates for the loss of energy that a faster scanning would imply. In this way it is made possible to define a suitable set of inspection parameters necessary to detect defects of the individual structure.

3.5. Shallow versus deep side

An interesting validation can be performed by comparing the overlapping defects at a depth of 1 mm between the shallow and deep measurements. In Fig. 14 both the POD curves and the binary detection rates are plotted. The POD curves are build from the combined measurements but exclusively from the data of the 1 mm defects. The binary hit-miss data is split in the two different measurements. The Deep side of the testsample is represented by circles and the Shallow side by crosses. It can clearly be seen that the results are equal for all aspect ratios except the one where the binary results flip from zero to one as can be seen in Fig. 14. For the D40 case, the defect with aspect ratio 5 is not visible in contrast with the other parameter sets. A reasonable explanation can be found in the flipping point at this aspect ratio from not visible below aspect ratio 5 to visible above this aspect ratio and uncertainty due to measurement noise. The overlapping data of the testcase on a distance D equal to 250 mm is neglected in Fig. 14 as for both sides 0 defects are found in this dataset. Thereby we can conclude that the data is consistent

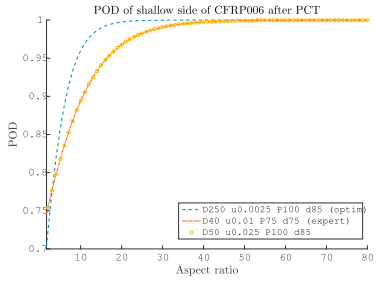

(a) Comparison of the Probability of detection for all parameter sets of the shallow test case after implementing PCT detection enhancement.

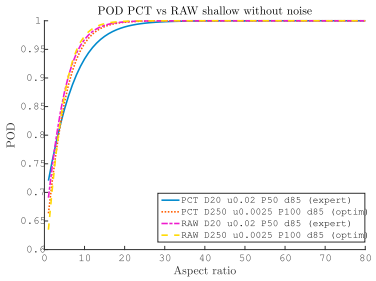

(b) Comparison of the Probability of Detection between the raw measurements and after post processing for both optimisation as expert parameter sets.

Fig. 10. Analysis of shallow side of CFRP006 without noise adding. The legend is described in front of section 3.

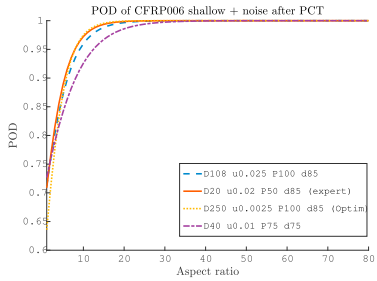

(a) Comparison of the Probability of detection for the shallow test case after adding Gaussian noise after implementing PCT detection enhancement.

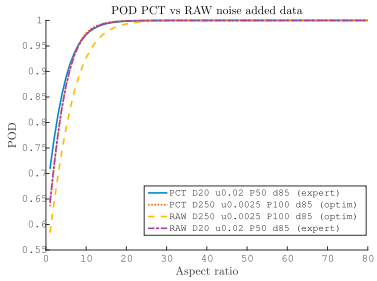

(b) Comparison of the Probability of Detection between the raw measurements and after post processing after adding Gaussian noise.

Fig. 11. PoD analysis of shallow side of CFRP006 with Gaussian noise added.

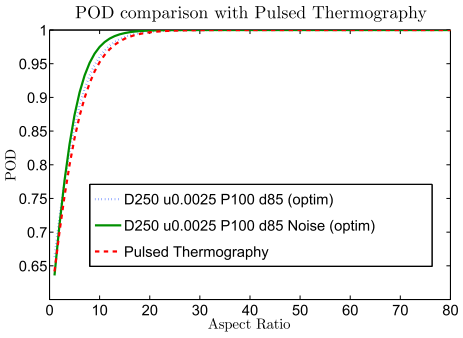

Fig. 12. Probability of Detection for the shallow defect cases and standard pulsed thermography after PCT post-processing. The legend is described in front of section 3.

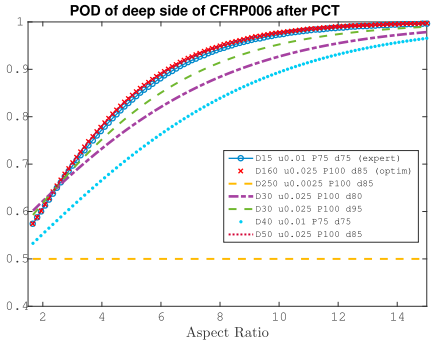

Fig. 13. Probability of Detection for the deeper defect case on the CFRP006 sample after PCT post-processing. The legend is described in front of section 3.

for the overlapping setups between the two different sides.

4. Conclusions

The use of FE updating techniques can provide dynamic line scan setups with similar accuracy as set-up by an active thermography expert, with the added value that it automatically considers scanning time and path planning. The proposed method searches for the best possible measurement configuration to find the most defects in the specific structure. So if the range of depths is very broad, it will search for an

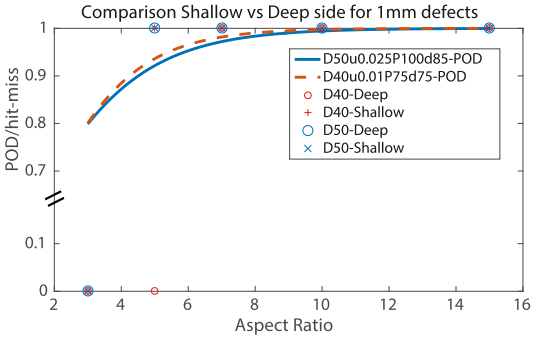

Fig. 14. Comparison of 1 mm defects measured from both sides.

optimum on which the shallow defects are still visible, the surface temperature is not to high and the deeper defects are starting to occur. In this way, it can be possible to efficiently modify NDE set-ups to inspect different serial produced complex parts and validate their accuracy using POD analysis. In longer term, the implementation of FE model updating in active thermography set-ups can support thermographers in choosing the most efficient measuring set-up for complex shaped surfaces made of multiple materials. In this work an important keystone is provided which shows the implementation for shallow and deeper hard to detect Teflon inserts in a CFRP laminate. The results are validated on a flat surface. Continuing research will be performed to further improve the technology to implement directional emissivities.

Acknowledgements

The research leading to these results has received main funding from The Research Fund - Flanders FWO travel grant V4.010.16N and the University of Antwerp. The authors also acknowledge the Flemish government (GOA-Optimech) and the research council of the University of Antwerp (fti-OZC) for its funding. Furthermore the authors want to thank the support of the Canada Research Chair in Multipolar Infrared Vision (MIVIM) for supporting this research. We acknowledge also the support of the Natural Sciences and Engineering Research Council of Canada. At last the authors would like to thank the colleagues of the Op3Mech (B) and LVSN (CA) laboratories for their help.

References

[1] Maldague X. Theory and practice of infrared thermography for nondestructive testing. New York: Wiley; 2001. http://scholar.google.com/scholar?hl=en&btnG=Search&q=intitle:theory+and+practice+of+infrared+thermography+for+nondestructive+testing#0.
[2] Vollmer M, Möllmann K. Infrared thermal imaging: fundamentals, research and applications. Berlin: Wiley-VCH; 2010. http://books.google.com/books?hl=en&lr=&id=5SSiZAMwxtYC&oi=fnd&pg=PR15&dq=Infrared+thermal+imaging:+fundamentals,+research+and+applications&ots=ClTOKRc2sH&sig=oRgWvTf06VZj2g0iXLoElTWHaxs.
[3] Avdelidis N, Almond D, Dobbinson A, Hawtin B. Pulsed thermography : philosophy, qualitative and quantitative analysis on certain aircraft applications. Insight 2006;48:286–9.
[4] Peeters J, Ribbens B, Dirckx JJJ, Steenackers G. Determining directional emissivity: numerical estimation and experimental validation by using infrared thermography. Infrared Phys Technol 2016. https://doi.org/10.1016/j.infrared.2016.06.016.
[5] Hoshimiya J, Hoshimiya T. Whole-electronic line-focus light-scanner for active thermography. In: QIRT2014 conférence; 2014. p. 1–6.
[6] Ibarra-Castanedo C, Servais P, Ziadi A, Klein M, Maldague X. RITA - robotized Inspection by Thermography and Advanced processing for the inspection of aeronautical components camera heating source actuator camera heating. In: QIRT2014 conférence; 2014. p. 1–8.
[7] Schmidt T, Dutta S, Ullmann T. Quantitative InfraRed thermography production integrated NDT by means of automated thermography. In: International conference on quantitative infrared thermography; 2012. p. 10.
[8] Cramer KE, Winfree WP. Thermographic detection and quantitative characterization of corrosion by application of thermal line source. Proc SPIE Int Soc Opt Eng 1998;3361:291–300. https://doi.org/10.1117/12.304740. https://www.scopus.com/inward/record.uri?eid=2-s2.0-0032403325&partnerID=40&md5=2fbc572776c36f0aaff7f84e7e3167d8.
[9] Maldague XPV. Nondestructive evaluation of materials by infrared thermography. London: Springer London; 1993. https://doi.org/10.1007/978-1-4471-1995-1. arXiv:arXiv:1011.1669v3, https://books.google.be/books?id=6MHcBwAAQBAJ. http://link.springer.com/10.1007/978-1-4471-1995-1.
[10] Lindberg P. A prism line-scanner for high-speed thermography. Opt Acta Int J Opt 1968;15(4):305–16. https://doi.org/10.1080/713818101. http://www.tandfonline.com/doi/abs/10.1080/713818101.
[11] Mistras. MIstras Line Scan thermography: necessary in industry. 2012. https://spinoff.nasa.gov/Spinoff2012/ip_4.html.
[12] Woolard DF, Cramer KE. The thermal photocopier: a new concept for thermal NDT. SPIE 2004;5405:366. https://doi.org/10.1117/12.541881.. In: http://proceedings.spiedigitallibrary.org/proceeding.aspx?doi=10.1117/12.541881.
[13] Ley O, Godinez-Azcuaga V. Line scanning thermography and its application inspecting aerospace composites. In: 5th international symposium on NDT in aerospace; 2013. p. 13–5. http://www.ndt.net/article/aero2013/content/papers/48_Godinez-Azcuaga.pdf.
[14] Steenackers G, Guillaume P. Finite element model updating taking into account the uncertainty on the modal parameters estimates. J Sound Vib 2006;296(4–5):919–34. https://doi.org/10.1016/j.jsv.2006.03.023. http://linkinghub.elsevier.com/retrieve/pii/S0022460X06002719.
[15] Meo M, Zumpano G. Damage assessment on plate-like structures using a global-local optimization approach. Optim Eng 2008;9(2):161–77. https://doi.org/10.1007/s11081-007-9016-0.
[16] Mottershead J, Friswell M. Model updating in structural dynamics: a survey. 1993. https://doi.org/10.1006/jsvi.1993.1340. http://www.sciencedirect.com/science/article/pii/S0022460X83713404.
[17] Cheng H-C, Tsai Y-H, Chen K-N, Fang J. Thermal placement optimization of multichip modules using a sequential metamodeling-based optimization approach. Appl Therm Eng 2010;30(17–18):2632–42. https://doi.org/10.1016/j.applthermaleng.2010.07.004. http://linkinghub.elsevier.com/retrieve/pii/S1359431110002875.
[18] Peeters J, Arroud G, Ribbens B, Dirckx J, Steenackers G. Updating a finite element model to the real experimental setup by thermographic measurements and adaptive regression optimization. Mech Syst Signal Process 2015;64–65:428–40. https://doi.org/10.1016/j.ymssp.2015.04.010. http://linkinghub.elsevier.com/retrieve/pii/S0888327015001697.
[19] Marwala T. Finite-element-model updating using computational intelligence techniques. Springer; 2010. http://books.google.com/books?id=ObtwUF1uAqMC&pgis=1.
[20] Nagle RK, Saff EB, Snider AD. Fundamentals of differential equations and boundary value problems. Pearson Education; 2012.
[21] Duan Y, Servais P, Genest M, Ibarra-Castanedo C, Maldague XPV. ThermoPoD: a reliability study on active infrared thermography for the inspection of composite materials. J Mech Sci Technol 2012;26(7):1985–91. https://doi.org/10.1007/s12206-012-0510-8.
[22] Hodge AJ, Walker JL. Probability of detection study on impact damage to honeycomb composite structure using thermographic inspection. In: Proc. 40th international SAMPE technical conference (ISTC), Memphis; 2008.
[23] DiMambro J, Rackow KA, Roach DP, Shepard SM, Ahmed T. A composite honeycomb probability of detection (POD) experiment using an uncooled infrared camera for pulsed thermography. In: 49th annual air transport association (ATA) NDT forum, ft. Worth north, TX, USA; 2006.
[24] DiMambro J. Quantitative evaluation of emerging infrared thermography technologies for aerospace applications. In: Chen CH, editor. Ultrasonic and advanced methods for nondestructive testing and material characterization. World Scientific; 2007. Ch. 15.
[25] Guo Y, Ruhge FR. Comparison of detection capability for acoustic thermography, visual inspection and fluorescent penetrant inspection on gas turbine components. In: AIP conference proceedings, vol. 1096; 2009. p. 1848–54. https://doi.org/10.1063/1.3114183.
[26] Ginzel E. Introduction to the statistics of NDT. NDT Net 2006;11(5):1. http://www.ndt.net/article/v11n05/ginzel2/ginzel2.htm.
[27] Ibarra-Castanedo C, Maldague XPV. Interactive methodology for optimized defect characterization by quantitative pulsed phase thermography. Res Nondestruct Eval 2005;16(4):175–93. https://doi.org/10.1080/09349840500351846.
[28] Lopez F, Ibarra-Castanedo C, de Paulo Nicolau V, Maldague X. Optimization of pulsed thermography inspection by partial least-squares regression. NDT E Int 2014;66:128–38. https://doi.org/10.1016/j.ndteint.2014.06.003. http://linkinghub.elsevier.com/retrieve/pii/S0963869514000760.
[29] Brown P, Hindmarsh A, Petzold L. Using Krylov methods in the solution of large-scale differential-algebraic systems. SIAM J Sci Comput 1994;15:1467–88.
[30] Chapman AJ. Heat transfer. fourth ed. New York: Macmillan; 1984.
[31] Stotter B, Gresslehner K, Mayr G, Hendorfer G, Sekelja J. Quantitative application of pulse phase thermography to determine material parameters. In: Quantitative infrared thermography(qirt)-Bordeaux, Bordeaux; 2014. p. 10. http://qirt.org/archives/qirt2014/QIRT 2014 Papers/QIRT-2014-074.pdf.
[32] (Comsol Multiphysics), Comsol documentation. 2015.
[33] CES Edupack 2013. Granta Design Limited; 2013.
[34] Joven R, Das R, Ahmed A, Roozbehjavan P, Minaie B. Thermal properties of carbon fiber epoxy composites with different fabric weaves. In: SAMPE international symposium proceedings; 2012. p. 14.

[35] Peeters J, Ibarra-Castanedo C, Sfarra S, Maldague X, Dirckx J, Steenackers G. Robust Quantitative Depth Estimation on CFRP samples using active thermography inspection and numerical simulation updating. NDT E Int 2017;87:119–23. https://doi.org/10.1016/j.ndteint.2017.02.003. http://linkinghub.elsevier.com/retrieve/pii/S0963869517300920.
[36] Busse G, Rosencwaig A. Subsurface imaging with photoacoustics. Appl Phys Lett 1980;36(10):815–6. https://doi.org/10.1063/1.91327.
[37] Meola C, Carlomagno GM, Giorleo L. The use of infrared thermography for materials characterization. J Mater Process Technol 2004;155:1132–7.
[38] Meola C, Carlomagno GM. Recent advances in the use of infrared thermography. Meas Sci Technol 2004;15(9):R27–58. https://doi.org/10.1088/0957-0233/15/9/R01.
[39] Bai W, Wong BS. Evaluation of defects in composite plates under convective environments using lock-in thermography. 2001. https://doi.org/10.1088/0957-0233/12/2/303.
[40] Busse G. Nondestructive evaluation of polymer materials. NDT E Int 1994;27(5):253–62. https://doi.org/10.1016/0963-8695(94)90130-9. http://linkinghub.elsevier.com/retrieve/pii/0963869594901309.
[41] Ibarra-castanedo C. Quantitative subsurface defect evaluation by pulsed phase thermography. Ph.D. thesis. 2005.
[42] Thomas RL, Pouch JJ, Wong YH, Favro LD, Kuo PK, Rosencwaig A. Subsurface flaw detection in metals by photoacoustic microscopya. J Appl Phys 1980;51(2):1152–6.
[43] N. Rajic, Principal component thermography, defense science and techno. URL http://oai.dtic.mil/oai/oai?verb=getRecord&metadataPrefix=html&identifier=ADA405857.
[44] Non-destructive evaluation system reliability assessment, military handbook. US Air force Aeronautical Systems Center; 2009.

Annexe B

Automatic dynamic inspection using active infrared thermography

B.1 Résumé

La thermographie active est une méthode prouvée efficace dans une large variété d'applications. Dans l'approche la plus commune utilisant une configuration statique, les éléments impliqués dans l'inspection ne bougent pas. Cette approche présente un sérieux inconvénient dans les inspections de larges spécimens. L'approche dynamique est une alternative. Cette dernière permet l'inspection de larges spécimens avec une meilleure résolution mais la reconstruction des données est nécessaire. Dans ce travail, deux méthodes dynamiques sont étudiées. Le mode photocopieuse et le mode linescan. Des méthodes automatiques robustes sont proposées pour établir le profil de température. Ce qui donne une séquence pseudo statique qui peut être traité en utilisant des algorithmes de traitement de données pour améliorer la détection. Les résultats montrent la robustesse de la méthode proposée et la capacité d'inspecter de larges pièces avec dexcellents résultats.

B.2 Abstract

Active thermography is a proven technology used in a wide variety of applications. In the most common approach using a static configuration, the elements involved in the inspection do not move. This presents serious drawbacks when it is applied to the inspection of large products and machines. An alternative approach is the dynamic inspection, which enables the inspection of large and complex products with better resolution, but it is also extremely challenging as data reconstruction is necessary. This work analyzes two methods for dynamic inspection using active infrared thermography : the thermal photocopier and the line scan. Automatic robust methods are proposed to calculate the temperature-time history, producing a pseudo-static sequence that can be further processed using advanced data processing

algorithms to improve defect detection. Results demonstrate the robustness of the proposed methods and the ability to inspect large products with excellent results.

Automated dynamic inspection using active infrared thermography

Active thermography is a proven technology used in a wide variety of applications. In the most common approach using a static configuration, the elements involved in the inspection do not move. This presents serious drawbacks when it is applied to the inspection of large products and machines. An alternative approach is the dynamic inspection, which enables the inspection of large and complex products with better resolution, but it is also extremely challenging as data reconstruction is necessary. This work analyzes two methods for dynamic inspection using active infrared thermography: the thermal photocopier and the line scan. Automatic robust methods are proposed to calculate the temperature-time history, producing a pseudo-static sequence that can be further processed using advanced data processing algorithms to improve defect detection. Results demonstrate the robustness of the proposed methods and the ability to inspect large products with excellent results.

***Index Terms*—Active thermography, dynamic inspection, Line scan, Thermal photocopier**

I. Introduction

There is an increasing demand for lighter and stronger industrial machines and products that can be subjected to extreme stress with better damage tolerance. Monitoring and testing are fundamental aspects for efficient and safe industrial manufacturing to increase reliability, and prevent failures and accidents in these rapidly changing industrial conditions.

Infrared thermography (IRT) is a proven technology used in a wide range of applications, including monitoring and diagnosis of industrial machines, facilities and products [1]. Monitoring is usually performed using passive IRT, where the temperature radiated by the inspected object is analyzed to detect abnormal temperature profiles. Testing, on the other hand, commonly uses active IRT, where the object is subjected to an external thermal stimulation, using light or other thermal excitation sources. In active IRT, the temperature-time response to the thermal stimulus in areas with subsurface anomalies produces thermal contrast that can be detected in the infrared spectrum [2]. Other techniques have also been proposed for nondestructive evaluation, including mechanical and optical, penetrating radiation, electromagnetic and electric, sonic and ultrasonic, chemical and analytical, image generation, and signal and image analysis [3], [4].

Active IRT is mostly performed in a static configuration, where the infrared camera, the source of energy used for the stimulation and the inspected object do not move with respect to each other [5]. However, inspecting large products or machines using this procedure is extremely challenging, as it requires performing multiple tests and a difficult merging of the results afterward. A possible alternative approach is the dynamic inspection, where the elements involved in the inspection can move with respect to each other [6], [7]. This approach enables the inspection of large and complex objects with better resolution, providing an increased probability of finding subsurface defects [8]. This approach has been used by NASA after the Columbia Space Shuttle disaster [9], and it is particularly suited for the inspection of large industrial parts. In [10], microwaves were used to inspect large panels in the space shuttle external fuel tank insulating foam. Two of the most common types of dynamic inspections are the line scan and the thermal photocopier. In the line scan, the infrared camera and the source of energy that heats the object line-by-line are moved along the surface while the object is motionless, or vice versa. In the thermal photocopier, only the source of energy that heats the object is moved and passes in front of the camera (in a similar manner as a photocopier machine).

Dynamic inspection using IRT requires data reconstruction to calculate the temperature-time history after the thermal stimulus, producing a pseudo-static sequence. In the case of line scan inspections, the speed of the moving camera and source of energy is required to reinterpolate the acquired thermal sequence. In the case of the thermal photocopier, the procedure is even more complex, as the surface covered by the moving source of energy can overlap during the movements, which requires selecting the correct temperature-time history.

This work investigates dynamic inspection using active IRT, and robust automated procedures are proposed to calculate the pseudo-static sequence. Both the line scan and the thermal photocopier approaches are analyzed, and various methods are proposed to calculate the required temperature-time history after the thermal stimulus. The proposed methods are designed to work in industrial environments, where noise and reflections can affect the acquisition of the infrared sequences. In order to enhance the SNR of the subsurface anomalies, the resulting pseudo-static sequence can be filtered using data processing algorithms such as polynomial fitting, principal component analysis or partial least squares. The proposed procedures are applied on real data, where the inspection results are evaluated.

II. Dynamic to pseudo-static sequence

In active IRT, a thermal stimulus is applied to the inspected object, causing non-stationary heat flow. The propagation of heat produces a thermal contrast between defective and non-defective areas of the inspected object. Therefore, the evolution of the temperature after the application of the thermal stimulus needs to be analyzed to detect subsurface anomalies. When the inspection is applied using a dynamic approach, data reconstruction is required to calculate the temperature-time history after the thermal stimulus, where the thermal contrast caused by defects appears. The proposed methods to perform data reconstruction are described next.

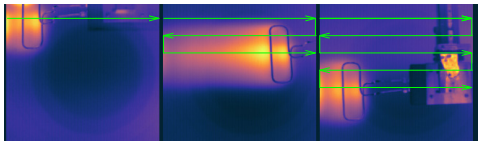

Fig. 1. Movement of the heat source in the thermal photocopier inspection using induction.

A. Thermal photocopier

In a thermal photocopier inspection, the heat source is moved while the infrared camera recording the emitted infrared radiation and the inspected object stand still. Fig. 1 shows an example of this type of inspection using induction as the heat source. Induction thermography is a method to detect defects in electrically conductive materials. It uses a coil excited with an alternating current at high frequency, creating an alternating magnetic field that induces an electric current to objects located near the magnetic field, producing heat. In the considered example, the coil is moved using a robot following the directions of the arrows in the figure.

The inspected object in this example is a carbon fiber skin, aluminum core honeycomb sandwich panel. This inspection is used to describe the proposed procedure for the required data reconstruction in a thermal photocopier inspection to calculate the pseudo-static sequence.

In this work, no restrictions were imposed on the number of times the heat source moved over the object, the direction, the overlapping or the speed. Thus, the inspection is extremely flexible. Moreover, noise and reflections, very common in industrial environments, are assumed to appear in the thermographic sequence. The third image in Fig. 1 shows an example of spurious reflection, where the thermal signature of the operator is reflected on a metal bracket used to mount the heat source onto the robot. This kind of reflection heat appear in the infrared image with more intensity than the heat source, which can greatly affect data reconstruction algorithms.

The first step of the proposed data reconstruction is the detection of intensity peaks in the evolution of temperature for each pixel. Fig. 2 shows the first steps of the procedure. This figure shows the temperature evolution of a pixel and the derivative of this signal. The selected pixel is particularly difficult to process, as it has been stimulated several times due to the overlapping in the movement of the heat source, and includes several spurious reflections. In this example, the heat source is moved five times over the object with overlapping. The objective is to detect the period of time in the signal where the pixel is stimulated with the highest intensity while ignoring reflections that may appear in the image with higher intensity than the stimulation. The period that needs to be extracted, corresponding to the highest stimulation of the pixel surface, is highlighted in the figure.

The proposed procedure for the peak detection is based on the first derivative of the temperature evolution. Possible peaks are detected because they have a downward zero-crossing. However, noise in the signal produces many false positive detections. Thus, the list of possible peaks is further filtered,

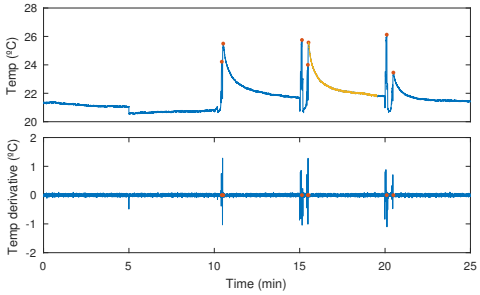

Fig. 2. Detection of peaks in the temperature evolution of a pixel.

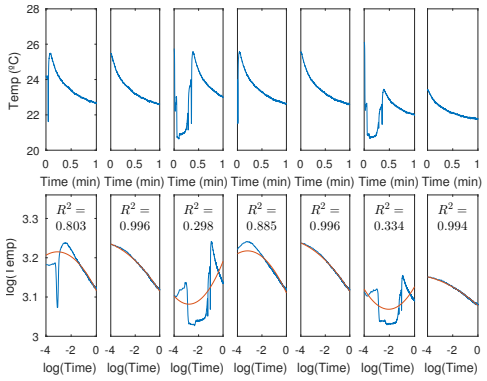

Fig. 3. Temperature evolution after the detected peaks.

by removing valleys, based on the magnitude of the derivative signal at that point and the temperature intensity. Only peaks with a derivative and signal intensities above a threshold are considered valid. The seven detected peaks with the considered temperature-time history are represented in Fig. 2.

The temperature evolutions after the position where each of the seven peaks is detected in the original signal are represented in Fig. 3. A peak corresponding to a thermal stimulus can be distinguished from a reflection because in the thermal stimulus the temperature evolution follows a curve similar to an exponential decay, when it is not affected by other heat sources. In order to test if the temperature evolution after a peak follows an exponential decay, the extracted signals are converted to a logarithmic domain. The resulting signals are then fitted to a second-degree polynomial, and the coefficient of determination is calculated to measure how close the signal is to the fitted regression curve. Only signals with a coefficient of determination above 0.99 are considered to be the response to a thermal stimulus, the rest are considered reflections or noise. As can be seen in Fig. 3, only the second, fifth and seventh peaks meet this criterion. These peaks correspond to different thermal stimulation while the heat source is moved. Among the three detected responses to thermal stimulus in the temperature signal, the one with the highest temperature is selected. When a position in the object is stimulated multiple times, the period of time with the highest intensity is selected, since the probability of detecting subsurface defects is higher in this case. This is the period of time highlighted in Fig. 2.

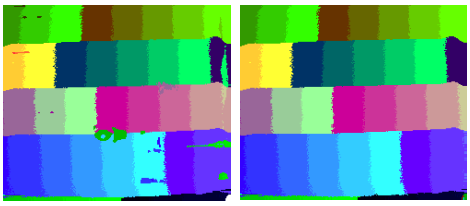

Fig. 4. Time at which the initial thermal stimulus is detected using the maximum of the temperature evolution (left) and the proposed approach (right).

This procedure is extremely robust under heavy noisy conditions and reflections in the temperature signal. Moreover, it is not affected by overlaps in the movement of the heat source over the surface of the inspected object. This provides a very flexible approach to the inspection, as the heat source can move in any direction.

This procedure is repeated for every single pixel in the image. The result can be compared with a naive approach that detects the thermal stimulus using the absolute maximum value of the temperature evolution. Fig. 4 shows this comparison using a high contrast color scale. The color in this figure represents the time at which the thermal stimulus is detected, using the maximum value (left image) and the proposed approach (right image). As can be seen, using the maximum value produces noise in the result due to reflections and artifacts in the images, while the proposed approach produces the correct result.

The extracted responses to the thermal stimulus for every pixel are then combined into a single sequence, which contains the correct temperature evolution after the stimulus for the whole surface of the inspected object. This pseudo-static sequence is the result of the data reconstruction procedure. The result for the considered example is presented in Fig. 5. This figure shows the first image in the reconstructed sequence, a vertical profile in this image, and the temperature evolution at three points in the sequence (highlighted in the image). As can be seen, the thermal stimulus in the inspected object is not uniform. In the middle of the heat source, the temperature is higher. Obtaining a uniform heating would have required displacing the heat source with more overlaps, thus it should have been moved more than five times, requiring a longer inspection. An alternative approach in these cases is the normalization, which provides a remedy to non-uniform heating sensitivity[11]. Data processing using polynomial fitting or principal component analysis also tends to remove the effects of uneven heating.

B. Line scan

In a dynamic inspection using the line scan approach, the position between the infrared camera and the heat source do not change with respect to each other. The movement is produced between the inspected object and the two other components. Fig. 6 shows an example of this type of inspection. In this case, the infrared camera and the light heating source are moved vertically using a robot, while the position of the

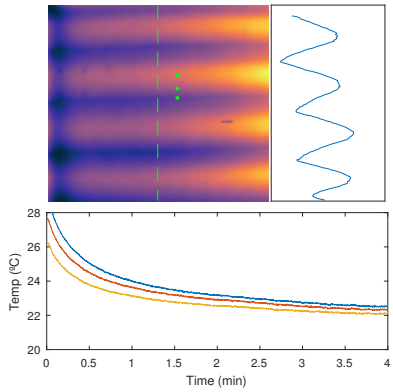

Fig. 5. Results of the data reconstruction of the thermal photocopier inspection.

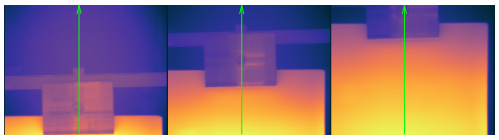

Fig. 6. Movement of the object in the line scan inspection.

inspected object remains fixed. As can be seen, a metallic part that is used to hold the object during the inspection.

In this type of inspection, a line heating lamp stimulates the object just before it becomes visible at the bottom of the image. The robot moves the camera and the lamp downward. This movement displaces the heated line in the object from the bottom to the top of the image. During this time, the infrared camera is recording the temperature response to the thermal stimulus, i.e., the cooling. Data reconstruction requires the calculation of the temperature evolution in the moving object.

In the considered example, the inspected object is parallel to the camera sensor. However, in a different setup, a calibration procedure that translates images to real-world units might be necessary before data reconstruction. Calibration enables the calculation of images without perspective projection, creating a transformed image with a fronto-parallel projection that provides reliable geometric information [12].

Monitoring the temperature while an object is moved is discussed in details in [13], with industrial applications being installed in [14]. The proposed approach is based on motion estimation and compensation. Motion is estimated using distinctive features in the object, which are used to detect the displacement of the object between images. This approach is valid for most scenarios. However, in the case of the inspection of objects with almost uniform temperature distribution, feature detection fails to provide the necessary information to estimate the movement accurately. Therefore, this general approach cannot be used for data reconstruction in dynamic inspections.

Data reconstruction for line scan inspection is analyzed in [7], where it is assumed that the camera frame rate is perfectly synchronized with the scanning speed. A direct transposition between the static and the pseudo dynamic sequence is pos-

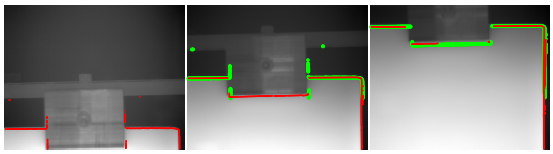

Fig. 7. Estimation of the scanning speed using ICP.

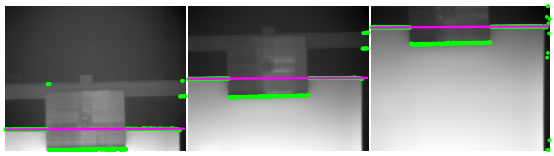

Fig. 8. Estimation of the scanning speed using RANSAC.

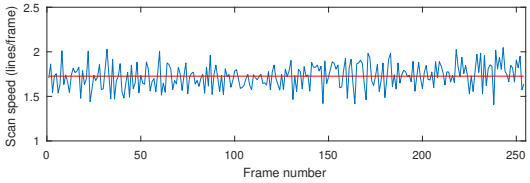

Fig. 9. Estimated scanning speed.

sible in this scenario. In [6] a calibration device is proposed to estimate the scanning speed. This work proposes a more effective alternative: the automated estimation of the scanning speed using only the infrared images of the inspected object.

Typically, in objects with a uniform temperature distribution, it is not possible to extract features that can be used to estimate the movement speed. In this work, the proposed estimation method is based on the information available at the beginning of the inspection. The edges of the object are used to extract all the required information to estimate the scanning speed. Because this speed is generally constant, it can be assumed to be the scanning speed of the rest of the inspection.

Two alternatives are proposed to robustly estimate the scanning speed: edge matching using the Iterative Closest Point algorithm (ICP), a method to estimate correspondences between point clouds; and a line matching using the Random Sample Consensus algorithm (RANSAC), a robust method to estimate mathematical models. The ICP approach starts with the calculation of the edges in the images. Then, a rigid body transformation between edges in consecutive images is calculated based on robust statistics.

The procedure for the estimation of the scanning speed based on ICP is illustrated in Fig. 7. Accurate subpixel edge detection is applied to each image [15]. The calculated edge positions are represented in the images. ICP is used to find a rigid body transformation that matches the edges in two different images. In order to provide robustness in the procedure, an outlier removal filter is included. In the figure, it can be seen the transformation of the edges detected in one image to the coordinates of the next. As can be seen, the result of the ICP is an excellent match between the two set of points, ignoring outliers. From the calculated transformations, the value ty, the vertical translation, can be obtained. The difference between the value ty in the transformation estimated between the images can be used to estimate the scanning speed.

In the RANSAC procedure, the transformation is calculated based on horizontal lines detected in the images, taking advantage of the frequent rectangular shape of the inspected objects. In this case, lines are detected using the gradient of the image in the vertical direction. The procedure for the estimation of the scanning speed based on RANSAC is illustrated in Fig. 8. The vertical gradient for each image is first calculated as $\partial I/\partial y$, where I is the image. Then, the maximum gradient value for each column in the image is calculated, as it can correspond to the top border of the inspected object. The positions of these points are represented in the figure. As can be seen, not all points belong to the top border of the inspected object. In this particular example, some points belong to a metallic part that is used to hold the object. In other cases, noise and outlier detections frequently appear in this type of procedures. RANSAC is used to detect the line that corresponds to the top border of the inspected object robustly, regardless other points in the data that do not belong to this line. The resulting lines from this procedure are represented in the figure. As can be seen, the lines correspond to the top border of the object, and the calculation is not affected by other points in the data. When the detected line is represented using polar coordinates (θ, ρ), the difference between the value ρ in the estimated lines in the images can be used to estimate the scanning speed.

Fig. 9 shows the estimated scanning speed, V_y, for the considered example. The speed is represented in vertical lines in the camera sensor that the object moves from one image to the next upward. In this example, the estimation of the scanning speed is performed for the first 250 images (around 10 seconds), resulting in an average of 1.72 lines per frame, i.e., in every new frame acquired by the camera, the object moves 1.72 pixels upward in the image.

The line scan inspection is performed with a camera at an acquisition frequency F, using a specific number of lines H. The sensor resolution, the detector pitch, the lens used with the camera, and the distance from the camera to the inspected object can also be used to calculate the vertical field of view, $VFOV$. The inspection parameters F and H depend on the camera. The parameter $VFOV$ depends on the camera, but also on the lens and distance from the camera to the object. The parameter V_y depends on the movement speed between the camera and heat source, and the inspected object. The scanning speed has an impact on the amount of energy that is transmitted to the specimen and consequently on the limiting of the size and depth of the defects that can be detected. Small and deep defects can only be detected when using lower scanning speed (since the observation time is increased and more energy is transferred to the specimen).

Using the inspection parameters, some interesting variables about the inspection can be calculated. The observation time, t_{obs}, which is the time in seconds during which a given

line of the object is visible by the camera can be calculated using Eq. 1. Following a similar procedure, the number of consecutive frames during which a given line of the object is visible, N_{obs}, can be calculated using Eq. 2. The speed, v, at which the camera is moved with respect to the camera in SI units can be calculated using Eq. 3.

$$t_{obs} = \frac{H}{FV_y} \tag{1}$$

$$N_{obs} = \frac{H}{V_y} = t_{obs}F \tag{2}$$

$$v = \frac{VFOV}{t_{obs}} \tag{3}$$

The number of consecutive frames during which a given line of the object is visible, N_{obs}, is often referred to as the virtual frame rate, as the number of frames in the calculated pseudo-static sequence is equal to that number.

The transformation of the acquired dynamic sequence, D, into the pseudo-static sequence, PS, only depends on the estimated scanning speed V_y. A pixel $D(i,j,k)$ or $PS(i,j,k)$ correspond to the row i, column j, frame k in the sequence. The symbol : is used to indicate all pixels in the row, column or frame. When the scanning speed parameter, V_y, is 1, data reconstruction can be performed using a transposition of the rows between the two sequences: the first row in the first frame of the dynamic sequence, $D(1,:,1)$, corresponds to the first row in the first frame of the pseudo-static sequence, $PS(1,:,1)$; $D(2,:,2)$ corresponds $PS(1,:,2)$; and so on. This way, the frames in the pseudo-static sequence correspond to the temperature evolution of a line in the inspected object.

In a real application, it is very difficult to synchronize the mechanical motion of the inspected object with respect to the camera and the acquisition frame rate of the camera. Therefore, in general V_y is not 1. In this work, a general procedure is proposed that is valid for any value of V_y. In the beginning, $D(1,:,1)$ is assigned $PS(1,:,1)$. However, the first row in the second frame of the pseudo-static sequence, $PS(1,:,2)$, cannot be calculated directly, and requires reinterpolation. $PS(1,:,2)$ can be calculated by interpolating the second frame of the dynamic sequence at row V_y, $D(V_y,:,2)$. This interpolation calculates the intensity values of pixels along the line in the image where the line of the object is projected in this frame. $PS(1,:,3)$ is calculated by interpolating the third frame of the dynamic sequence at row $2V_y$, $D(2V_y,:,2)$, and so on.

Fig. 10 shows the result of data reconstruction for the considered line scan inspection. The image on the left is the first frame of the reconstructed sequence, and the graph on the right shows the temperature evolution of the pixel highlighted in the image. This pseudo-static sequence contains the correct temperature evolution of the material after the thermal stimulus, and it can be analyzed for defect detection. As can be seen in the image, some shallow defects are already visible. However, applying post-processing algorithms to this sequence will greatly enhance the SNR of these defects.

The proposed data reconstruction procedure is fully automatic, no inputs are required. The proposed procedure analyzes the sequence looking for either matching edges between consecutive images using robust ICP, or horizontal lines using a robust RANSAC approach. In any of the two proposed methods, a robust estimation of the scanning speed is obtained. The average estimated scanning speed for the whole sequence is then used for data reconstruction using the method described above, producing the required pseudo-static sequence for defect detection. In general, the scanning speed cannot be estimated in every single frame of the sequence due to uniform temperature distribution. However, it can be calculated very accurately at the beginning and at the end of the inspection, where the edges of the object provide all the required information.

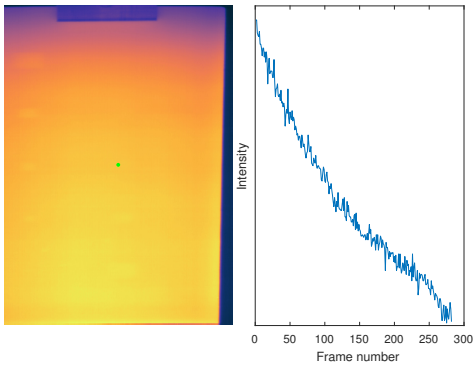

Fig. 10. Results of the data reconstruction of the line scan inspection.

III. Results and Discussion

In order to test the proposed procedures for dynamic inspection, they have been applied to the inspection of a honeycomb sandwich panel. The resulting pseudo-static sequences were subsequently filtered using data post-processing algorithms to enhance the SNR of the subsurface anomalies.

A. Materials

The specimen used to test the proposed procedures is a honeycomb sandwich panel of 560×560 mm size and 50 mm thick, with aluminum honeycomb core and a cell size of 1/8". The panel has several square inclusions with different lateral sizes (3, 5, 7, 10 and 15 mm) located at different depths, as depicted in Fig. 11. The panel also includes defects caused by impact damage. A region of interest is highlighted in the figure for later tests.

The infrared camera used to record the infrared radiation resulting from the thermal stimulus is a Flir A655sc. The camera has a 24.6 mm lens, and a sensor of 640×480 resolution. The temperature range is configurable within several available ranges. In the experiments, the range [-40, 140 °C] was selected. The manufacturer reports measurement accuracy of ±2 K and sensitivity lower than 30 mK at 30 °C. The longwave infrared camera operates at 7.5 to 14 μm. The detector type used in the camera is an uncooled microbolometer. No further configuration is applied to the camera, as only raw radiation data is analyzed for defect detection.

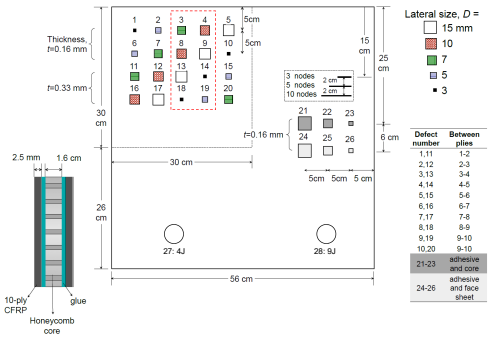

Fig. 11. Model of the panel used for testing with positions, sizes and depths of the defects.

B. Data post-processing

Thermal contrast caused by subsurface anomalies can be inappreciable, depending on the size and depth of the defect. Thus, data post-processing algorithms are applied to enhance the signal-to-noise ratio (SNR) and improve the visualization of the thermal contrast [16]. The post-processing methods used in this work: principal component thermography and polynomial fit and time derivatives, are briefly described next. These two methods have been proven to provide the best results with a wide variety of stimulation and materials [17].

1) Principal component thermography

Principal Component Thermography (PCT) is a post-processing algorithm based on principal component analysis, a statistical technique of information synthesis. The objective is to reduce the number of variables in a dataset, while losing the least amount of relevant information possible.

The calculation of PCT is based on singular value decomposition (SVD), which decomposes the thermal sequence into a series of statistic orthogonal functions known as Empirical Orthogonal Functions (EOF) [18]. The first components provide a reduction of the data without removing useful information about the defects [19].

2) Polynomial fit and time derivatives

In this method, the temperature-time history of every pixel in the thermal sequence is approximated by a polynomial. This approach can be applied to the cooling, but also to the heating period [17]. This method is referred to as Thermographic Signal Reconstruction (TSR) [20]. The evolution of the temperature during cooling is adjusted to an n degree polynomial as shown in (4).

$$T(t) = a_n t^n + a_{n-1} t^{n-1} + \ldots + a_1 t + a_0 \tag{4}$$

When this method is applied to thermography, the signals are previously converted to the logarithmic domain. However, this conversion is not required when applying this method to step heating thermography, since polynomial with a degree above 4 can capture the dynamic of the cooling period.

The polynomial fitting provides the opportunity to filter noise and compress the thermal sequence, as only the coefficients of the polynomials are required to reconstruct the complete sequence. Moreover, the most important advantage is that it can be used to calculate the time derivatives analytically. These derivatives have been proven to be one of the best methods to enhance the visualization of defects, especially the first and second derivative.

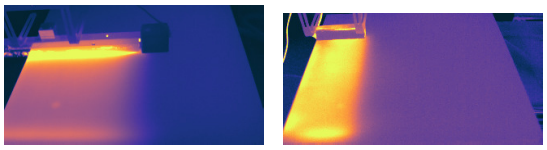

(a) (b)

Fig. 12. Configurations used for the inspection using the thermal photocopier. (a) Stimulation based on a quartz linear IR heater. (b) Stimulation based on induction.

C. Thermal photocopier

Two different configurations have been applied for the thermal photocopier: stimulation based on light, using a low power quartz linear IR heater; and stimulation based on induction, using a coil excited with an alternating current at high frequency. Fig. 12 shows two frames acquired during the inspection using the two considered configurations. As can be seen, the scanning direction is different than the example showed previously. Moreover, the width of the heating source changes. These two new scenarios are used to validate the proposed approach for the automatic calculation of the pseudo-static sequence.

The calculation of the pseudo-static sequence follows the procedure described before. Peaks are detected and filtered in the temperature-time history of every pixel. Then, the time period corresponding to the response to the thermal stimulus is extracted from the signal. The pseudo-static sequence is calculated by combining the temperature evolution after the stimulus for the whole surface of the inspected object. Fig. 13a shows the first frame of the resulting pseudo-static sequence using the stimulation based on light. The proposed procedure accurately detects the correct temperature-time history after the thermal stimulus. The calculated pseudo-static sequence is processed using the two considered algorithms to improve the SNR of the defects.

The results of the stimulation based on a quartz linear IR heater can be seen in Fig. 13. Fig. 13b show the image resulting from PCT. In this case, it shows the seconds EOF, which provides the best results in this case compared to other EOF. Figs. 13c and 13d show the image resulting from the first and second derivative of the polynomial fit. A polynomial of fifth degree was used, and signals were converted to the logarithmic domain before fitting. The contrast of all the images in Fig. 13b have been improved to visualize all the defects using an adaptive histogram equalization [21].

Images in Fig. 13 show a clear difference between the raw image and the images resulting from post-processing. In the raw image the only visible defects are the two large defects at the bottom of the panel (number 27 and 28) caused by impact damage. All the other defects are missed. However, the images obtained using PCT and derivatives show more defects, and

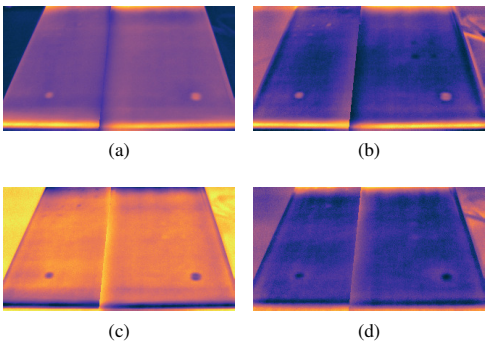

Fig. 13. Images resulting from the infrared inspection based on the thermal photocopier method using a quartz linear IR heater. (a) Raw image. (b) PCT EOF 2. (c) First derivative. (d) Second derivative. The contrast of all the images have been improved using an adaptive histogram equalization.

TABLE I
DETECTED DEFECTS FROM THE INFRARED INSPECTION BASED ON THE THERMAL PHOTOCOPIER METHOD USING LIGHT

Raw	27, 28
PCT	4, 11, 12, 13, 16, 17, 21, 22, 24, 25, 27, 28
First derivative	2, 3, 4, 8, 9, 11, 12, 13, 16, 17, 27, 28
Second derivative	13, 21, 22, 24, 27, 28

thus, can be used to visualize more subsurface anomalies. The complete list of defects detected is presented in Table I. The best results were obtained in the PCT and the first derivative of the polynomial fit. However, the advantage of PCT is that a technician can analyze this image (EOF 2) without having to look the entire sequence of images, contrary to the case with the polynomial fitting and derivatives.

The results of the stimulation based on induction can be seen in Fig. 14. As can be seen, the results are worse than when the test piece is stimulated using an IR heater. These results are consistent with previous literature, where induction is mostly used for cracks and not for subsurface defects [22]. Post-processing algorithms, in this case, did not improve the SNR of the defects significantly. Nevertheless, the PCT algorithm slightly improves the detection of defects.

The complete list of defects detected using induction is presented in Table II. The number of detected defects in all case is clearly reduced compared with the experiments using an IR heater.

The results of these experiments can be used to validate the proposed procedure for the calculation of the pseudo-static sequence. Not only does the proposed method extract the cooling period correctly, it also allows the resulting sequence

TABLE II
DETECTED DEFECTS FROM THE INFRARED INSPECTION BASED ON THE THERMAL PHOTOCOPIER METHOD USING INDUCTION

Raw	11, 12, 13, 27, 28
PCT	11, 12, 13, 16, 17, 27
Fit'	12, 13, 27, 28
Fit"	

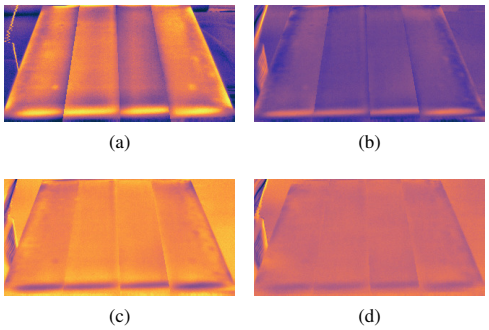

Fig. 14. Images resulting from the infrared inspection based on the thermal photocopier method using induction. (a) Raw image. (b) PCT EOF 2. (c) First derivative. (d) Second derivative. The contrast of all the images have been improved using an adaptive histogram equalization.

to be analyzed using advanced post-processing method to improve defect detection.

D. Line scan

The same two configurations for the thermal stimulation were used for the line scan method: induction and IR heater. The inspected specimen has a rectangular shape, thus, the extraction method RANSAC was used. Using this procedure, an average scanning speed was calculated and used for data reconstruction, producing the required pseudo-static sequence for defect detection. The scanning speed was estimated at the beginning and at the end of the inspection, where the edges of the specimen are visible by the camera.

The comparison of the results using the two considered thermal stimulation configurations, induction and IR heater, were similar to those obtained in the thermal photocopier method. When the specimen was thermally stimulated using light more defects were detected. This depends on the type of defects in the inspected specimen.

In terms of defect detectability, the line scan method shows far superior performance compared to the thermal photocopier. Fig. 15 shows the results obtained using the line scan method with light stimulation to the region of interest highlighted in Fig. 11. All the defects in the considered regions are visible and, thus, they can be detected. This figure can also be used to compare the differences between the raw image and the images obtained after post-processing. Improved results can be seen in the images obtained after post-processing, particularly the PCT EOF 2 and the first derivative of the polynomial fit.

These results are not only better from the point of view of the SNR compared to the thermal photocopier, defect detectability is also greatly increased, as even small defects can be detected using the line scan method. Moreover, this increased performance is obtained using the same stimulation energy in both methods, thermal photocopier and line scan. Thus, they both capture an equivalent temperature-time history after thermal stimulation. Nevertheless, it should be noted that the field of view is different. The line scan results were acquired with the camera perpendicularly positioned with

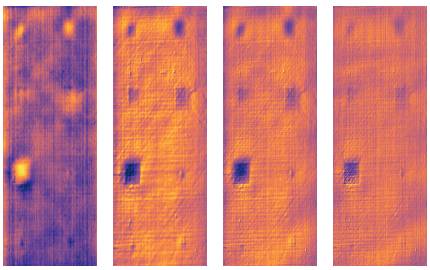

(a) (b) (c) (d)

Fig. 15. Images resulting from the infrared inspection based on the line scan method using an IR heater to a region of interest. (a) Raw image. (b) PCT EOF 2. (c) First derivative. (d) Second derivative. The contrast of all the images have been improved using an adaptive histogram equalization.

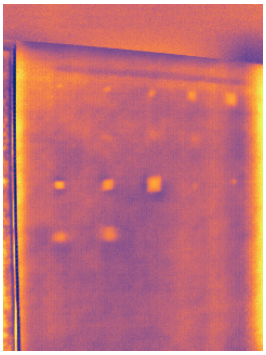

Fig. 16. Image resulting from the infrared inspection based on the thermal photocopier method using a quartz linear IR heater with decreased distance (PCT EOF 2).

respect to the specimen surface, whilst this is not the case for the thermal photocopier experiment.

The key to understanding the difference in the results between the two methods is the spatial resolution and the observation angle of the image. In general, when the size of a defect is doubled it can be detected in twice as much noise. In the line scan method, the camera is located close to the inspected specimen (approximately 20 cm). Thus, the perceived size of the defect is higher, as it is captured with more pixels. Thus, under similar noise in the thermal photocopier and the line scan stimulation, the line scan method produces better SNR and higher defect detectability. This conclusion can be corroborated by performing a new experiment using the thermal photocopier where the camera is closer to the inspected specimen. Decreasing the distance between camera and the inspected object also decreases the field of view, thus, only a part of the specimen is visible. The results of the inspection are presented in Fig. 16. In this case, the number of detected defects is greatly increased. However, only a small part of the object can be inspected.

IV. Conclusions

Active IRT was used to detect subsurface anomalies using a thermal stimulation that produces contrast detected in the infrared spectrum. A dynamic inspection approach where the camera, heat source and specimen can move with respect to each other was presented as an alternative approach to a static configuration. This dynamic approach has superior advantages for the inspection of large products or machines, such as the increased resolution. However, the procedure is also extremely challenging, as it requires data reconstruction. This work has analyzed two methods for dynamic inspection: the thermal photocopier and the line scan, and proposed automatic and robust methods for data reconstruction that generate a pseudo-static sequence.

Results indicate that the proposed procedures can be used to inspect materials efficiently. The pseudo-static sequences were extracted correctly under different configurations, using induction and light to thermally stimulate the material for different thermal source sizes. Moreover, the images resulting from the inspection can be further processed using advanced data processing algorithms to improve SNR and defect detection. The comparison between the thermal photocopier method and the line scan shows that the line scan produces superior results due to the increased resolution. This enables the detection of defects with increased SNR, but also the detection of smaller defects, that could go undetected using other inspection procedures.

The considered dynamic inspection procedures and the proposed methods to extract pseudo-static sequences automatically can be applied in a number of different areas, where nondestructive inspection of large products or machines is required. The camera, heat source and specimen can move with respect to each other, which allows the inspection of large products with increased resolution at the expense of slightly increased complexity in the inspection.

References

[1] S. Bagavathiappan, B. Lahiri, T. Saravanan, J. Philip, and T. Jayakumar, "Infrared thermography for condition monitoring–a review," *Infrared Physics & Technology*, vol. 60, pp. 35–55, 2013.

[2] R. Usamentiaga, P. Venegas, J. Guerediaga, L. Vega, J. Molleda, and F. G. Bulnes, "Infrared thermography for temperature measurement and non-destructive testing," *Sensors*, vol. 14, no. 7, pp. 12 305–12 348, 2014.

[3] A. Foudazi, C. A. Edwards, M. T. Ghasr, and K. M. Donnell, "Active microwave thermography for defect detection of cfrp-strengthened cement-based materials," *IEEE Transactions on Instrumentation and Measurement*, vol. 65, no. 11, pp. 2612–2620, 2016.

[4] Y. Wang, B. Gao, W.-L. Woo, G. Y. Tian, X. Maldague, L. Zheng, Z. Guo, and Y. Zhu, "Thermal pattern contrast diagnostic of micro cracks with induction thermography for aircraft braking components," *IEEE Transactions on Industrial Informatics*, 2018.

[5] C. Ibarra-Castanedo, P. Servais, A. Ziadi, M. Klein, and X. Maldague, "Rita-robotized inspection by thermography and advanced processing for the inspection of aeronautical components," in *12th International Conference on Quantitative InfraRed Thermography*, 2014.

[6] B. Oswald-Tranta and M. Sorger, "Scanning pulse phase thermography with line heating," *Quantitative InfraRed Thermography Journal*, vol. 9, no. 2, pp. 103–122, 2012.

[7] F. Khodayar, F. Lopez, C. Ibarra-Castanedo, and X. Maldague, "Optimization of the inspection of large composite materials using robotized line scan thermography," *Journal of Nondestructive Evaluation*, vol. 36, no. 2, p. 32, 2017.

[8] ——, "Implementation of advanced signal processing techniques on line-scan thermography data," in *Electrical and Computer Engineering (CCECE), 2017 IEEE 30th Canadian Conference on*. IEEE, 2017, pp. 1–4.

[9] D. F. Woolard and K. E. Cramer, "Line scan versus flash thermography: comparative study on reinforced carbon-carbon," in *Defense and Security*. International Society for Optics and Photonics, 2005, pp. 315–323.

[10] S. Kharkovsky, J. T. Case, M. A. Abou-Khousa, R. Zoughi, and F. L. Hepburn, "Millimeter-wave detection of localized anomalies in the space shuttle external fuel tank insulating foam," *IEEE Transactions on Instrumentation and Measurement*, vol. 55, no. 4, pp. 1250–1257, 2006.

[11] D. L. Balageas, "Defense and illustration of time-resolved pulsed thermography for nde," *Quantitative InfraRed Thermography Journal*, vol. 9, no. 1, pp. 3–32, 2012.

[12] R. Usamentiaga, "Easy rectification for infrared images," *Infrared Physics & Technology*, vol. 76, pp. 328–337, 2016.

[13] R. Usamentiaga and D. F. García, "Infrared thermography sensor for temperature and speed measurement of moving material," *Sensors*, vol. 17, no. 5, p. 1157, 2017.

[14] R. Usamentiaga and D. F. Garcia, "Enhanced temperature monitoring system for sinter in a rotatory cooler," *IEEE Transactions on Industry Applications*, vol. 53, no. 2, pp. 1589–1597, 2017.

[15] A. Trujillo-Pino, K. Krissian, M. Alemán-Flores, and D. Santana-Cedrés, "Accurate subpixel edge location based on partial area effect," *Image and Vision Computing*, vol. 31, no. 1, pp. 72–90, 2013.

[16] R. Usamentiaga, C. Ibarra-Castanedo, M. Klein, X. Maldague, J. Peeters, and A. Sanchez-Beato, "Nondestructive evaluation of carbon fiber bicycle frames using infrared thermography," *Sensors*, vol. 17, no. 11, p. 2679, 2017.

[17] R. Usamentiaga, P. Venegas, J. Guerediaga, L. Vega, and I. López, "A quantitative comparison of stimulation and post-processing thermographic inspection methods applied to aeronautical carbon fibre reinforced polymer," *Quantitative InfraRed Thermography Journal*, vol. 10, no. 1, pp. 55–73, 2013.

[18] N. Rajic, "Principal component thermography for flaw contrast enhancement and flaw depth characterisation in composite structures," *Composite Structures*, vol. 58, no. 4, pp. 521–528, 2002.

[19] C. Ibarra-Castanedo, N. P. Avdelidis, M. Grenier, X. Maldague, and A. Bendada, "Active thermography signal processing techniques for defect detection and characterization on composite materials," in *Thermosense XXXII*, vol. 7661. International Society for Optics and Photonics, 2010, p. 76610O.

[20] S. M. Shepard, J. R. Lhota, B. A. Rubadeux, D. Wang, and T. Ahmed, "Reconstruction and enhancement of active thermographic image sequences," *Optical Engineering*, vol. 42, no. 5, pp. 1337–1342, 2003.

[21] A. M. Reza, "Realization of the contrast limited adaptive histogram equalization (clahe) for real-time image enhancement," *The Journal of VLSI Signal Processing*, vol. 38, no. 1, pp. 35–44, 2004.

[22] U. Netzelmann, G. Walle, S. Lugin, A. Ehlen, S. Bessert, and B. Valeske, "Induction thermography: principle, applications and first steps towards standardisation," *Quantitative InfraRed Thermography Journal*, vol. 13, no. 2, pp. 170–181, 2016.

Bibliographie

[1] Emmanouilidis c, S Vasilios, and K Hrissagis. A mobile robot for automated non-destructive testing of steel plates. *Zenon SA, Automation Technologies*.

[2] Horst Czichos. Scope of technical diagnostics. In *Handbook of Technical Diagnostics*, pages 3–9. Springer, 2013.

[3] Henrique Fernandes, Hai Zhang, Clemente Ibarra-Castanedo, and Xavier Maldague. Fiber orientation assessment on randomly-oriented strand composites by means of infrared thermography. 121, 11 2015.

[4] Direct INdustry. Fanuc lrmate 200id/7l. http://http:/www.directindustry.fr/prod/fanuc-robotics/robots-articules-6-axes-pick-and-place-emballage-14532-1420339.html/.

[5] C Krishnamurthy, Krishnan Balasubramaniam, N Biju, M Arafat, and N Ganesan. Tone burst eddy current thermography (tbet) for nde applications. In *Proceedings of the National Seminar & Exhibition on Non-Destructive Evaluation, Chennai, India*, pages 10–12, 2009.

[6] X Maldague. John wiley-interscience. In *Therory and practice of infrared technology for Non Destructive Testing*, 2001.

[7] Xavier Maldague. Theory and practice of infrared technology for nondestructive testing. 2001.

[8] C Mineo, D Herbert, M Morozov, SG Pierce, PI Nicholson, and I Cooper. Robotic non-destructive inspection. In *51st Annual Conference of the British Institute of Non-Destructive Testing*, pages 345–352, 2012.

[9] N Rajic. Principal component thermography for flaw contrast enhancement and flaw depth characterisation in composite structures. *Composite Structures*, 58(4):521 – 528, 2002.

[10] H Rowshandel, GL Nicholson, CL Davis, and C Roberts. A robotic approach for ndt of rcf cracks in rails using an acfm sensor. *Insight-Non-Destructive Testing and Condition Monitoring*, 53(7):368–376, 2011.

[11] H. Rowshandel, G.L. Nicholson, C.L. Davis, and C. Roberts. A robotic system for non-destructive evaluation of rcf cracks in rails using an acfm sensor. In *Railway Condition Monitoring and Non-Destructive Testing (RCM 2011), 5th IET Conference on*, pages 1–6, Nov 2011.

[12] Tariq P. Sattar and Alina-Alexandra Brenner. Robotic system for inspection of test objects with unknown geometry using ndt methods. *Industrial Robot : An International Journal*, 36(4):340–343, 2009.

[13] Peter J Shull. *Nondestructive evaluation : theory, techniques, and applications*. CRC press, 2002.

[14] M. W. Siegel. Automation for nondestructive inspection of aircraft. *American Institute of Aeronautics and Astronautic*, 1994.

[15] Gia Phuong Tran. *Crack Inspection and simulations with Eddy Current Thermography for the Aerospace Industry*. PhD thesis, Université Laval, 2013.

[16] P Tran-Gia, X Maldague, and L Birglen. Crack detection limit in eddy current thermography. *The American Society for Nondestructive Testing Research Symposium*, (22), 2013.

[17] M Viens. Courants de foucault. In *Essai mécanique et contrôle non destructif*, 2013.

[18] M Viens. Introduction au contrôle non destructif. In *Essai mécanique et contrôle non destructif*, 2013.

[19] M Viens. Ultrasons (ut). In *Essai mécanique et contrôle non destructif*, 2013.

[20] G Zenzinger, J Bambergt, W Satzgert, and V Carl. Thermographic crack detection by eddy curreent excitation. *MTU Aero Engines, Muenchen Germany TZFP, Dinslaken, Germany*.